Induction Infrared Thermography for Non-Destructive Evaluation of Alloy Sensitization

Matthew Thomas Roberts

Thesis submitted to the faculty of the Virginia Polytechnic Institute and State University
in partial fulfillment of the requirements for the degree of

Master of Science
In
Ocean Engineering

Kevin G. Wang, Chair
Emily L. Guzas, Co-Chair
Christine M. Gilbert
Gary D. Seidel

April 30, 2019
Blacksburg, VA

Keywords: Sensitization, Induction Thermography, Non-Destructive Evaluation

Induction Infrared Thermography for Non-Destructive Evaluation of Alloy Sensitization

Matthew Thomas Roberts

ABSTRACT

The sensitization of stainless steel describes the process by which a high-carbon alloy is heated above a certain threshold (either naturally or artificially) followed by a cooling period during which chromium (which provides the metal with its corrosion-inhibiting properties) comes out of solid solution and forms chromium carbides ($Cr_{23}C_6$) along the material's natural grain boundaries. This dissolution of chromium from the alloy makes the material more susceptible to intergranular corrosion (IGC), environmentally-assisted cracking (EAC), and broader failure. Currently, the accepted techniques used to test for the presence of sensitization (ASTM A262 being one of the most widely-accepted) are qualitative and/or destructive in nature. Attempts have been made to non-destructively characterize sensitization through various means including the propagation of sound waves and with Hall sensors, all with mixed results. With the use of these high-carbon alloys in a range of industries, a comprehensive, *in-situ* process is desirable.

This thesis will focus specifically on non-destructive evaluation of sensitization seen in the heat affected zones (HAZ) of a weld using induction infrared thermography (IIRT). Previous IIRT experimental results have shown asymmetric heating in the HAZ of a weld when sensitization is present. As the altered microstructure affects a material's electrical properties, the induced eddy currents are forced to take different paths through a more resistive material, which results in disproportionate heating that can be detected with an infrared (IR) camera. New IIRT experiments have been conducted on both welded and unwelded 440C alloy samples to establish quantitative data on the heating profiles. These results (in conjunction with the appropriate experimental parameters) were then used to inform a numerical model to replicate them. Despite some limitations in populating the model with accurate parameters, the results obtained were in good agreement with the experiments and provide a foundation for future work. Future work will focus on further model development to establish a predictive tool that can detect and quantify the level of sensitization in an arbitrary steel sample in the field.

Induction Infrared Thermography for Non-Destructive Evaluation of Alloy Sensitization

Matthew Thomas Roberts

GENERAL AUDIENCE ABSTRACT

The sensitization of stainless steel describes the process by which a high-carbon steel alloy is heated above a certain threshold (either naturally or artificially) followed by a cooling period during which chromium (one of the elements most responsible for providing stainless steel with its corrosion-inhibiting properties) forms new compounds with the carbon present in the steel. With the chromium being taken from the parent material to form these compounds, the corrosion-resistant properties are compromised, which can lead to corrosion, cracking, and broader failure. Currently, the accepted techniques used to test for the presence of sensitization are qualitative and/or destructive in nature. Attempts have been made to non-destructively detect and characterize sensitization through various means, but all with mixed results. With the use of these high-carbon alloys in a range of industries, a comprehensive, in-place process is desirable.

This thesis will focus specifically on non-destructive evaluation of sensitization seen as a result of welding steel plates using induction infrared thermography (IIRT). This process uses an induction coil to generate heat within a sample whose resulting heat signature can then be detected with an infrared (IR) camera and analyzed. Previous IIRT experimental results have shown higher levels of heating in the HAZ when sensitization is present as it modifies the original microstructure of the material. New IIRT experiments have been conducted on both welded and unwelded 440C alloy samples to establish quantitative data on the heating profiles. These results (in conjunction with the appropriate experimental parameters) were then used to create a numerical model to replicate them. Despite some limitations in populating the model with accurate parameters, the results obtained were in good agreement with the experiments and provide a foundation for future work. Future work will focus on establishing a predictive tool that can detect and quantify the level of sensitization in an arbitrary steel sample in the field.

DEDICATION

I would never have gotten to this point without the love and support from my family, mom, dad, and John, as well as from Hilary Katz who has always stuck by me through thick and thin.

I am forever grateful.

ACKNOWLEDGEMENTS

I must begin by thanking Maria Medeiros and the Office of Naval Research (ONR) for their generous funding of this project under contract N00014-18-1-2059. I would also like to give a special thanks to my advisor, Dr. Kevin Wang, for taking the chance on me to pursue this project and ensuring I was positioned to succeed every step of the way.

The Naval Research Enterprise Internship Program (NREIP) was instrumental in this project, giving me the chance to go hands-on with the laboratory equipment at the Naval Undersea Warfare Center, Division Newport (NUWCDIVNPT) to run new IIRT experiments.

The talented engineers at NUWCDIVNPT, particularly Drs. Emily Guzas, Patric Lockhart, and Wayne Tucker, provided me invaluable insights in to this problem and took the time to pass on their breadth knowledge. Additionally, Lis Foster, Mike Lapera, Wendell Maciejewski, Ally MacInnis, and Matt Rice were all more than willing to contribute their time whenever I needed assistance.

Finally, I want to acknowledge my graduate colleagues at Virginia Tech for always making themselves available to answer my questions and for providing their support.

Table of Contents

1 Introduction 1
1.1 Sensitization Overview 1
1.2 Motivation 2
1.3 Accomplishments 5
2 Review of Literature 6
2.1 Non-Destructive Evaluation (NDE) and Non-Destructive Testing (NDT) 6
2.2 Eddy Current (EC)/Eddy Current Thermography (ECT) 6
2.3 NDE/NDT to Detect Sensitization 7
2.4 Challenges and Knowledge Gaps 8
3 Design and Methodology 9
3.1 Governing Equations 9
3.1.1 Overview 9
3.1.2 Skin Depth 10
3.1.3 Maxwell's Equations 10
3.1.4 Heat Transfer 13
3.2 Limitations and Assumptions 14
3.3 Description of Phi (Φ) 16
3.4 Image Processing 18
3.5 Experiments 19
3.5.1 Proof-of-Concept Data (2018) 19
3.5.2 Simulation Data (2019) 22
3.6 Numerical Simulations 23
4 Results 30
4.1 2018 Experimental Results 30
4.2 2019 Experimental Results 31
4.3 Simulation Results 33
4.3.1 Baseline 33
4.3.2 Modified HAZ 36
4.3.3 Trackline Comparison 42
5 Discussion 45
5.1 Model Parameter Selection 46
5.1.1 Current 47
5.1.2 Relative Magnetic Permeability 48
5.1.3 Electrical Conductivity (HAZ) 49
5.1.4 Emissivity 51
5.1.5 HAZ Location 52
5.2 Meshing 53
5.3 Behavior of Welded Region 53
5.4 Emissivity 55
5.5 Limitations/Challenges 56
5.5.1 Current in Coil 56
5.5.2 IR Thermometer 56
5.5.3 Placement of Coil 56
6 Conclusions and Future Work 56

6.1 Future Work – Modeling 57
6.1.1 HAZ Conductivity 57
6.1.2 Weld Incorporation 58
6.1.3 Mesh Refinement 58
6.2 Future Work – Experiments 58
6.2.1 SEM Images 58
6.2.2 Power Supply 58
6.2.3 Means of Sensitization 58
6.2.4 Temperatures of Heating 59
6.2.5 Painting Samples 59
6.2.6 Surface Treatments 59
6.2.7 New Materials 59
Appendix A – ImageJ Image Processing Procedure 60
Appendix B – Experimental Data, 2018 65
Appendix C – Experimental Data, 2019 72
References 79

Table of Figures

Figure 1 – Schematic of "Sensitized" Grain Boundaries [4] 1
Figure 2 – Time-Temperature-Sensitization Graph of Type 304 Steel 2
Figure 3 – Welded 440C Plate with Sensitized HAZ 3
Figure 4 – Schematic of Weld/HAZ Regions 4
Figure 5 – Temperatures in Weld/HAZ Regions (304 Steel) 4
Figure 6 – Temperature Ranges for Sensitization (304 Steel) 4
Figure 7 – Example IIRT Scan 5
Figure 8 – Micrograph Images of 440C Steel 5
Figure 9 – Schematic of Typical Induction Heating Setup 9
Figure 10 – Typical B-H Curves 14
Figure 11 – Generic Ferromagnetic Hysteresis Loop 15
Figure 12 – B-H Curve of 416 Steel 16
Figure 13 – Example Raw SEM Image (301 Steel) 18
Figure 14 – Example SEM Image (301 Steel) Processed with ImageJ 18
Figure 15 – Experimental Setup 19
Figure 16 – "Pancake" Coil 20
Figure 17 – Example Background/Heated Scan 20
Figure 18 – Hairpin Coil 23
Figure 19 – Induction Heating Edge Effects 24
Figure 20 – COMSOL Model, Coil Offset 25
Figure 21 – COMSOL Model, Isometric View 26
Figure 22 – COMSOL Model, Plan View 26
Figure 23 – Impedance Boundary Condition Model Domains (Highlighted) 29
Figure 24 – Baseline Trial 1, Temperature Profile 34
Figure 25 – Baseline Trial 1, Temperature Profile 34
Figure 26 – Baseline Trial 2, Plan View Temperature 35
Figure 27 – Baseline Trial 2, Temperature Profile 35
Figure 28 – Welded Trial 1, Plan View Temperature 37
Figure 29 – Welded Trial 1, Temperature Profile 37
Figure 30 – Welded Trial 2, Plan View Temperature 38
Figure 31 – Welded Trial 2, Temperature Profile 38
Figure 32 – Welded Trial 3, Plan View Temperature 39
Figure 33 – Welded Trial 3, Temperature Profile 39
Figure 34 – Welded Trial 4, Plan View Temperature 40
Figure 35 – Welded Trial 4, Temperature Profile 40
Figure 36 – Welded Trial 5, Plan View Temperature 41
Figure 37 – Welded Trial 5, Temperature Profile 41
Figure 38 – Welded Trial 1, Trackline Comparison 43
Figure 39 – Welded Trial 2, Trackline Comparison 43
Figure 40 – Welded Trial 3, Trackline Comparison 44
Figure 41 – Welded Trial 4, Trackline Comparison 44
Figure 42 – Welded Trial 5, Trackline Comparison 44
Figure 43 – Example 2019 Data Trackline 48
Figure 44 – HAZ with Rule of Mixtures Only 50

Figure 45 – HAZ with Rule of Mixtures and Drude Model 50
Figure 46 – Temperature Profiles with an Emissivity of 0.1 51
Figure 47 – Temperature Profiles with an Emissivity of 0.5 51
Figure 48 – Original Placement of HAZ 52
Figure 49 – Modified Placement of HAZ 52
Figure 50 – COMSOL Model Mesh 53
Figure 51 – Welded Trial 1 Virtuoso Temperature Profiles 54
Figure 52 – Welded Trial 1 Virtuoso Data Points 54

Table of Equations

Equation 1 – Joule Heating Proportionality 9
Equation 2 – Skin Depth, Conductivity Formulation 10
Equation 3 – Skin Depth, Resistivity Formulation 10
Equation 4 – Electromagnetic Diffusion Equation, Time Domain 12
Equation 5 – Electromagnetic Diffusion Equation, Frequency Domain 13
Equation 6 – Induced Eddy Currents Within Sample 13
Equation 7 – Bulk Heating Resulting from Induction 13
Equation 8 – Heat Conduction Equation 13
Equation 9 – Convective Losses 13
Equation 10 – Radiative Losses 13
Equation 11 – Aggregate Heat Transfer Equation 14
Equation 12 – Relationship Between B and H Fields 14
Equation 13 – Temperature Dependence on Electrical Conductivity 16
Equation 14 – Phi Formulations of Conductivity and Resistivity 17
Equation 15 – Rule of Mixtures, Electrical Conductivity Formulation 17
Equation 16 – Stefan-Boltzmann Law for a Blackbody 21
Equation 17 – Generalized Stefan-Boltzmann Law 21
Equation 18 – Fractional Difference in Intensity Counts 21
Equation 19 – COMSOL Impedance Boundary Condition 28
Equation 20 – McAdams' Convective Heat Transfer Coefficient, Turbulent 29
Equation 21 – McAdams' Convective Heat Transfer Coefficient, Laminar 29
Equation 22 – Drude Model for Conductivity, DC Field 49
Equation 23 – Drude Model for Conductivity, AC Field 49
Equation 24 – Continuum Form of Ohm's Law, AC Field 49

Table of Tables

Table 1 – Simulation Parameters, Plate 23
Table 2 – Simulation Parameters, HAZ 24
Table 3 – Simulation Parameters, Coil 24
Table 4 – Simulation Parameters, Air Domain 25
Table 5 – 2018 Experimental Data Summary 31
Table 6 – 2019 Experimental Data Summary, Unsensitized 440C 31
Table 7 – 2019 Data Validation 32
Table 8 – Intensity Counts Added, Welded 440C 32
Table 9 – 2019 Experimental Data Summary, Welded 440C 33
Table 10 – Baseline COMSOL Results 36
Table 11 – Relative Error of Baseline Results 36
Table 12 – Welded COMSOL Data 41
Table 13 – Relative Error of Welded Results 42
Table 14 – COMSOL Capture Time Corrections 43
Table 15 – HAZ Temperature Errors 45

List of Acronyms

ASTM – American Society for Testing and Materials
DOS – Degree of Sensitization
EAC – Environmentally-Assisted Cracking
EC – Eddy Current
ECT – Eddy Current Thermography
EMAT – Electromagnetic Acoustic Transducer
EPR – Electrochemical Potentiodynamic Reactivation
HAZ – Heat Affected Zone
IGC – Intergranular Corrosion
IIRT – Induction Infrared Thermography
IR – Infrared
NDE – Non-Destructive Evaluation
NDT – Non-Destructive Testing
NLU – Nonlinear Ultrasonics
NUWCDIVNPT – Naval Undersea Warfare Center, Newport
PEC – Pulsed Eddy Current
RCF – Rolling Contact Fatigue
SEM – Scanning Electron Microscope
TTS – Time-Temperature-Sensitization

List of Units

A – Ampere
Btu – British Thermal Unit
°C – Degree Celsius
C – Coulomb
°F – Degree Fahrenheit
ft – Foot
H – Henry
Hz – Hertz
K – Kelvin
kg – Kilogram
J – Joule
m – Meter
Ω – Ohm
rad – Radians
s – Second
S – Siemen
V – Volt
W – Watt

1 Introduction

1.1 Sensitization Overview

The sensitization of stainless steels is a well-understood problem that affects an array of high-carbon alloys in a range of industries. This phenomenon describes the process by which a steel sample or component has its temperature raised (either naturally or artificially) above a critical threshold (in excess of ~1000° F [1, 2, 3]) for a given length of time followed by a cooling period. It is through this heating and cooling cycle that chromium carbides ($Cr_{23}C_6$) precipitate at the material's natural grain boundaries. With chromium being a primary contributor to a stainless steel's corrosion-inhibiting properties, the formation of these carbides depletes the grain boundaries of these benefits and leaves these regions susceptible to intergranular corrosion (IGC), environmentally-assisted cracking (EAC), and broader failure (see Figure 1). It is worth noting that while this concept of sensitization also applies to various aluminums, the method of action varies slightly. This is a topic of ongoing research and will not be discussed herein.

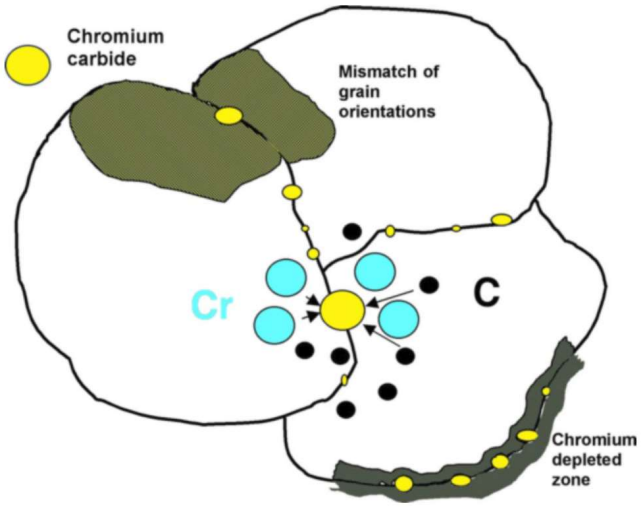

Figure 1 – Schematic of "Sensitized" Grain Boundaries [4]

Depending upon the alloy in question and, correspondingly, the amount of carbon present, the time/temperature relationship to sensitize a steel will vary but can be described in what is known as a time-temperature-sensitization (TTS) graph (an example for 304 stainless steel is shown in Figure 2 [4]). For sensitization to take place, the carbon content must be above approximately 0.08% by weight. Below this threshold, there is not a critical mass of carbon to combine with chromium for precipitates to appreciably form and thus sensitization becomes less of a concern. Additionally, as also seen in Figure 2, a decrease in carbon content, besides contributing less material to carbide creation, greatly increases the time to sensitize, making it even more difficult to achieve [5].

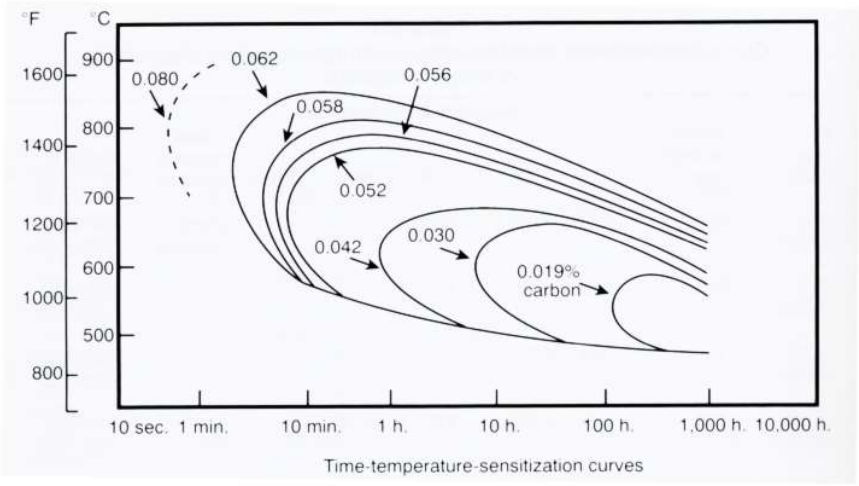

Figure 2 – Time-Temperature-Sensitization Graph of Type 304 Steel

Methods have been developed to detect sensitization in austenitic stainless steels, notably ASTM standard A262. While useful, the drawback of this family of tests is that they are destructive and/or qualitative in their results. For example, Practice B of this standard requires the boiling of test samples over a 120-hour period (5 days) in a mixture of ferric sulfate-sulfuric acid after which the resulting mass loss can be measured to draw conclusions on the corrosion rate [6]. It is evident that such processes could be a challenge for in-service material given the unlikelihood of a sample being available to be removed from its host. Therefore, it is desirable to find a solution that can provide comprehensive, *in-situ* evaluation of components before corrosion and cracking occur on a macro scale.

While there are established techniques to minimize the risk of sensitization occurring, such as low carbon ("L" grade) steels and the addition of stabilizing elements such as niobium or titanium [3], materials are still in use that are susceptible to this behavior and with limited means of nondestructive evaluation, there is room for more research to be conducted.

1.2 Motivation

One group who could benefit greatly from such a non-destructive means to test for sensitization is the U.S. Navy. Currently, there is specific guidance prohibiting post-weld heat treatments of austenitic stainless steels due to the inability to confirm that the material can resist corrosion after such a treatment [5].

In this context, Tucker et al. at the Naval Undersea Warfare Center, Division Newport (NUWCDIVNPT) have shown that sensitization behavior within stainless steels (namely 440C and 301 alloys) can be detected using a novel non-destructive evaluation (NDE) approach, applying induction infrared thermography (IIRT) to plates that have had sensitization introduced through welding [5]. This technique employs an infrared (IR) camera to capture the heat signature of a sample during and after electromagnetic induction heating. As sensitization within a metal alters the microstructure due to the congregation of carbides at the natural grain boundaries, the eddy currents that are induced within the workpiece via IIRT are forced to change directions to take the "path of least resistance" through the sample. This funneling and

crowding of the eddy currents to find the “path of least resistance” results in disproportionate heating (as compared with the parent metal) in these regions that can be detected with an IR camera for further analysis. In addition, the carbides are expected to have a higher resistivity than the healthy parent material [7] which will compound the increase in heating.

While sensitization does not have to be induced exclusively by welding, welding serves as a suitable, simple test case. The temperatures involved are sufficiently high to bring about carbide formation in a rapid manner. By using welded plates, different regions can be compared (both sensitized and unsensitized) as the sensitized regions are small compared to the overall scale of the piece. See Figure 3 for an example of welded plates that possess sensitization to either side of the weld. These sensitized regions cannot be seen with the naked eye, which highlights a further challenge of sensitization detection. As sensitization occurs on a microstructure level, simple inspection is not enough for detection; more robust methods are needed.

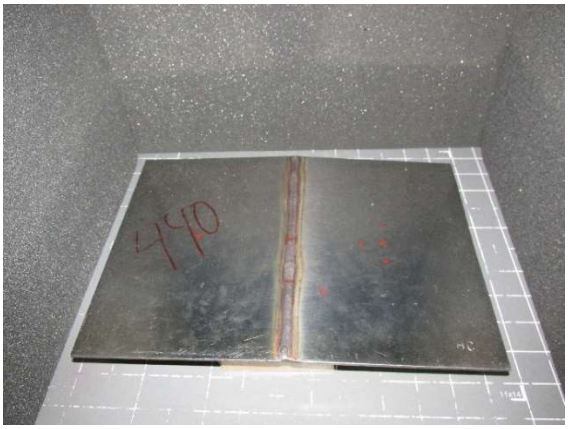

Figure 3 – Welded 440C Plate with Sensitized HAZ

During the welding process, several distinct regions are formed, as seen in Figure 4. Just outside of the fully-melted/mixed region, there are what are referred to as the heat affected zones (HAZ), where the microstructure has been modified but the temperature has not increased high enough to bring about melting. Depending on the alloy used, i.e. one that meets the thresholds for sensitization, sensitization can be induced in the HAZ. To this point, welded 440C stainless steel will be the focus here due to its high carbon content (approximately 1% [8]), allowing for prevalent sensitization and a strong contrast between the induction heating within the sensitized and unsensitized regions.

Note that there is separation between the HAZ and the weld with some of the unsensitized base material falling between the two regions. While this isn’t always the case, it is common to see this layout due to the temperature profiles seen in Figure 5 [3]. As previously discussed, both temperature and time are contributing factors to a given material’s ability to sensitize. Just outside of the welded region, the temperatures seen are above the critical range to bring about sensitization (see Figure 6 [3]) but do not stay in that range for long enough for sensitization to occur. However, moving further out in to the HAZ, the proper temperatures are experienced for enough time to see sensitization [3]. Moving even further away from the weld, the temperatures are too low for sensitization to initiate.

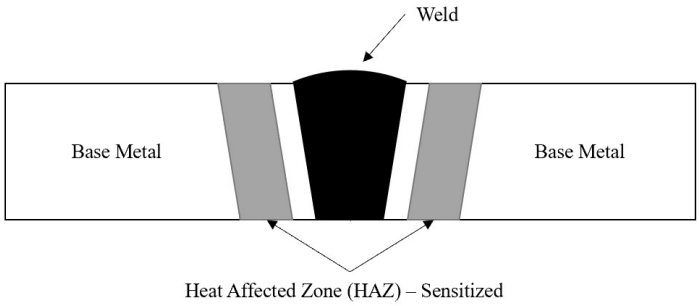

Figure 4 – Schematic of Weld/HAZ Regions

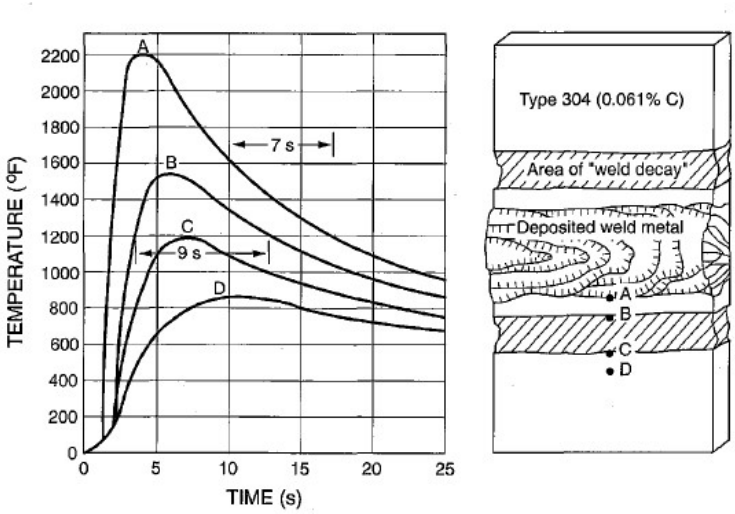

Figure 5 – Temperatures in Weld/HAZ Regions (304 Steel)

Temperature	Metallurgical Reactions	Remarks: Unstabilized Nb/Ti Absent (Type 304)	Remarks: Stabilized Nb/Ti Present (Type 321, 347)
Melting Point			
A	All carbides dissolve.	Rapid cooling prevents IGC.	Rapid cooling and reheating to *C* causes KLA. Reheating to *B* prevents KLA.
1230°C (2250°F)			
B	Niobium carbide precipitates. Chromium carbide dissolves.	Rapid cooling prevents IGC.	IGC prevented by precipitating dissolved carbide uniformly.
815°C (1500°F)			
C	Chromium carbide precipitates at grain boundaries.	Sensitization to IGC caused. precipitated at *B*. →	No sensitization. Nb/Ti Carbides
425°C (800°F)			
D	No reactions.	Temperature too low for adequate diffusion.	

Figure 6 – Temperature Ranges for Sensitization (304 Steel)

To verify that the observed temperature increases in the HAZ as a result of IIRT correspond to the presence of sensitization, micrograph images were taken of material samples cut from the parent plate. These 1" long by ¼" wide samples were cut transverse to the weld, and included the weld, the HAZ, and the base metal. Inspection of the SEM images provided physical evidence that the temperature spikes seen in the IIRT scans correlated with presence of sensitized material. Figure 7 shows a typical IIRT scan result with the small spikes in the red (post-heating) curve occurring around pixels 74 and 111. These corresponded to heating within the HAZ (the middle spike, corresponding to the weld itself, will be addressed later). These same regions are shown in Figure 8 where the micrograph clearly shows thickened grain boundaries consistent with sensitization. Together, these figures correlate disproportionate HAZ heating to the existence of sensitization [9].

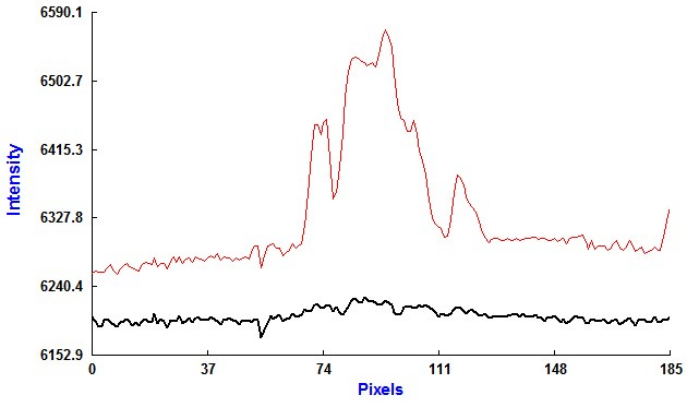

Figure 7 – Example IIRT Scan

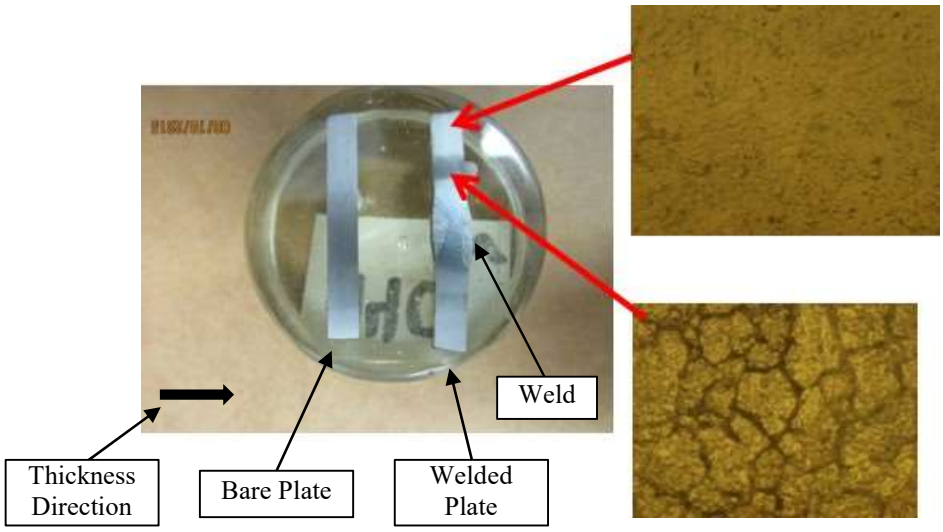

Figure 8 – Micrograph Images of 440C Steel

1.3 Accomplishments

This thesis had several specific accomplishments that will be discussed:

1. Building upon Tucker's previous work, the efficacy of the IIRT method in detecting sensitization was further validated.
2. Using scanning electron microscope (SEM) images along with new thermography trials, a quantitative correlation was drawn between a measured temperature rise and the presence of sensitized material.
3. This quantitative analysis of the experimental data was leveraged to populate a numerical model which accurately captured the varied heating within a sample.
4. The limitations and future potential of the model was explored in how it may be used to predict the level or degree of sensitization (DOS) of an arbitrary sample or component to make a real-time decision on its health rather than relying on destructive and/or qualitative methods.

2 Review of Literature

2.1 Non-Destructive Evaluation (NDE) and Non-Destructive Testing (NDT)

Non-destructive evaluation (NDE) and non-destructive testing (NDT) are a family of processes to evaluate materials for defects and/or changes in their microstructure that could result in material damage if performed in another manner. Besides being inherently nondestructive, these techniques offer the potential to rapidly detect flaws over a large area [10] as, such is the case with the ASTM sensitization tests, samples do not need to be taken from a host but can be evaluated in-place. There is a range of methods to accomplish this including millimeter wave imaging, magnetic particle inspection, and that of interest here, eddy current thermography.

2.2 Eddy Current (EC)/Eddy Current Thermography (ECT)

Eddy current techniques make up a broad group of test methods that includes the one of interest here, IIRT. In each application, the premise is similar: eddy currents are induced within a workpiece in a known flow pattern, where the flow is disturbed by a physical difference in the part, typically a defect or crack. The presence of this discontinuity results in the behavior previously outlined where the eddy currents are forced to take alternate paths that generate differing signatures (heat signatures in the case of thermography techniques) when compared to what would be witnessed in the same material with no abnormalities [11, 12]. These areas with altered paths can then be seen with an infrared camera or other detector and analyzed/characterized to make predictions on the shape, size, etc. of the abnormality. This technique has consistently proven itself to be a reliable test method and one worth exploring in attempting to detect sensitization.

Several researchers [10, 13] have presented useful summaries of this technique, demonstrating that asymmetric heating (as theorized) can be seen when heating a sample with defects present. Regarding specific applications, Netzelmann et al. looked at induction thermography to detect defects in forged components, showing that not only could the defects be found but that it had benefits over magnetic particle inspection typically used by a manufacturer [14]. Peng et al. showed the viability of ECT in rolling contact fatigue (RCF), a type of damage to train rails that can lead to catastrophic accidents [15]. Further work was done by Oswald-Tranta et al. [16] regarding the thermographic testing of surface cracks in steel wires, Świderksi in using ECT for subsurface defects in both steel and aluminum in the context of the marine industry [17], and

Vasic et al. in oil well piping, using pulsed eddy currents (PEC) to detect the thickness of ferromagnetic tubes [18].

Naturally, there are many variables that impact these techniques and much exploration has also been done in this regard, further showing its flexibility in a range of scenarios. He et al. [19] performed similar eddy current thermography work to those listed above but investigated the use of moving a sample underneath an excitation coil to capture a larger surface area, thus exploring one of the benefits of this technique over other NDE/NDT methods. Yang et al. leveraged a PEC technique to investigate edge cracks rather than those just on a surface [20] while Abidin et al. have shown the differing ECT heat signatures associated with angled cracks [10, 21]. In additional work by Oswald-Tranta et al. [22], she showed the different heating behaviors seen in magnetic vs. non-magnetic materials, specifically how the former produces asymmetric spikes and the latter produces asymmetric dips in heat signature.

While eddy current and eddy current thermography techniques must be done in a conducting medium (typically metals), broader thermography research has been conducted that further show its merits within other materials. For example, Cannas et al. showed the viability in detecting subsurface cavities and defects in concrete structures by using heat lamps to generate a characteristic asymmetric heating pattern [23]. Li et al. used induction thermography to detect flaws in composite panels that do possess some conductivity (like a metal) but have the added complexity of possessing anisotropic material parameters [24].

2.3 NDE/NDT to Detect Sensitization

Regarding sensitization, there is a small body of work that has been done to develop non-destructive evaluation and test methods, with some early results showing promise. Shaikh et al. attempted an eddy current technique to correlate eddy current amplitudes to a DOS, both in aged samples and in samples that had previously undergone the ASTM A262 Strauss test [25]. Kikuchi et al. have explored a technique to detect sensitization in samples using a Hall sensor, measuring differences in magnetic properties due to the presence of sensitization [26].

Several researchers have explored the use of sound propagation within a material to detect subtle changes in velocity. Abraham et al. used nonlinear ultrasonics (NLU) in the context of nuclear power plants due to their use of austenitic stainless steels to detect sensitization [27]. This method drew a correlation between ASTM testing of the DOS and the ratio of the first and second harmonic amplitudes. Similarly, Cobb et al. used ultrasound in aluminum samples, specifically EMAT (electromagnetic acoustic transducer) ultrasound to correlate velocity ratios to a DOS [28]. Stella et al. showed that a difference in low and high levels of sensitization could be qualitatively resolved through differences in their ultrasonic attenuation and power spectra [29].

A handful of developments have also taken place in the field of electrochemical potentiodynamic reactivation (EPR) testing. Park holds a U.S. patent on an electrochemical device that evaluates the current-voltage relationship of a sample subjected to a series of tests, enabling the user to tell if sensitization is present [30]. A similar concept to that of Park has been employed by ElectraWatch in a portable instrument to detect sensitization in aluminum using an electrochemical measurement that provides results in agreement with the destructive ASTM G67

method (this method can be taken as the aluminum equivalent of the ASTM 262 tests) [31]. More formally, ASTM G108 uses an EPR test to quantify the level of sensitization in 304 and 304L steels [32].

2.4 Challenges and Knowledge Gaps

EC and ECT methods have proven to be successful and useful in a range of industries and contexts but there are several drawbacks. To detect cracks, the short heating times required can necessitate sophisticated equipment to be able to resolve the rapid temperature increases, as illustrated by Yang et al. [20]. Even though He et al. were able to leverage one of ECT's largest advantages (sweeping a large test area), challenges were seen in using the appropriate sweep speed to properly process the images [19]. Additionally, in the case of cracks, some knowledge about the defects would be useful to know *a priori* as the amount of heat needed for proper resolution can vary widely depending upon the depth, orientation, size, etc. of the crack defect(s), as well as the material parameters [10, 22]. Walle et al. illustrated such a drawback by using frequencies far lower than that seen in many experiments to detect deeper cracks [12]. In other words, using a "one size fits all" approach is not always conducive to detecting all types of defects; multiple scans may be needed to characterize certain flaws.

Previous research on developing viable NDE techniques to detect sensitization exhibited some limitations. Shaikh et al.'s work with eddy currents produced more definitive results in specimens that had previously been exposed to the destructive Strauss test, a condition that is likely infeasible in fielded material [25]. Kikuchi et al.'s experiments, while promising, have only been validated in highly controlled specimens, thus necessitating more experimentation before conclusions can be drawn [26].

Abraham's method of ultrasonic testing is highly sensitive to the grain structure of the material such that there could be interference from other nonuniformities present [27]. Cobb et al. could only detect high states of sensitization in their testing [28], while Stella et al. showed challenges in drawing quantitative conclusions using their techniques [29].

The probe that was patented by Park uses a capillary tube, which necessarily restricts it to a small test area. In addition, the electrolyte reservoir used must be replenished between each test, harming the ability to give rapid results [30]. The portable apparatus from ElectraWatch must be left to operate for 75 minutes in an area that has been specifically prepared, which is not always a possibility [31]. Within the ASTM G108 test, the only alloy that it is suited for is 304 stainless steel and it is still recommended to have a microstructure analysis performed after it is run, thus limiting its overall applicability [32].

When compared to the detection of cracks, ECT has a few clear benefits as a potential tool to detect sensitization. As sensitization is brought about by a large fluctuation in temperature, it will either occur on a global scale or at a known concentration point such as near a weld. This means that, when compared to crack detection, the tester already has an idea of where to inspect and the concern of missing a flaw is minimized. Sensitization also creates a more homogeneous change in the nature of the material, helping to negate the issues introduced by crack orientation, size, and depth. Fine-tuning can be done to capture specific heat signatures but even a modest treatment of the parameters can yield suitable results.

With the limited non-destructive methods researched for the testing of sensitization, in combination with the limited accepted test methods (namely the ASTM standards), there is room for expansion. This thesis aims to meld the benefits of eddy current techniques (namely the rapidity and scale of testing and the ability to perform it in-place) with the attempts made at non-destructively characterizing sensitization, to introduce a new, alternative technique to quantify this material state.

3 Design and Methodology

3.1 Governing Equations

3.1.1 Overview

Electromagnetic induction is a coupled process that marries two branches of physics: (1) electromagnetism as described by Maxwell's equations and (2) heat transfer, as described by Fourier's law of heat conduction (it should be noted that convection and radiation are also factors in the heat transfer portion of this process, which will be addressed later) [33]. By placing an induction coil near a conductive sample or component and passing an alternating current through it at a prescribed frequency, a rapidly-varying magnetic field is created that penetrates the object and induces eddy currents near its surface [34, 35]. A schematic of a typical induction heating setup can be seen in Figure 9 [11].

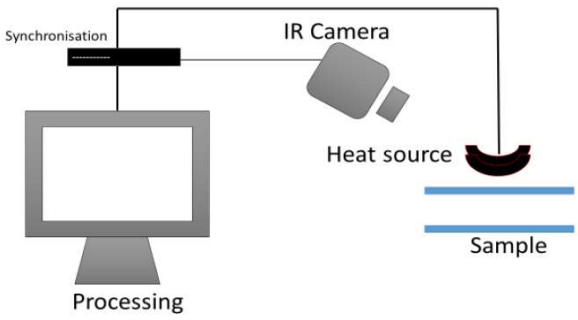

Figure 9 – Schematic of Typical Induction Heating Setup

The induced currents flowing within the sample will generate heat through Joule heating at a level that is proportional to the resistance within the material. Joule heating is described through the following [36]:

$$P \propto I^2 R$$

Equation 1 – Joule Heating Proportionality

Here, P is the power in W, I is the current in A, and R is the resistance in Ω.

A material with a high conductivity has a correspondingly low resistivity (which is found as the inverse of conductivity) [37] and will take longer to heat than a material with a lower conductivity and higher resistivity. For example, a highly conductive material, such as copper

(5.8e7 S/m [8]) or silver (6.5e7 S/m [8]), allows the eddy currents to pass more freely, thus limiting the build-up of heat in a given time. In contrast, the 440C of interest has a conductivity of approximately 1.7e6 S/m [8], one order of magnitude lower than that of copper, which should yield more rapid heating in response to a given coil with the same applied current, etc.

This resistive heating can be compounded by hysteresis losses when the material being heated is ferromagnetic, i.e., one that is inherently magnetic, like nickel. In ferromagnetic materials, the changing magnetic field results in a continual realignment of the molecules that generates heat through friction. However, this heating is considered secondary and will not be treated further [38, 39, 40].

3.1.2 Skin Depth

A consideration of critical importance for IIRT is that of skin depth, which represents the depth of penetration of the eddy currents in to a material at which point their amplitude is 1/e (≈0.368) times that seen at the surface. This depth can be described as follows [41, 42]:

$$\delta = \sqrt{\frac{1}{\pi f \mu_0 \mu_r \sigma}}$$

Equation 2 – Skin Depth, Conductivity Formulation

Here, f is the excitation frequency in Hz, μ_0 is the permeability of vacuum (4π e-7 H/m), μ_r is the dimensionless relative permeability of the material, and σ is the electrical conductivity of the material in S/m.

An equivalent form can be written by using the fact that the resistivity of a material (ρ) is the inverse of its conductivity (σ):

$$\delta = \sqrt{\frac{\rho}{\pi f \mu_0 \mu_r}}$$

Equation 3 – Skin Depth, Resistivity Formulation

Here, ρ is the resistivity in Ω-m.

From observation of these equations, either an increase in frequency or permeability, or a decrease in resistivity (equivalent to an increase in conductivity), will lower this skin depth. In the limits of these conditions, the penetration depth of the eddy currents will tend to 0. This allows for a simplification within a numerical model where the eddy currents are assumed to only congregate near the surface and penetrate a negligible amount into the material (this will be discussed in more detail later).

3.1.3 Maxwell's Equations

One of the primary governing equations comes in the form of the magnetic vector potential formulation of the electromagnetic diffusion equation derived from Maxwell's equations:

$$i\omega\sigma \boldsymbol{A} - \frac{1}{\mu}\nabla^2 \boldsymbol{A} = \boldsymbol{J}_S$$

To arrive at this result, the following derivation is undertaken [41, 43, 44]:

1. From Gauss' Law for Magnetism, the divergence of a magnetic field (**B**) is 0, i.e. the magnetic field is solenoidal:

$$\nabla \cdot \boldsymbol{B} = 0$$

2. Knowing that the divergence of the curl of a vector field is 0, the magnetic field can be written in terms of **A**, the magnetic vector potential:

$$\boldsymbol{B} = \nabla \; x \; \boldsymbol{A}$$

3. From Maxwell's Law of Induction, the curl of an electric field (**E**) is equal to the negative time derivative of the magnetic field:

$$\nabla \; x \; \boldsymbol{E} = -\frac{\partial \boldsymbol{B}}{dt}$$

4. Substituting line (2) in to the right-hand side of line (3) for **B**:

$$-\frac{\partial \boldsymbol{B}}{dt} = -\frac{\partial}{dt}(\nabla \; x \; \boldsymbol{A}) = -\nabla \; x \; \frac{\partial \boldsymbol{A}}{dt}$$

5. Putting this back in to line (3) and moving everything to the left-hand side:

$$\nabla \; x \; \left(\boldsymbol{E} + \frac{\partial \boldsymbol{A}}{dt}\right) = 0$$

6. Because the curl of a gradient of a vector field is 0, one possible solution to line (5) is the following (note that φ is the electric scalar potential):

$$\boldsymbol{E} = -\frac{\partial \boldsymbol{A}}{dt} - \nabla\varphi$$

7. The solution in line (6) can be interpreted to be a combination of an induced electric field and an applied electric field:

$$\boldsymbol{E} = -\frac{\partial \boldsymbol{A}}{dt} - \nabla\varphi = \boldsymbol{E}_{induced} + \boldsymbol{E}_{applied}$$

8. Multiplying the electric field by the electrical conductivity (σ), the result relates current density (**J**) to the magnetic vector potential (the continuum form of Ohm's law):

$$\boldsymbol{J} = \sigma \boldsymbol{E} = -\sigma \frac{\partial \boldsymbol{A}}{dt} - \sigma \nabla \varphi = -\sigma \frac{\partial \boldsymbol{A}}{dt} + \boldsymbol{J_s}$$

9. The current density on the left-hand side of line (8) can be equivalently written (using Ampere's law with μ equal to the magnetic permeability) as:

$$\boldsymbol{J} = \nabla \, x \, \frac{1}{\mu} \boldsymbol{B}$$

10. Substituting line (9) in to line (8) and using the relation between **A** and **B** from line (2):

$$\nabla \, x \, \frac{1}{\mu} \boldsymbol{B} = -\sigma \frac{\partial \boldsymbol{A}}{dt} + \boldsymbol{J_s}$$

$$\nabla \, x \, \nabla \, x \, \boldsymbol{A} = -\mu\sigma \frac{\partial \boldsymbol{A}}{dt} + \mu \boldsymbol{J_s}$$

11. Through vector identities, the curl of the curl of the magnetic vector potential is represented as:

$$\nabla \, x \, \nabla \, x \, \boldsymbol{A} = \nabla(\nabla \cdot \boldsymbol{A}) - \nabla^2 \boldsymbol{A}$$

12. This can be simplified by imposing the Coulomb gauge condition which says [45]:

$$\nabla \cdot \boldsymbol{A} = 0$$

13. After applying this gauge condition and substituting back into line (10), the final form of the diffusion equation in the time domain results:

$$-\nabla^2 \boldsymbol{A} = -\mu\sigma \frac{\partial \boldsymbol{A}}{dt} + \mu \boldsymbol{J_s}$$

Equation 4 – Electromagnetic Diffusion Equation, Time Domain

14. Assuming the magnetic vector potential is harmonic, this diffusion equation can be moved from the time domain in to the frequency domain using a phasor transformation of the form:

$$\boldsymbol{A} = Ae^{i\omega t} = A\big(cos(\omega t) + isin(\omega t)\big)$$

15. Taking the time derivative yields:

$$\frac{\partial \boldsymbol{A}}{\partial t} = i\omega A e^{i\omega t} = i\omega \boldsymbol{A}$$

16. Substituting this back in to line (13) provides the desired result:

$$\boldsymbol{J_s} = i\omega\sigma\boldsymbol{A} - \frac{1}{\mu}\nabla^2\mathbf{A}$$

Equation 5 – Electromagnetic Diffusion Equation, Frequency Domain

Here, $\mathbf{J_s}$ is the current density of the source in A/m^2, ω is the angular frequency in rad/s, **A** is the magnetic vector potential in A-s/m, and μ is magnetic permeability in H/m.

The final magnetic vector potential, **A**, is found by solving this diffusion equation in the frequency domain. Upon finding the solution for the magnetic vector potential, the eddy currents in the plate are described by [41]:

$$\boldsymbol{J} = -i\omega\sigma\boldsymbol{A}$$

Equation 6 – Induced Eddy Currents Within Sample

3.1.4 Heat Transfer

Once the eddy currents are induced within a sample, the resultant bulk heating generated by induction is represented by [10, 46]:

$$q_{ind} = \frac{1}{\sigma}|\boldsymbol{J}|^2$$

Equation 7 – Bulk Heating Resulting from Induction

This induced heat is then used as the source term in Fourier's law of heat conduction to describe the conduction through the workpiece [10]:

$$\rho C_p \frac{\partial T}{\partial t} - \nabla \cdot (k\nabla T) = q_{ind}$$

Equation 8 – Heat Conduction Equation

Here, ρ is the density of the material in kg/m^3, T is the temperature in K, k is the thermal conductivity in W/(m-K), and C_p is the specific heat in J/(kg-K).

Heat losses are also present due to both natural convection and radiation which are represented by [23]:

$$q_{conv} = h(T - T_\infty)$$

Equation 9 – Convective Losses

$$q_{rad} = \varepsilon\sigma(T^4 - T_\infty^4)$$

Equation 10 – Radiative Losses

Here, h is the convective heat transfer coefficient in W/(m^2-K), T_∞ is the ambient temperature in K, and ε is the dimensionless emissivity.

Subtracting these losses from the heat conducted through the sample, the aggregate heat transfer equation is:

$$\rho C_p \frac{\partial T}{\partial t} - \nabla \cdot (k \nabla T) = q_{ind} - q_{conv} - q_{rad}$$

Equation 11 – Aggregate Heat Transfer Equation

This equation is solved in the time domain to find the heat at a given time and location in the workpiece.

3.2 Limitations and Assumptions

There are two primary factors that can introduce additional nonlinearities in to Equation 5, but these can also be sufficiently simplified.

One limitation comes with ferromagnetic materials (such as 440C) as they possess a time-dependent relative magnetic permeability (μ_r). This relative magnetic permeability relates the magnetic field (**B**) and magnetic field strength (**H**) through [47]:

$$\boldsymbol{B} = \mu_r \mu_0 \boldsymbol{H} = \mu \boldsymbol{H}$$

Equation 12 – Relationship Between B and H Fields

In what is known as a B-H curve or its corollary, a hysteresis loop, these B and H values are graphically related with the instantaneous slope of the curve representing the relative magnetic permeability. In a linear material, the magnetic permeability does not vary, and this slope is a constant value as seen in the blue (vacuum) curve in Figure 10 [48].

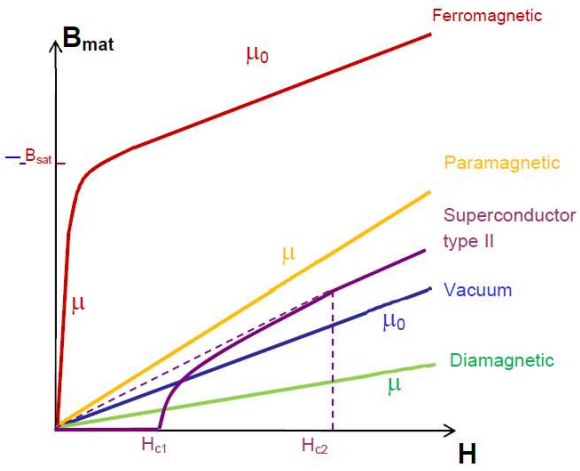

Figure 10 – Typical B-H Curves

However, in a material such as 440C steel, depending upon the value for H, the curve will not always be linear, meaning that the value for μ_r can change over time. A generic hysteresis loop for a ferromagnetic material is shown in Figure 11 [47].

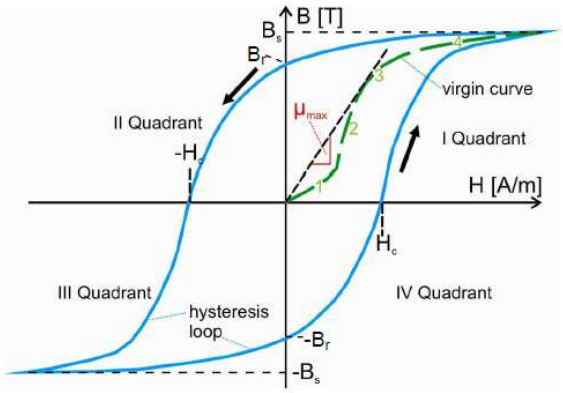

Figure 11 – Generic Ferromagnetic Hysteresis Loop

Two conditions within the experimental setup used allow for the simplification of this relative magnetic permeability to one value:

1. The green curve in Figure 11 is the area of operation of the experiments, that is, low values of H where the slope (relative magnetic permeability) can be approximated by one value. This range represents the time before saturation of the material when irreversible changes are made to its magnetic properties (at which point the blue curve would be followed).
2. The coil used in the conducted IIRT experiments, through an on/off switch, had what can be considered an instantaneous application of current [22]. Therefore, during each experimental trial, the value for H would rise to a consistent value along the green curve and correspond to a consistent slope (relative magnetic permeability).

While not an exact representation of the material being used, a B-H curve of 416 stainless steel is seen in Figure 12 where this permeability value holds relatively constant at low values of H [49]. In the IIRT experiments described herein, for a solid conductor coil, i.e. one with a single turn, with an applied current less than approximately 40 A (in the limiting case as seen later) and a total length of 1 m, the H value will be less than 40 A/m, sufficiently small to approximate the relative magnetic permeability as a single value.

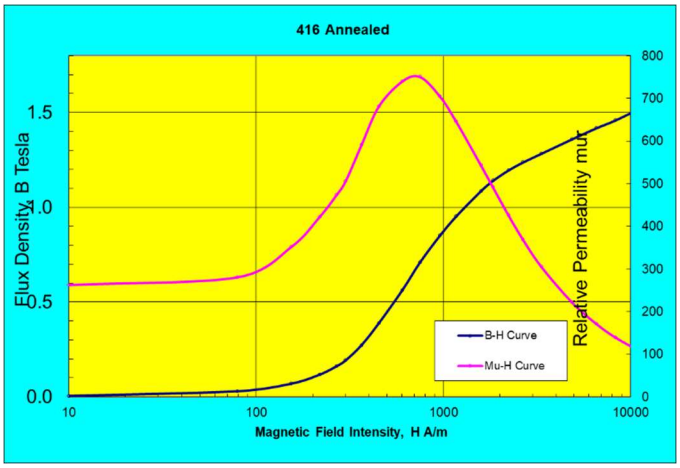

Figure 12 – B-H Curve of 416 Steel

The second assumption can be made regarding the electrical conductivity, which, in a thorough treatment, is dependent on the temperature through Equation 13 [10, 20].

$$\sigma = \frac{\sigma_0}{1 + \alpha(T - T_0)}$$

Equation 13 – Temperature Dependence on Electrical Conductivity

Here, σ_0 is the reference conductivity in S/m which is found at a reference temperature, T_0, α is the temperature coefficient of resistivity in inverse units of temperature, and T is the new temperature.

As the temperature increases experienced in the lab were less than 3 °C, for a 440C plate whose initial temperature was room temperature (approximately 24 °C), the new conductivity of the plate would vary by less than 1% [9, 50]:

$$\sigma = \frac{\sigma_0}{1 + \alpha(T - T_0)} = \frac{1.4706e6\ S/m}{1 + 0.00094/°C(27\ °C - 24\ °C)} = 1.4664e6\ S/m$$

Note that the value for the temperature coefficient of resistivity used was that of 18-8 steel but even using the more conservative value for pure iron (0.006/°C [50]), the change is still less than 2%. With such a small variation in the conductivity, it was assumed that this variability could be acceptably neglected.

3.3 Description of Phi (Φ)

While a given material has an inherent conductivity (and resistivity) due to its microstructure, the presence of sensitized material alters these values and results in differing induction heating behavior. As shown by Tucker, the presence of sensitized regions within a sample yields disproportionate heating above what would be expected within an unsensitized sample [5]. The hypothesis is that there are two contributions that drive this spike in heating [9]:

1. The carbide precipitates possess a higher resistivity than the original alloy, which helps to increase the level of heating in the sensitized regions.
2. The presence of the chromium carbide precipitates at the grain boundaries will force the eddy currents to take altered paths to find the "path of least resistance" through the sample, resulting in increased heating due to longer distances traveled.

The goal was to relate the microstructure changes due to sensitization to a change in bulk conductivity/resistivity such that a single value could be changed within the numerical simulations rather than requiring explicit modeling of the grain boundaries, which would be computationally intensive. A factor, phi (Φ) was introduced as a multiplier to increase the resistivity of the original material within sensitized regions (the HAZ in this case).

Per the Joule heating relationship, a higher resistivity (or equivalently, a lower conductivity) would yield an increase in the level of heating seen in the sensitized regions, or:

$$\sigma_{sensitized} = \frac{\sigma_{original}}{\Phi}$$

$$\rho_{sensitized} = \Phi \rho_{original}$$

Equation 14 – Phi Formulations of Conductivity and Resistivity

The rule of mixtures was used in conjunction with SEM images to help bridge the gap between heat signature and the physical presence of chromium carbides to develop this factor. This technique allows for a weighted mean to be taken of differing material properties within a composite material to yield a single equivalent value [51, 52] (see Equation 15).

$$\left(\frac{f}{\sigma_1} + \frac{1-f}{\sigma_2}\right)^{-1} \leq \sigma_{mix} \leq f\sigma_1 + (1-f)\sigma_2$$

Equation 15 – Rule of Mixtures, Electrical Conductivity Formulation

Here, f represents the decimal fraction of sensitized material within a given test area, σ_1 is the conductivity of the chromium carbide precipitate in S/m, and σ_2 is the conductivity of the parent 440C in S/m.

An upper and a lower bound are found between which lies the value for σ_{mix}, representative of the value that the conductivity could take on. If f is set equal to 1, the upper and lower bounds will be identical to that of pure chromium carbide and if it is set to 0, the upper and lower bounds will be identical to that of pure 440C. In a real scenario, f falls somewhere between 0 and 1.

This rule of mixtures and the resulting value of Φ only contributes to the first piece of the difference in conductivity within sensitized material. Using only the rule of mixtures to determine the value of Φ assumes that in the sensitized material, the eddy currents can flow in the same manner as those in the original material, albeit in a material with a lower bulk conductivity (higher bulk resistivity). As hypothesized above, there is an additional contribution

to the lowering of conductivity due to the path length increase that eddy currents must take. See the Discussion section for more on how this second contribution was explored.

3.4 Image Processing

To establish the basis for the rule of mixtures model (the value for "f"), the goal was to process SEM images through the open source software ImageJ. Here, the amount of sensitized material can be found as a percentage of the total image size such that this fraction could be input to the rule of mixtures model (for reference, the raw image shown in Figure 13 and the processed result in Figure 14 show that ~8% of the total area is sensitized in 301 steel samples). This should provide the bounds on the rule of mixtures to allow for the first conductivity adjustment. For more specifics on this process, refer to Appendix A.

Optimal SEM images of the sensitized grain structure of the 440C specimens were not able to be obtained due to technical and scheduling challenges. These challenges included (1) unforeseen difficulties in procuring chemicals and preparing samples of the 440C in a manner optimal for viewing sensitized grain boundaries, and (2) emergent equipment repair needs at NUWCDIVNPT. To continue with the analysis, the results seen for the 301 steel were used as a foundation (that is, an 8% (0.08) sensitization fraction) as described in the Discussion section.

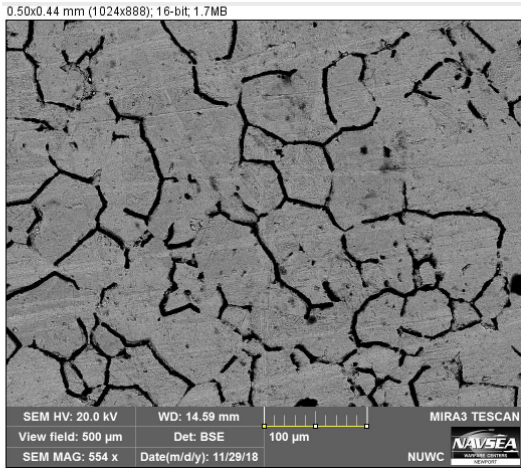

Figure 13 – Example Raw SEM Image (301 Steel)

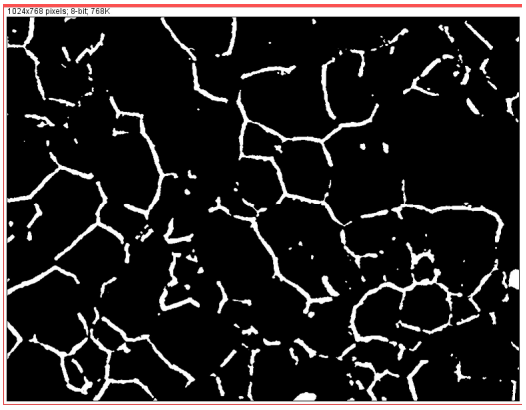

Figure 14 – Example SEM Image (301 Steel) Processed with ImageJ

3.5 Experiments

Laboratory experiments were conducted between May and July 2018 and between January and March 2019 at NUWCDIVNPT. The typical experimental setup can be seen in Figure 15.

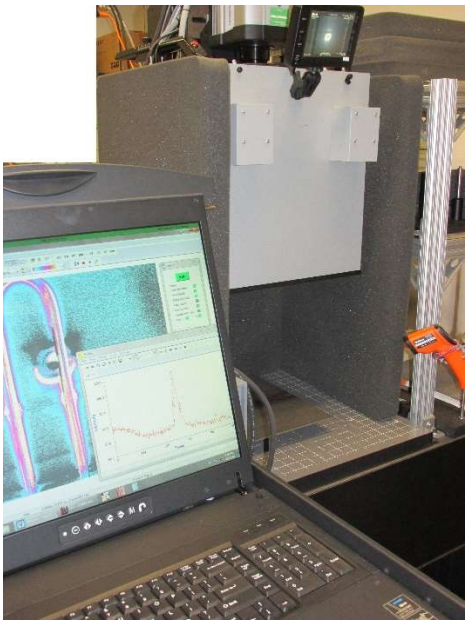

Figure 15 – Experimental Setup

The goal of the first set of experiments was to draw a correlation between the analog intensity counts that were observed by the overhead infrared camera and processed in Thermal Wave Imaging Inc.'s Software, Virtuoso, with a measured increase in temperature due to induction heating. As previously theorized and demonstrated by Tucker, regions that possessed sensitized material should show a disproportionate increase in temperature. Developing this correlation would allow for a wide-range of interpretation to be performed and enable the development of the numerical simulations.

3.5.1 Proof-of-Concept Data (2018)

The initial experiments performed in 2018 were run with the following procedure:

1. The shroud containing the FLIR infrared camera was raised to a specified height above the workbench.
2. A metal sample was placed on the bench underneath the camera and supported by cardboard boxes to decouple the heating from the table.
3. The camera was brought in to focus above the sample to ensure that the images and data taken were free of distortions and aberrations.
4. A background thermal scan was performed in conjunction with a temperature reading with an infrared thermometer to relate the radiation seen by the camera with a steady-state temperature.
    a. This temperature reading and intensity measurement were both read within the welded region as this had been shown in early tests to yield the largest temperature

increase and would thus be easy to discern and extract from the IIRT data. As the goal was to relate intensity counts to temperature, finding such a maximum (one data point) would suffice rather than trying to capture the global heating.

b. A 2” trackline was used in Virtuoso to visualize the heating along a 2” line along the surface of the plate. The trackline was placed outside of the coil boundaries and spanned both HAZ regions and the weld.
c. The thermometer was held in place with a lab stand and clamp to assure a consistent measurement location test-over-test.

5. An electromagnetic coil (a flat, “pancake” shape, see Figure 16 [9]) was placed above the sample of interest and energized with an external power supply.

Figure 16 – "Pancake" Coil

6. This excitation was performed for a designated period (on the order of seconds) with the coil held in a fixed location before being removed.
7. After heating, a final temperature was taken with the infrared thermometer in the same position as the baseline reading.
8. The heated intensity data was collected and compared against the baseline data taken earlier (an example can be seen in Figure 17 where the black line is the baseline profile and the red line is the profile after heating).

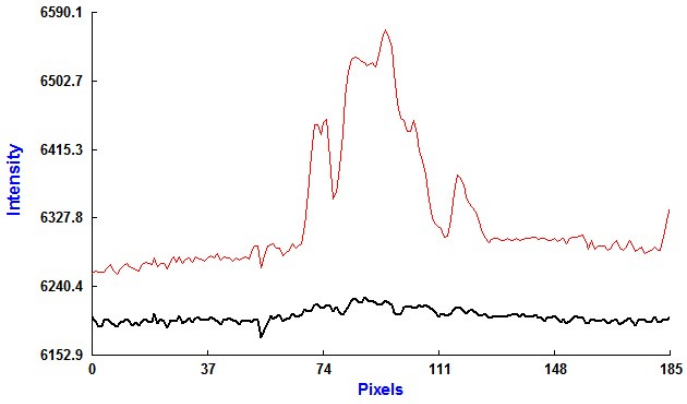

Figure 17 – Example Background/Heated Scan

It should be noted that one 440C sample was the focus of these trials despite a few being available. A welded 440C sample was used that had no surface treatments done (painting, grit-blasting, etc.) to limit the variability in heating behavior. For example, a painted sample, with an additional layer of material on its surface, introduces a new thermal diffusivity parameter that only serves to add complexity to the model rather than allowing for the focus to be specifically on the plate's thermal response.

A realization was made in early testing that the difference in the baseline and heated intensity count profiles was not a linear relationship that could be applied across any test setup. Rather, there was a wide variation in the output based on which plate was being tested (for instance, those plates with a surface treatment applied) and between alloys (both 440C and 301 were explored in early trials).

To account for this, the relationship described in the Stefan-Boltzmann law was employed to relate intensity counts to temperature. This law relates the total energy radiated to the fourth power of temperature [53]:

$$E = \sigma T^4$$

Equation 16 – Stefan-Boltzmann Law for a Blackbody

$$E = \varepsilon \sigma T^4$$

Equation 17 – Generalized Stefan-Boltzmann Law

Here, E is the radiant heat energy emitted per unit area (across all wavelengths) per unit time, ε is the dimensionless emissivity of the material, σ is the Stefan-Boltzmann constant (5.67e-8 W/(m^2-K^4)), and T is temperature in K.

There are two forms of this equation with the more general being represented in Equation 17 as it accounts for the emissivity, ε, of the sample allowing for an arbitrary material to be analyzed rather than a perfect blackbody as in Equation 16 [54]. In both cases, it is evident that radiated heat energy is proportional to temperature through:

$$E \propto T^4$$

Leveraging this relationship, several post-processing steps were then undertaken after each trial to predict what the temperature rise should be based on the increase of intensity counts (a measure of radiated energy) from the baseline to the final heated value:

1. The relative fractional difference in intensity counts between the baseline and the heated profile at the point of largest increase (within the weld) was found:

$$Difference = \frac{|Heated\ Intensity\ Counts - Baseline\ Intensity\ Counts|}{Baseline\ Intensity\ Counts}$$

Equation 18 – Fractional Difference in Intensity Counts

2. This difference was then added to 1 to create a multiplier, i.e. a fractional difference of 0.05 was transformed in to a value of 1.05.
3. This multiplier was raised to the ¼ power in line with the Stefan-Boltzmann law to create a new multiplier to be used for computing the temperature.
4. The baseline temperature was multiplied by this factor to estimate what the new temperature should be based on the change seen in intensity counts.
5. The predicted temperature value was compared with the measured value.

One of the most important considerations in this testing (and the testing moving forward) was the elimination of emissivity. By measuring singular points before and after heating without comparing the global heating changes, emissivity variations within the plate would not need to be considered because the emissivity at one point before and after testing should remain the same. Refer to the Discussion section for more on emissivity and how it is neglected in this analysis.

3.5.2 Simulation Data (2019)

The 2019 experiments followed a similar set of steps but with some notable differences. In particular, the focus of the data was on varied heating and settling times to help seed the numerical model and less on the establishment of the intensity-temperature correlation that had previously been addressed. The measurements taken, rather than relying solely on a relative difference in intensity counts, set the baseline to 0 and allowed the heating to increase the intensity counts from there. As a result, the postprocessing procedure was amended as follows:

1. Find the relative difference in intensity counts between the final value at the end of the settling time and the value at the maximum point of heating when the coil was removed.
2. This difference was then added to 1 to create a multiplier, i.e. a fractional difference of 0.05 was transformed in to a value of 1.05.
3. The final temperature was multiplied by this factor to estimate what the temperature rise at the plate's "hottest" point should be based on the change seen in intensity counts.
4. The predicted maximum temperature value was used as a point of comparison for the model.

The following additional changes were made in this set of experiments:

1. The coil shape used was changed from a "pancake" to a hairpin (see Figure 18)
    a. In 2018, the "pancake" coil was used as the plate was placed under the IR camera as seen in Figure 16 with the weld running towards and away from the viewer. This was done to minimize reflections from the camera and yield more stable results. As a side effect, the hairpin coil could not be used as it could not easily be placed across the HAZ and weld regions. In these later experiments, the plate was rotated 90 degrees, a scenario where the hairpin could be properly aligned.

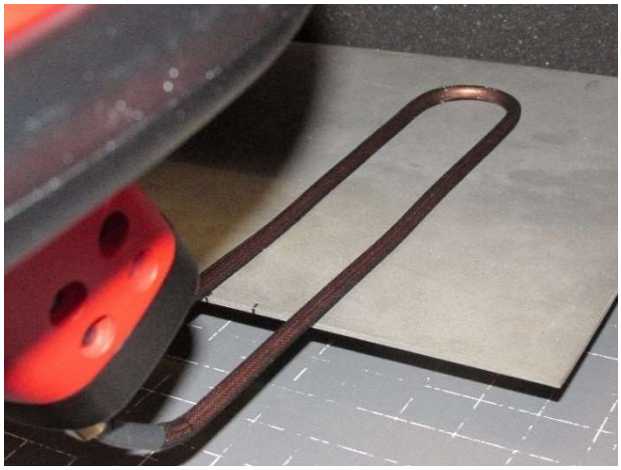

Figure 18 – Hairpin Coil

2. The heating and settling times were varied to capture a wider range of behavior.
3. Besides only using a trackline to measure intensity counts, discrete measurement points were also used in Virtuoso to capture the heating within the HAZ and weld.

An additional consideration used to help inform the numerical model was the induction heating of bare 440C samples, i.e. ones with no sensitization present. This scenario provided a benchmark to verify that the simulation was populated with the correct initial parameters (current, relative magnetic permeability, etc.) before handling the variable of sensitization.

3.6 Numerical Simulations

COMSOL Multiphysics 5.3a and its AC/DC Module were employed to create and numerically solve the induction heating problem. Per the experimentation performed at NUWCDIVNPT, the model parameters for the 440C plate and the HAZ regions were directly imported into the model. Regarding the coil and the air, the COMSOL-provided values were used with the only adjustment made to the air's conductivity. By default, it is provided as 0 S/m but for numerical stability, it was increased to 1 S/m. These parameters are shown in Table 1, Table 2, Table 3, and Table 4 [5, 55, 56]. Refer to the Discussion section for more information on the parameter selection/derivation.

Plate Dimensions (LxWxH)	12" x 8" x 0.125"
440C Density	7700 kg/m^3
440C Conductivity	1.4706e6 S/m
440C Relative Permeability	700
440C Relative Permittivity	1
440C Specific Heat	450 J/(kg-K)
440C Thermal Conductivity	24.2 W/(m-K)

Table 1 – Simulation Parameters, Plate

The height of the plate was exactly matched to that in the experiments (0.125") but the other dimensions were approximated. As the critical heating of the plate takes place sufficiently far

from the edges (in the middle, underneath the coil), there was no need to capture the outermost plate edges (in fact, the plate size could have been reduced even further). The one consideration was to ensure that the edges were far enough from the areas of interest to reduce the impact of the "edge effects.". These edge effects are a result of the plate being of a finite size and the eddy currents induced at the boundaries of the plate running out of room to propagate, creating recirculation regions of heat as seen on the left- and right-hand sides of Figure 19 (this is further described by Vrana et al. [13]).

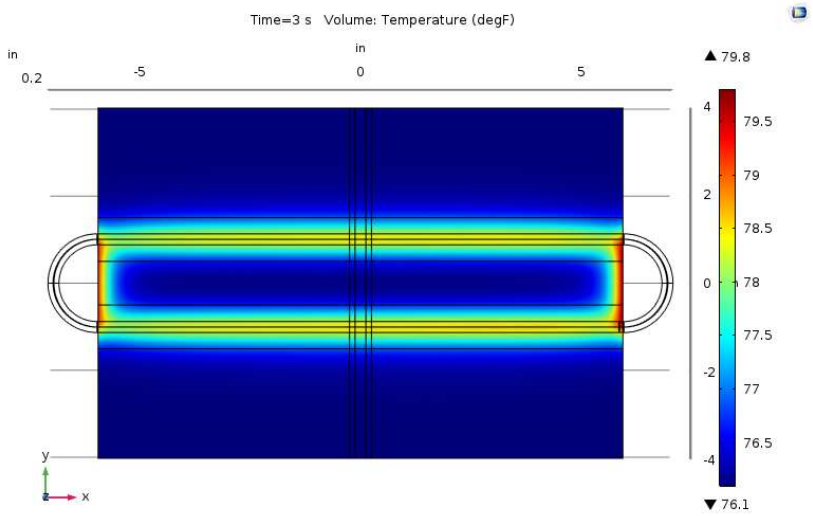

Figure 19 – Induction Heating Edge Effects

HAZ 440C Density	7700 kg/m^3
HAZ 440C Conductivity	1.396e3 S/m
HAZ 440C Relative Permeability	700
HAZ 440C Relative Permittivity	1
HAZ 440C Specific Heat	450 J/(kg-K)
HAZ 440C Thermal Conductivity	24.2 W/(m-K)

Table 2 – Simulation Parameters, HAZ

Copper Density	8960 kg/m^3
Copper Conductivity	5.998e7 S/m
Copper Relative Permeability	1
Copper Relative Permittivity	1
Copper Specific Heat	385 J/(kg-K)
Copper Thermal Conductivity	400 W/(m-K)
Coil Frequency	245 kHz
Coil Current (Baseline Trials)	36 A
Coil Current (Welded Trials)	19 A

Table 3 – Simulation Parameters, Coil

Air Density	*** kg/m^3
Air Conductivity	1 S/m
Air Relative Permeability	1
Air Relative Permittivity	1
Air Specific Heat	*** J/(kg-K)
Air Thermal Conductivity	*** W/(m-K)

Table 4 – Simulation Parameters, Air Domain

***The properties of air within COMSOL, by default, are set to vary with temperature and do not have constant values provided.

The weld was modeled as a region 0.25” wide with the HAZ regions to either side of this weld, directly adjacent to the weld, and each 0.125” wide. Within the HAZ regions, the rule of mixtures was used to alter the base conductivity from that of the 440C as described above which was compounded with an additional factor to capture the sensitization forcing the eddy currents in to taking different paths within the sample. See the Discussion section for more information on the derivation of this value.

The hairpin coil used in the 2019 experiments was wrapped in a nylon mesh. This nylon mesh was not explicitly modeled but its effect was simulated in COMSOL by using a liftoff distance of 1/16” (induction heating is not impacted by the presence of such a material in between the coil and the sample). The 1/16” liftoff distance was derived by adding the ~0.5 mm nylon mesh thickness together with the physical liftoff distance, ~0.5-1 mm, between the mesh-encased coil and the sample. Thus, from a simulation perspective, the nylon mesh only served to provide an air gap between the coil and the plate. Refer to Figure 20 for this offset.

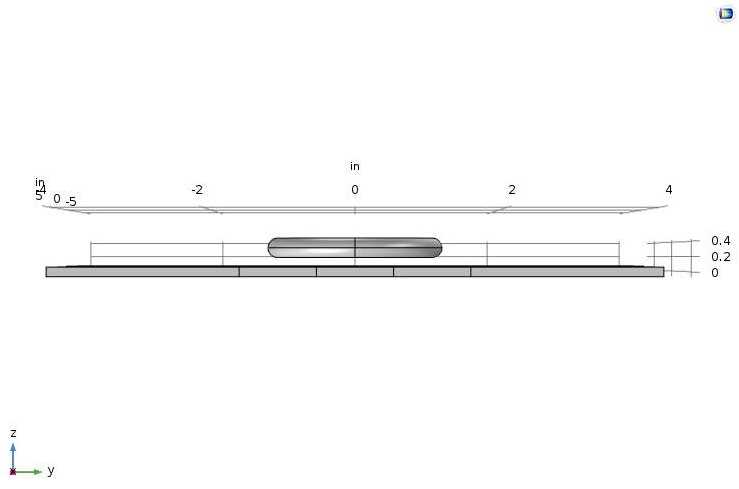

Figure 20 – COMSOL Model, Coil Offset

The lumped port feature of COMSOL was used to excite the coil. The excitation current was 36 A for the bare plate case and 19 A for the welded case (see the Discussion section for more

information on the derivation of these values). The plate and coil components were enclosed in an infinite element domain to simulate the plate's presence within in an arbitrarily large room/space filled with air.

A frequency-transient study was implemented to capture both the frequency-dependence in the solution of the electromagnetic equations with the time-dependence in the solution of the heat transfer problem. An overview of the entire model (including the surrounding air domain) can be seen in Figure 21 and Figure 22.

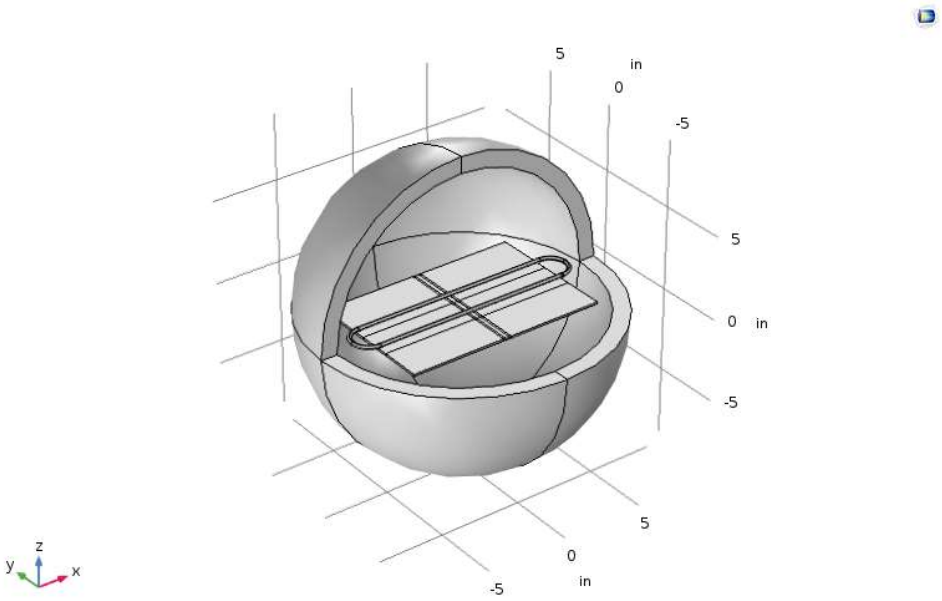

Figure 21 – COMSOL Model, Isometric View

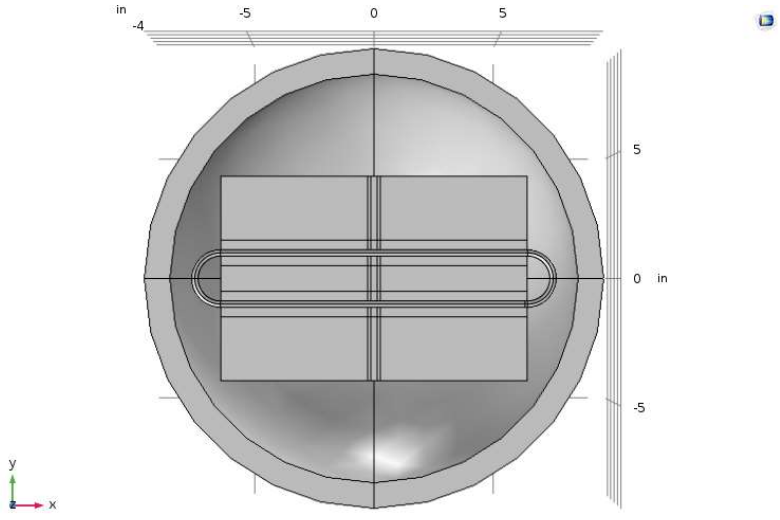

Figure 22 – COMSOL Model, Plan View

As discussed previously, the skin depth is a critical quantity to understand when dealing with induction heating problems. In the case of the 440C steel, the skin depth was found to be approximately:

$$\delta = \sqrt{\frac{\rho}{\pi f \mu_0 \mu_r}} = \sqrt{\frac{680\ x\ 10^{-9}\ \Omega\text{m}}{\pi(245\ x\ 10^3\ Hz)(4\pi\ x\ 10^{-7}\ H/m)(700)}} = 3.17x\ 10^{-5}\ m = 0.00125\ in$$

The skin depth within the copper coil was also computed:

$$\delta = \sqrt{\frac{\rho}{\pi f \mu_0 \mu_r}} = \sqrt{\frac{1.6672\ x\ 10^{-8}\ \Omega\text{m}}{\pi(245\ x\ 10^3\ Hz)(4\pi\ x\ 10^{-7}\ H/m)(1.008)}} = 1.31\ x\ 10^{-4}\ m$$
$$= 0.00515\ in$$

As the plate's skin depth was two orders of magnitude smaller than its characteristic length (its height, 0.125") and the coil's skin depth was one order of magnitude smaller than its characteristic length (the thickness of the coil's hollow copper tubing, ~0.0625"), it was decided that an impedance boundary condition (also called a Leontovich boundary condition [57]) could be applied to the outer boundaries of both (note that COMSOL deems this condition to be acceptable when the skin depth is at least 10 times smaller than the characteristic length). This type of boundary condition allows for the assumption that all the induced eddy currents are concentrated near the surface (due to the small skin depth), meaning that the electromagnetics do not have to be solved within the coil or plate to simplify the computation.

If a planar surface is taken to be located at a position z = 0, i.e. the surface in question lies entirely in the x-y plane, with the positive z-axis pointing out of the surface, the components of the electric and magnetic fields are related through [57]:

$$E_x = -\eta H_y$$

$$E_y = \eta H_x$$

Here, η is the surface impedance in units of V/A, E_x and E_y are the components of electric field in V/m, and H_x and H_y are the components of the magnetic field in A/m.

In equivalent vector form, this relationship can be represented as [57]:

$$\hat{\boldsymbol{n}}\ x\ (\hat{\boldsymbol{n}}\ x\ \boldsymbol{E}) = -\eta \hat{\boldsymbol{n}}\ x\ \boldsymbol{H}$$

Here, $\hat{\boldsymbol{n}}$ is the unit normal to the plate ($\hat{\boldsymbol{k}}$ in this case).

As seen in the derivation of the magnetic vector potential formulation of the diffusion equation, the electric field is a combination of an induced and an applied field [43]:

$$\boldsymbol{E} = \boldsymbol{E}_{induced} + \boldsymbol{E}_{applied}$$

This can be substituted in to the vector form of the impedance boundary condition:

$$\hat{\boldsymbol{n}}\, x\, \left(\hat{\boldsymbol{n}}\, x\, (\boldsymbol{E_{induced}} + \boldsymbol{E_{applied}})\right) = -\eta \hat{\boldsymbol{n}}\, x\, \boldsymbol{H}$$

Through the distributive properties of vectors, this can be rewritten as:

$$\hat{\boldsymbol{n}}\, x\, \left(\hat{\boldsymbol{n}}\, x\, \boldsymbol{E_{induced}} + \hat{\boldsymbol{n}}\, x\, \boldsymbol{E_{applied}})\right) = -\eta \hat{\boldsymbol{n}}\, x\, \boldsymbol{H}$$

$$\hat{\boldsymbol{n}}\, x\, (\hat{\boldsymbol{n}}\, x\, \boldsymbol{E_i}) + \hat{\boldsymbol{n}}\, x\, (\hat{\boldsymbol{n}}\, x\, \boldsymbol{E_s}) = -\eta \hat{\boldsymbol{n}}\, x\, \boldsymbol{H}$$

Note that the "s" subscript represents the applied or source electric field, and the "i" subscript represents the induced electric field.

From the definition of the vector triple product, this equation can be rewritten once more:

$$\boldsymbol{a}\, x\, (\boldsymbol{b}\, x\, \boldsymbol{c}) = (\boldsymbol{a} \cdot \boldsymbol{c})\boldsymbol{b} - (\boldsymbol{a} \cdot \boldsymbol{b})\boldsymbol{c}$$

$$\hat{\boldsymbol{n}}\, x\, (\hat{\boldsymbol{n}}\, x\, \boldsymbol{E_i}) + \hat{\boldsymbol{n}}\, x\, (\hat{\boldsymbol{n}}\, x\, \boldsymbol{E_s}) = -\eta \hat{\boldsymbol{n}}\, x\, \boldsymbol{H}$$

$$(\hat{\boldsymbol{n}} \cdot \boldsymbol{E_i})\hat{\boldsymbol{n}} - \boldsymbol{E_i} + (\hat{\boldsymbol{n}} \cdot \boldsymbol{E_s})\hat{\boldsymbol{n}} - \boldsymbol{E_s} = -\eta \hat{\boldsymbol{n}}\, x\, \boldsymbol{H}$$

This result is COMSOL's impedance boundary condition formulation [58]:

$$\sqrt{\frac{\mu_0 \mu_r}{\varepsilon_0 \varepsilon_r - \frac{j\sigma}{\omega}}}\, \hat{\boldsymbol{n}}\, x\, \boldsymbol{H} + \boldsymbol{E_i} - (\hat{\boldsymbol{n}} \cdot \boldsymbol{E_i})\hat{\boldsymbol{n}} = (\hat{\boldsymbol{n}} \cdot \boldsymbol{E_s})\hat{\boldsymbol{n}} - \boldsymbol{E_s}$$

Equation 19 – COMSOL Impedance Boundary Condition

Given the negligible skin depths of the 440C plate and the copper coil found previously, this boundary condition was implemented in both the coil and plate boundaries within the model as seen in Figure 23 to reduce the computational effort.

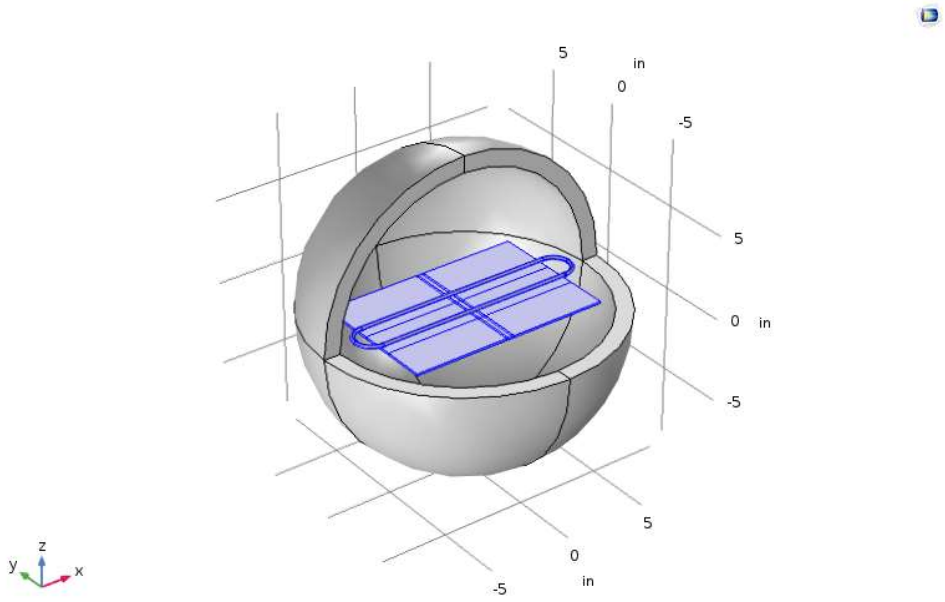

Figure 23 – Impedance Boundary Condition Model Domains (Highlighted)

The actual hairpin coil used in the experiments was made of a hollow copper tube. However, the impedance boundary condition enabled the modeling simplification of a solid piece of copper because the currents would be modeled as only flowing on the surface. Although neglecting the interior of the coil would not provide an accurate account of the heat transfer within the coil, this was not of interest and was acceptably disregarded.

A convective heat flux was introduced to all the plate boundaries to model the convective losses. However, the governing convective heat transfer coefficient (h) is not an intuitive quantity and can vary depending on plate orientation, the use of active/passive cooling, etc. The model used to establish this coefficient was the simplified formulae established by McAdams for a horizontal plate with the heated side facing up in air at atmospheric pressure and room temperature [59]. Two regimes exist, one for turbulent and one for laminar flow. These two regimes are defined by the value of the Rayleigh number.

Without explicitly finding the Rayleigh number (to avoid introducing further error), the values were found for both the laminar and turbulent regimes to gauge the difference between them and find a suitable value. A conservative change in temperature was used of 5 °F (higher than was seen in the experimentation) to find these values.

$$h_c = 0.22(\Delta T)^{1/3}$$

Equation 20 – McAdams' Convective Heat Transfer Coefficient, Turbulent

$$h_c = 0.27(\Delta T/L)^{1/4}$$

Equation 21 – McAdams' Convective Heat Transfer Coefficient, Laminar

Here, ΔT is the difference in temperature between the surface and the ambient air in °F and L is the characteristic length (the dimension of a plate side) in ft. As McAdams' equations are based off a square plate, the average side length was taken of the rectangular plate used.

Note that the units of these equations are Btu/(hr-ft^2-°F). The conversion in to SI units (W/(m^2-K)) is 1 Btu/(hr-ft^2-°F) = 5.678 (W/(m^2-K)) [60] yielding:

$$h_c = 5.678\ x\ 0.22(\Delta t)^{1/3} = 5.678\ x\ 0.22(5\ °\text{F})^{1/3} = 2.136\ \frac{W}{m^2K}$$

$$h_c = 5.678\ x\ 0.27\left(\frac{\Delta t}{L}\right)^{1/4} = 5.678\ x\ 0.27\left(\frac{5\ °\text{F}}{0.8333\ ft}\right)^{1/4} = 2.399\ \frac{W}{m^2K}$$

The small values at hand showed that the convective losses would be minimal. With the small temperature gradients seen, the laminar equation was used in the model.

Finally, COMSOL's diffuse surface feature was used to provide an emissivity to all the plate boundaries which would enable radiative heat transfer to be calculated. Like the convection term, this value has some abstraction and a final value was settled on of 0.1 (see the Discussion section for more information on this value).

4 Results

4.1 2018 Experimental Results

As described above, the goal of the 2018 experimental tests was to draw a correlation between intensity counts and temperature such that any future heating of plates could immediately have their observed heat signatures resolved to an increase in temperature.

The initial set of experiments consisted of ten (10) trials run in two sets of five. In between the two sets of tests, the entire test setup was broken down before being set back up to ensure that the process and data were repeatable. Following the process laid out previously, the result was a comparison between the predicted temperature based on the observed change in intensity counts and the new measured temperature to verify consistency. Additionally, a "cool down" period of approximately 30-45 minutes was used between each test to enable the plate to equilibrate back with the ambient air temperature.

A summary of the experimental data taken in 2018 can be found in Table 5 (the complete data set can be seen in Appendix B).

Trial	Predicted Temperature	Measured Temperature	Relative Error
1	77.1 °F	76.9 °F	0.26%
2	78.7 °F	78.6 °F	0.13%
3	78.0 °F	78.2 °F	0.26%
4	78.7 °F	78.6 °F	0.13%
5	79.3 °F	79.1 °F	0.25%

Trial	Predicted Temperature	Measured Temperature	Relative Error
Test setup broken down and set up again			
6	79.2 °F	78.9 °F	0.88%
7	79.6 °F	79.1 °F	0.63%
8	80.5 °F	80.2 °F	0.37%
9	80.6 °F	80.6 °F	0.00%
10	81.6 °F	80.9 °F	0.86%

Table 5 – 2018 Experimental Data Summary

While there are several potential sources of error, including the IR thermometer's test area and temperature range (see the Discussion section for more details), the above results proved the validity of using the Stefan-Boltzmann law for a correlation between intensity counts and temperature rise, with a maximum error of less than 1% seen across the ten trials.

4.2 2019 Experimental Results

The data taken in 2019 used the 2018 results as a basis for more sophisticated analysis of the temperature variations seen in two different scenarios. That is, after showing the suitability of using the Stefan-Boltzmann law, it was leveraged to draw conclusions about the temperature increases seen in the 2019 dataset to assist in the creation of the COMSOL model.

Per the modifications in the testing described above, the 2019 trials varied both heating time and materials tested. The first set of experiments of interest were those of the unwelded, unsensitized 440C samples to provide a baseline for the model parameters. Two trials were run with slightly different parameters to the 2018 trials as described in Table 6.

Trial	Heating Time (s)	Total Capture Time (s)	Measured Initial Temperature	Measured Maximum Temperature	Measured Final Temperature
1	3	10	76.1 °F	77.9 °F	77.7 °F
2	3	10	76.2 °F	77.9 °F	77.7 °F

Table 6 – 2019 Experimental Data Summary, Unsensitized 440C

Although the Stefan-Boltzmann law was shown to be effective in the 2018 trials, a check was performed on the second trial of this unwelded 2019 data to verify that it was appropriate to use. To do this, the following procedure was followed:

1. Based on Trial 1 of the 2018 experiments which had a comparable initial temperature (76.1 °F), 5950 intensity counts were added to the intensity counts found at the final timestep and at the point of maximum heating to account for the background radiation of the plate.
2. The relative fractional difference in intensity counts between the final timestep and point of maximum heating was found:

$$Difference = \frac{|Heated\ Intensity\ Counts - Final\ Intensity\ Counts|}{Heated\ Intensity\ Counts}$$

3. This difference was then added to 1 to create a multiplier, i.e. a fractional difference of 0.05 was transformed to a value of 1.05.
4. This multiplier was raised to the ¼ power, in line with the Stefan-Boltzmann law, to create a new multiplier to be used for computing the temperature.
5. The final temperature was multiplied by this factor to estimate what the temperature should be based on the change seen in intensity counts.
6. The predicted temperature value was compared with the measured value as seen in Table 7.

It should be noted that as several temperatures were obtained around the plate to capture heating at different locations, the computed value at each location was averaged before being tabulated.

Trial	Predicted Maximum Temperature	Measured Maximum Temperature	Relative Error
1	N/A	N/A	N/A
2	77.8 °F	77.9 °F	0.15%

Table 7 – 2019 Data Validation

Thus, the Stefan-Boltzmann law was shown to hold once more with this data.

A similar set of data was collected for the welded plates. One key difference as described above was the lack of a measured maximum temperature value. Using the Stefan-Boltzmann law, the maximum temperature was predicted and tabulated in Table 8 (the raw data can be seen in Appendix C). Once again, due to multiple temperature measurements taken around the HAZ regions, the predicted temperature rise for all points were averaged before being tabulated.

A second difference between the 2018 and 2019 trials was that, as the initial measured temperature showed more variation than that of the baseline (unwelded) plates, a variable amount of intensity counts was added to the final and maximum intensity count values before computing the maximum temperature. This was done through a calculation based on the counts seen in the 2018 trials in Appendix B.

Trial	Measured Initial Temperature	Baseline Intensity Counts Added
1	75.2 °F	5670
2	75.9 °F	5860
3	75.3 °F	5670
4	75.7 °F	5830
5	76.2 °F	5950

Table 8 – Intensity Counts Added, Welded 440C

Trial	Heating Time (s)	Total Capture Time (s)	Measured Initial Temperature	Predicted Maximum Temperature	Measured Final Temperature
1	3	10	75.2 °F	76.4 °F	76.2 °F
2	3	10	75.9 °F	77.2 °F	76.8 °F
3	2	5	75.3 °F	76.3 °F	75.8 °F
4	2	5	75.7 °F	76.5 °F	76.2 °F
5	2	5	76.2 °F	76.9 °F	76.7 °F

Table 9 – 2019 Experimental Data Summary, Welded 440C

4.3 Simulation Results

4.3.1 Baseline

After setting up the model as described above, a series of trials were run to confirm the baseline results obtained from testing the unsensitized plates could be obtained numerically. This entailed making the entire plate's parameters equal to those laid out in Table 1 to match the parent 440C and drawing a comparison with the experimental values in Table 6.

A simulation was run for each of the two (2) baseline experiments to ensure consistent results by using the selected input parameters. The results for each trial are shown in Figure 24 through Figure 27. Two images are shown, one being the raw COMSOL temperature map as seen looking down on the top of the plate at the time of maximum heating and the other showing trackline results at three time snapshots. Time t = 0 s shows the baseline temperature and the other two lines depict results at the maximum temperature and the temperature at the end of the trial. All results correspond to a 2" trackline (labeled as arc length).

Although several combinations of current and relative magnetic permeability were shown to duplicate the experimental results, the literature showed the relative magnetic permeability trending towards 600-700 for 440C steel [5, 8, 59] and thus a combination was found where the current was of a value to allow for a higher relative magnetic permeability to be used. By solving the inverse problem in this way, it allowed for the proper parameters to be established even with knowledge limitations in the physical parameters present (see the Discussion section for more information on this methodology).

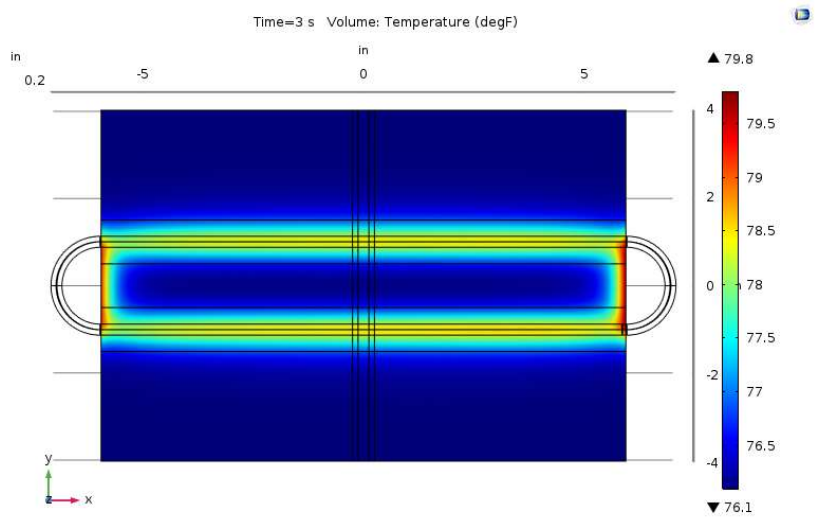

Figure 24 – Baseline Trial 1, Temperature Profile

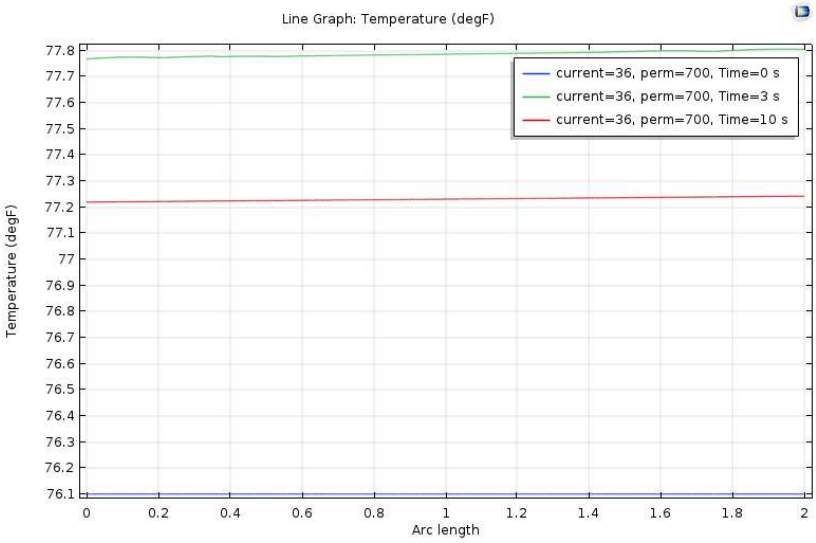

Figure 25 – Baseline Trial 1, Temperature Profile

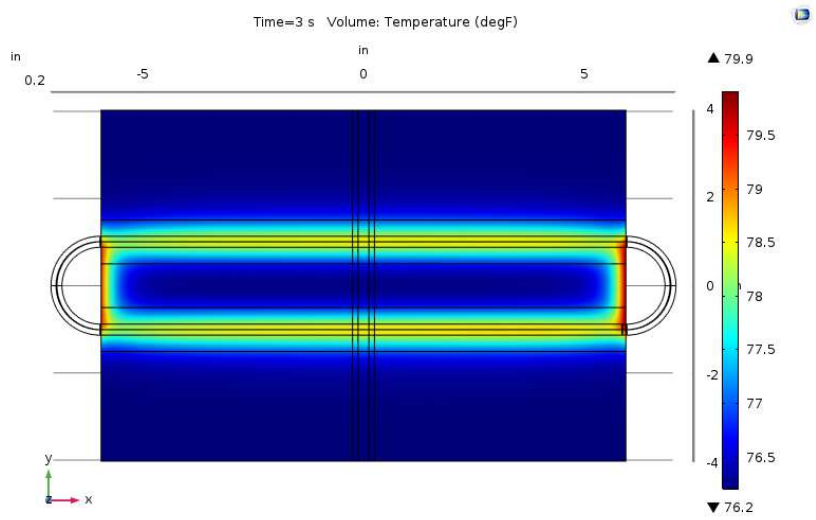

Figure 26 – Baseline Trial 2, Plan View Temperature

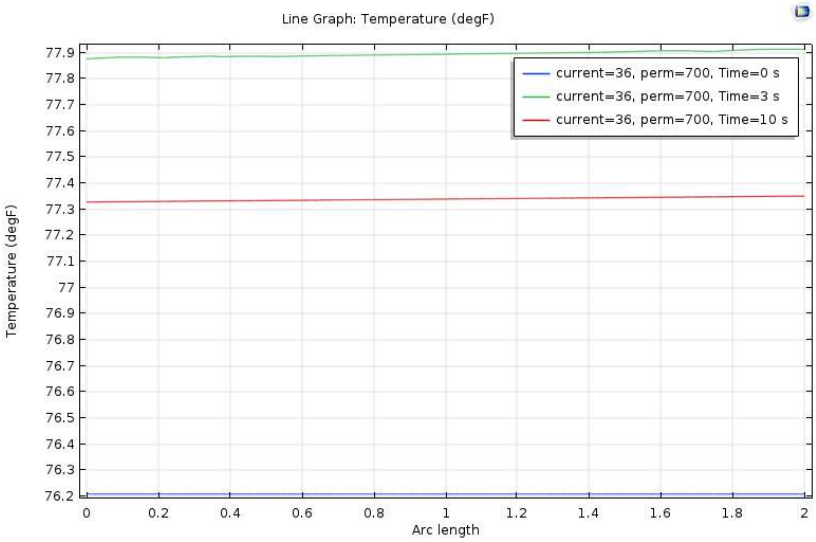

Figure 27 – Baseline Trial 2, Temperature Profile

The 2” trackline shown in the graphs was located 0.125” away from the projected outer edge of the coil onto the plate and ran parallel to the coil, centered on the weld. Due to slight numerical variations in temperature along the length of the trackline, the averaged value across the trackline was found for each time. Additionally, this line had to be placed 0.0001” below the surface of the plate for numerical stability. This data is tabulated in Table 10.

Two modifications were made to the simulations trial-over trial:

1. The initial temperature was loaded based on the experimental values.
2. The convective heat transfer coefficient was recalculated based on the experimental temperature rise seen.

Trial	Heating Time (s)	Total Capture Time (s)	Initial Temperature	Maximum Temperature	Final Temperature
1	3	10	76.1 °F	77.8 °F	77.2 °F
2	3	10	76.2 °F	77.9 °F	77.3 °F

Table 10 – Baseline COMSOL Results

The errors when compared to the experiments are summarized in Table 11, demonstrating the ability of these initial parameters to effectively replicate the laboratory results and providing a foundation for the modification of the HAZ regions.

Trial	Initial Temperature Relative Error	Maximum Temperature Relative Error	Final Temperature Relative Error
1	N/A	0.15%	0.60%
2	N/A	0.007%	0.46%

Table 11 – Relative Error of Baseline Results

4.3.2 Modified HAZ

From a cursory look at the data, it was evident that the temperature rises seen in the welded cases were qualitatively different than those seen in the baseline trials. For instance, the first welded trial's final temperature showed a difference of 1 °F when compared to the initial temperature whereas the first baseline trial showed a 1.6 °F difference under the same heating conditions (heating time and total capture time). As Tucker et al. showed that sensitization would create temperature spikes in the HAZ, it meant that the power (current) provided by the coil and seen by the plate in the welded trials was less than that in the baseline experiments. Thus, this current value had to be adjusted between the different simulation configurations (see the Discussion section for more information).

One simulation was run for each of the welded trials to ensure that the selected parameters gave consistent results. Like the baseline trials, two images are presented: (1) the temperature map as seen in plan view at the time of maximum heating and (2) a plot with three curves representing the baseline temperature, the maximum temperature, and the final temperature over the 2" trackline. Also like the baseline trials, the initial temperature and convective heat transfer coefficient were modified for each run. Below are results for welded Trials 1-5. Note that welded Trials 1 and 2 involved an induction coil application time of 3 s, whereas welded Trials 3-5 involved an application time of 2 s.

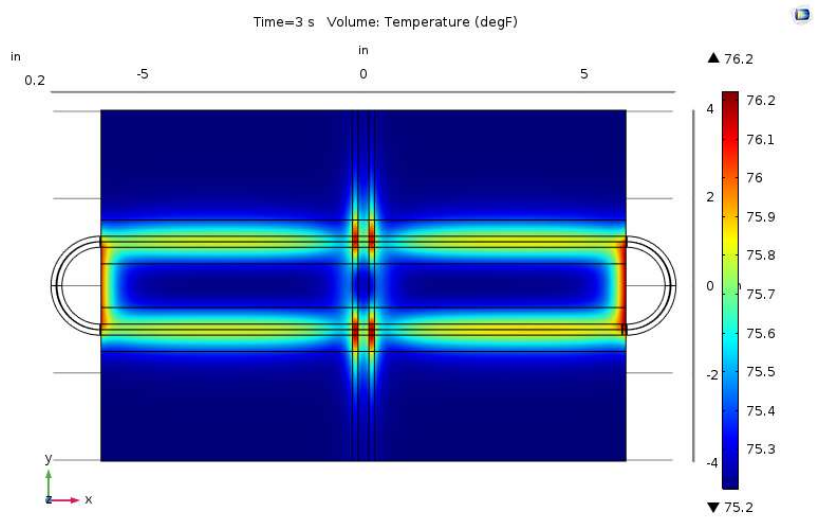

Figure 28 – Welded Trial 1, Plan View Temperature

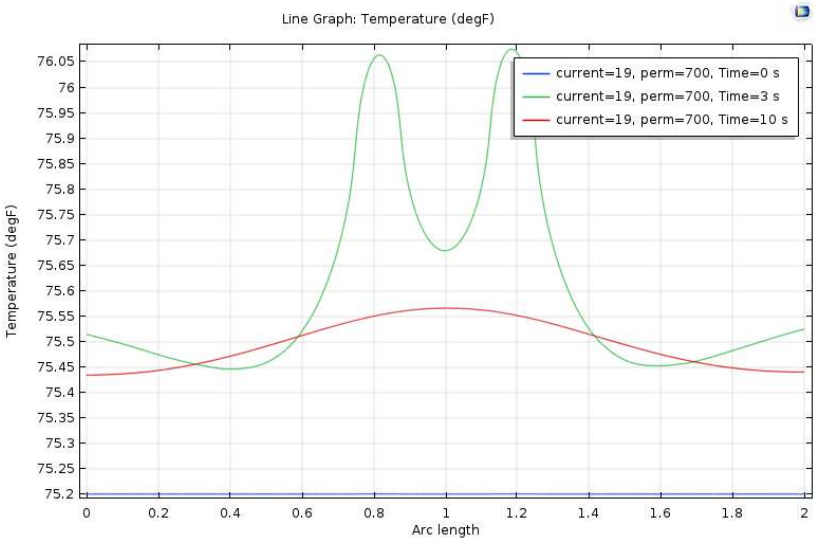

Figure 29 – Welded Trial 1, Temperature Profile

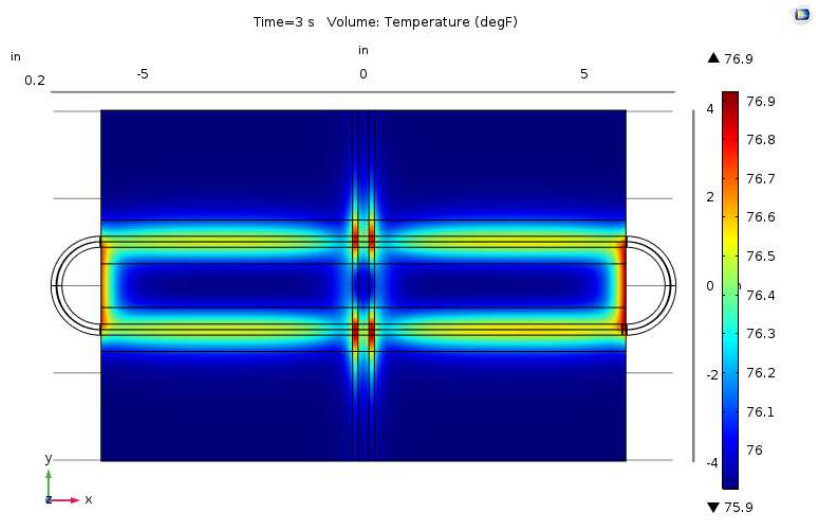

Figure 30 – Welded Trial 2, Plan View Temperature

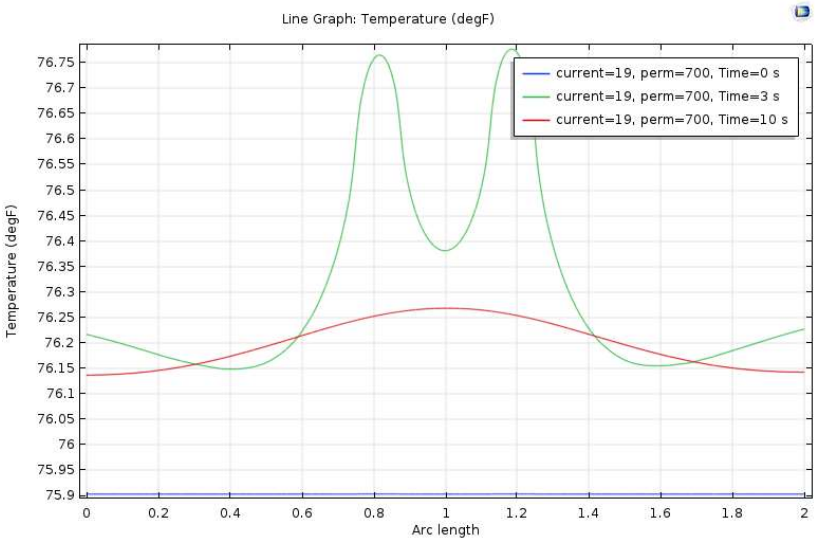

Figure 31 – Welded Trial 2, Temperature Profile

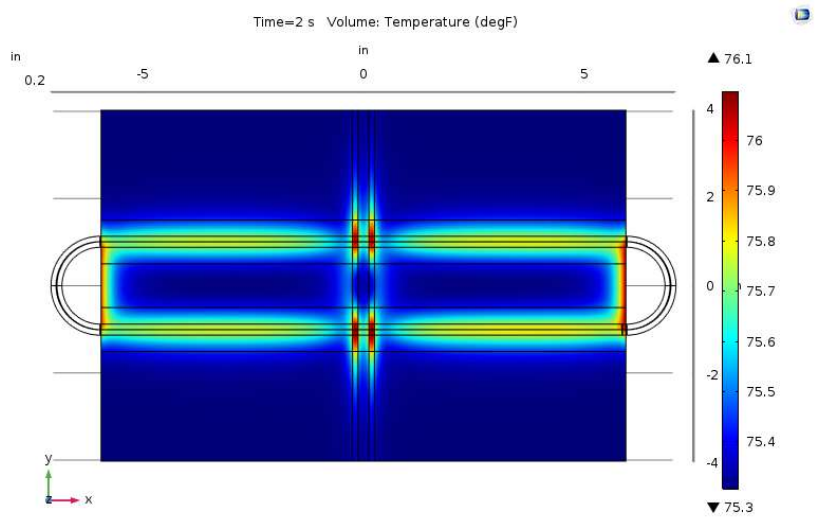

Figure 32 – Welded Trial 3, Plan View Temperature

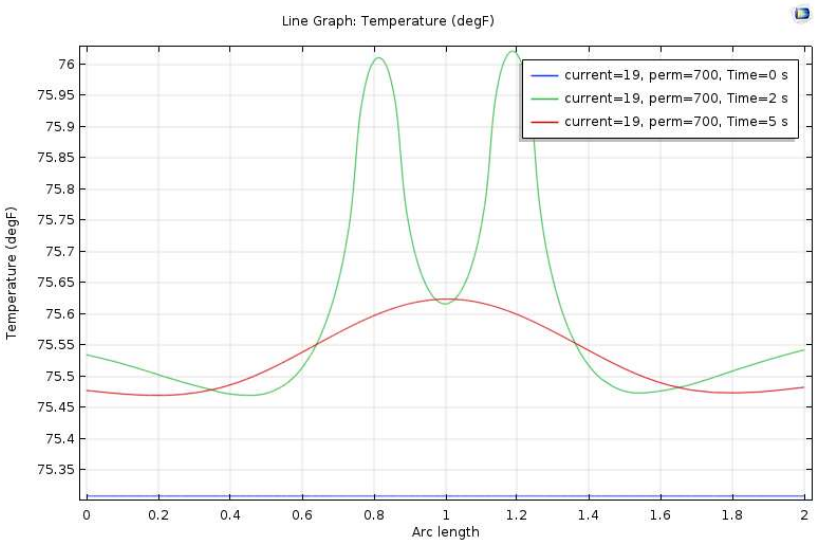

Figure 33 – Welded Trial 3, Temperature Profile

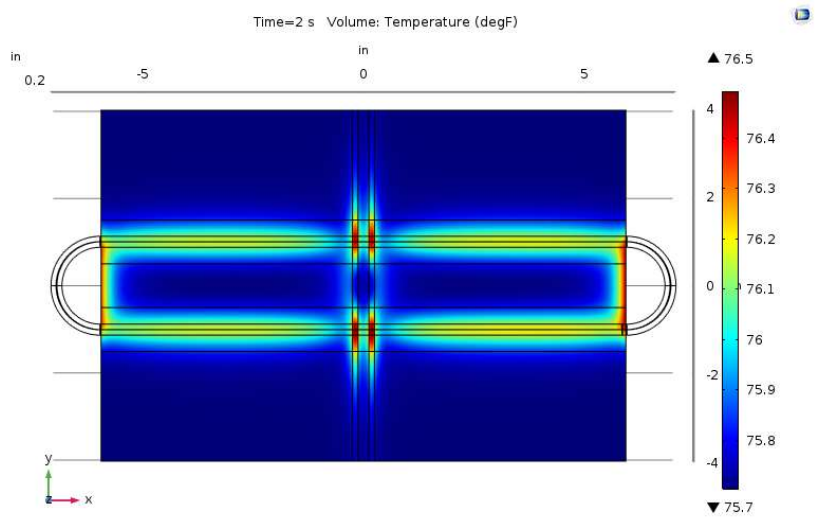

Figure 34 – Welded Trial 4, Plan View Temperature

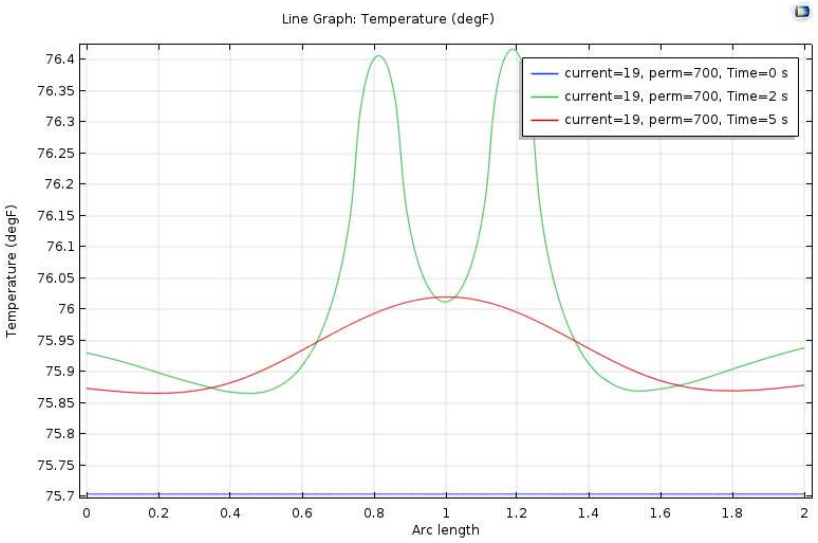

Figure 35 – Welded Trial 4, Temperature Profile

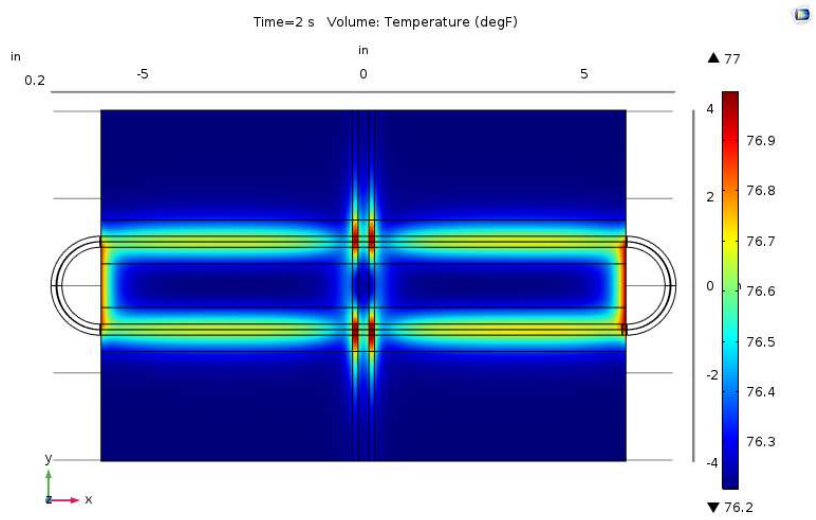

Figure 36 – Welded Trial 5, Plan View Temperature

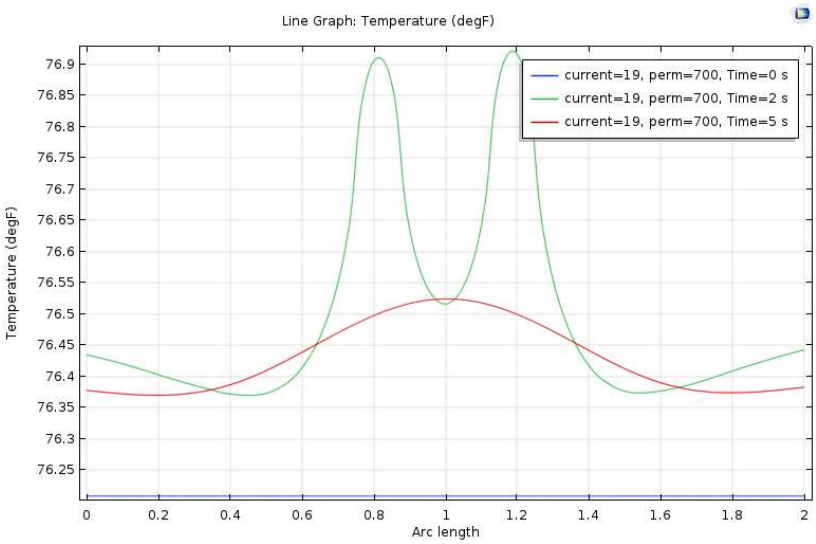

Figure 37 – Welded Trial 5, Temperature Profile

Trial	Heating Time (s)	Total Capture Time (s)	Initial Temperature	Maximum Temperature	Final Temperature
1	3	10	75.2 °F	76.1 °F	75.6 °F
2	3	10	75.9 °F	76.8 °F	76.3 °F
3	2	5	75.3 °F	76.0 °F	75.6 °F
4	2	5	75.7 °F	76.4 °F	76.0 °F
5	2	5	76.2 °F	76.9 °F	76.5 °F

Table 12 – Welded COMSOL Data

As the data had more variability than the baseline trials, the maximum temperature was taken to be the highest temperature within the HAZ at the end of the heating period. For the final temperature, the maximum temperature at the end of the capture time was taken as the heating had "blurred." These assumptions were justified as the IR thermometer uses a circular region to capture a temperature based on the distance it is held away from the sample, meaning that it will tend to find the maximum within that region (see the Discussion section for more details).

Trial	Initial Temperature Relative Error	Maximum Temperature Relative Error	Final Temperature Relative Error
1	N/A	0.41%	0.83%
2	N/A	0.52%	0.69%
3	N/A	0.33%	0.23%
4	N/A	0.05%	0.24%
5	N/A	0.03%	0.23%

Table 13 – Relative Error of Welded Results

Once more, the error values of less than 1% showed the tight agreement between the experiments and the COMSOL model.

4.3.3 Trackline Comparison

To provide the final comparison between the experimental results and the numerical simulations, the tracklines of the welded trials were compared. This involved taking the 2" tracklines from COMSOL as shown in the figures above and plotting them against the experimental tracklines as shown in Appendix C.

To do this, the first step was to leverage the Stefan-Boltzmann law as laid out above to convert the intensity counts along the experimental tracklines in to temperature values. Once this was done, the pixel locations of the tracklines were converted in to a linear measurement as at the camera height used, it was known that approximately 93 pixels corresponded to 1 inch. Next, an adjustment was made to this positioning data to ensure that it would align properly with the COMSOL results by setting the "0" point of the data at the minimum temperature value in between the two HAZ regions. This was done to mimic the COMSOL trackline where it had a known "0" point in the center of the weld (which corresponded to the minimum temperature between the HAZ regions) and allowed for the two data sets to be easily superimposed.

One final adjustment was made regarding the time at which the COMSOL data was taken. On the coil itself, there was a button to begin the data capture in the software and there was a trigger to begin heating. There ended up being a small time lag between when this capture began and when heating commenced as seen in the raw data where the intensity counts did not begin to change until a short while in to the capture period. This transient period was subtracted from the nominal time of the trackline capture which was then used as the capture time in the model to ensure that an accurate comparison of the heating could be performed. Table 14 shows these timing corrections. The Nominal Time of Capture represents when the trackline was captured based on the raw data and the Corrected Time of Capture represents the time that was put in to

COMSOL after subtracting out the time lag. Trial 1, with its longer capture time, was deemed to be more accurate than the remaining trials and did not have a time correction performed.

The final trackline comparisons can be seen in Figure 38 through Figure 42.

Trial	Nominal Time of Capture	Corrected Time of Capture
1	1.905 s	1.905 s
2	0.611 s	0.098 s
3	0.585 s	0.121 s
4	0.488 s	0.122 s
5	0.464 s	0.098 s

Table 14 – COMSOL Capture Time Corrections

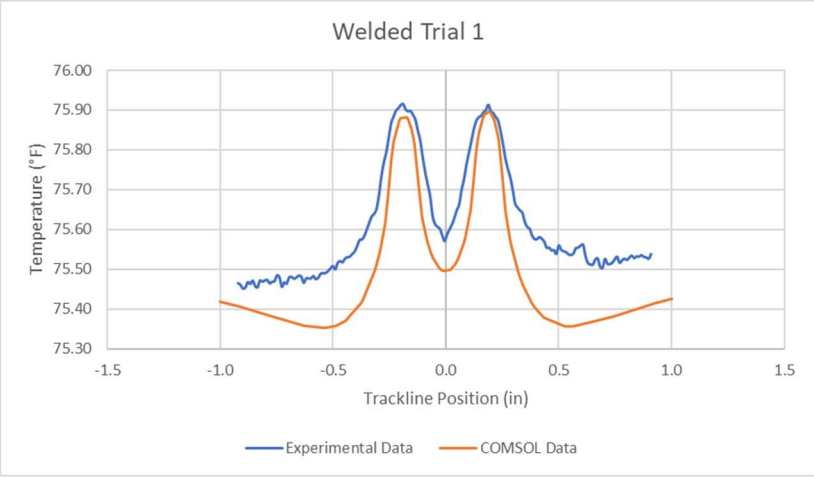

Figure 38 – Welded Trial 1, Trackline Comparison

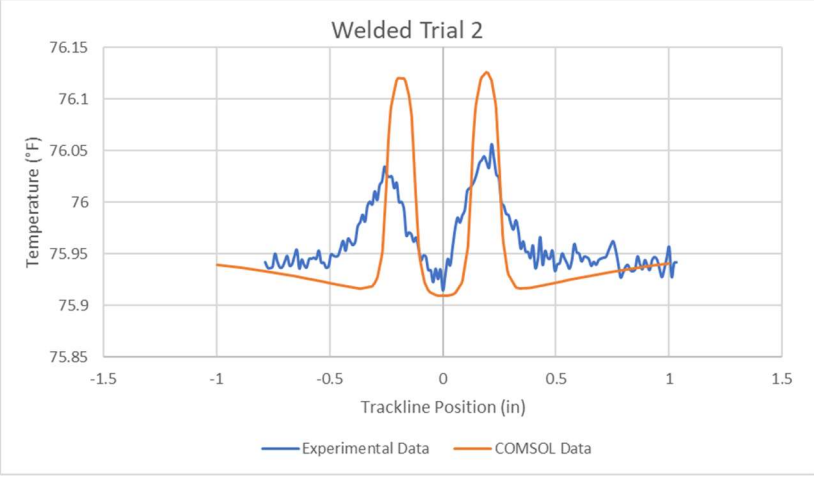

Figure 39 – Welded Trial 2, Trackline Comparison

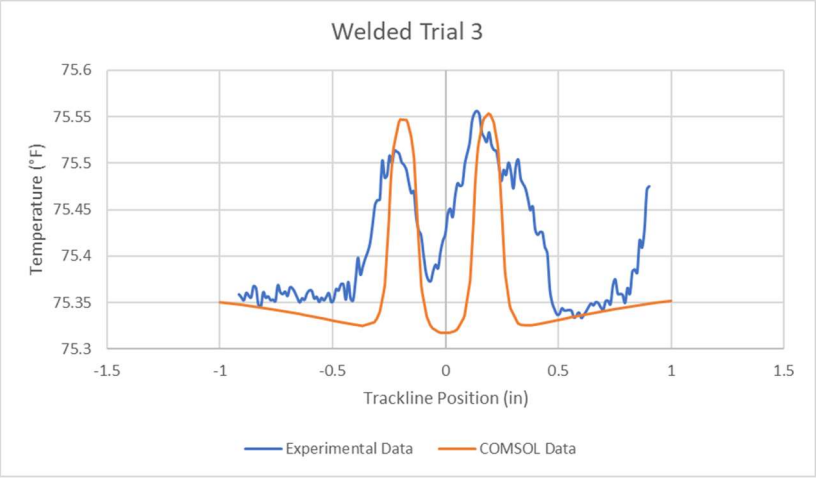

Figure 40 – Welded Trial 3, Trackline Comparison

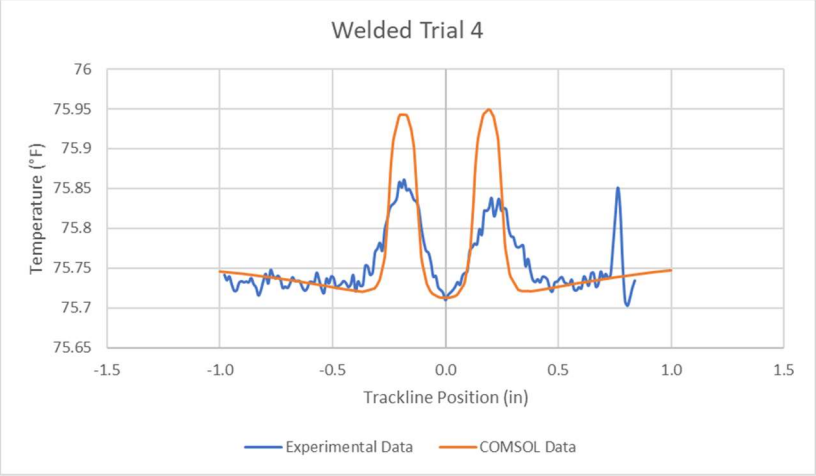

Figure 41 – Welded Trial 4, Trackline Comparison

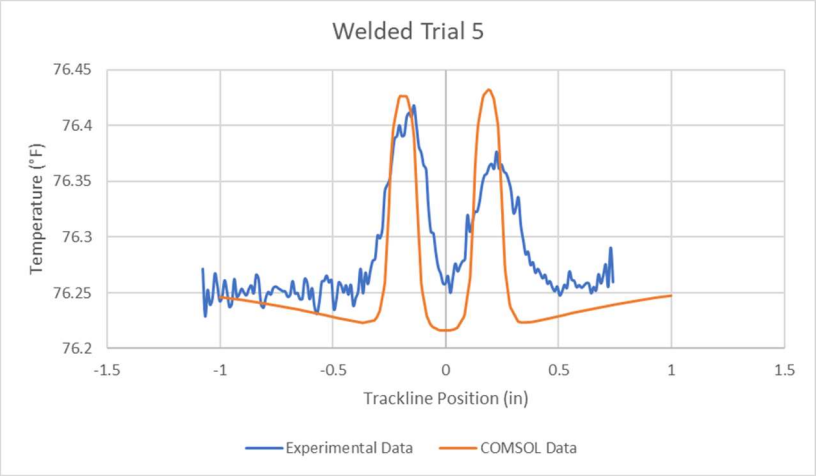

Figure 42 – Welded Trial 5, Trackline Comparison

Trial	Predicted HAZ 1 Temp.*	COMSOL HAZ 1 Temp.*	Relative Error	Predicted HAZ 2 Temp.**	COMSOL HAZ 2 Temp.**	Relative Error
1	75.92 °F	75.88 °F	0.04%	75.91 °F	75.90 °F	0.02%
2	76.03 °F	76.12 °F	0.11%	76.06 °F	76.12 °F	0.08%
3	75.51 °F	75.55 °F	0.05%	75.56 °F	75.55 °F	0.004%
4	75.86 °F	75.94 °F	0.11%	75.84 °F	75.95 °F	0.15%
5	76.42 °F	76.43 °F	0.01%	76.38 °F	76.43 °F	0.07%

*HAZ region located on the left-hand side of the preceding graphs
**HAZ region located on the right-hand side of the preceding graphs

Table 15 – HAZ Temperature Errors

Table 15 provides the summary of the temperature errors between the experiments and the numerical simulations within the HAZ regions which once more demonstrated the accuracy of the model.

5 Discussion

A few initial observations can be made when comparing the COMSOL results with the experiments:

1. The trackline comparisons, while showing a close agreement, each showed a slight variation for differing reasons.
2. The cooling behavior is more rapid than anticipated, yielding a lower temperature at the end of the capture time than expected.

Regarding the trackline comparisons, each showed slightly different errors which could be attributed to the following reasons:

Trial 1 – This trial is one of the closest matches between the experiments and the numerical model. A possible reason for this is due to the longer heating time used which helped to eliminate some of the uncertainty in the transient behavior earlier in the heating period.

Trial 2 – While the alignment of the HAZ and the positioning of the maximum temperature in the HAZ regions is quite good, the magnitudes of the maximum temperatures are slightly off. There are many possible reasons for this including slight microstructure variations in the HAZ regions or a slight variation in the current that the plate saw, different from the predicted 19 A.

Trial 3 – In this case, the magnitude of the maximum temperature in the HAZ is in good agreement between the two cases but the HAZ shows up as a slightly wider region than predicted numerically. A possible cause of this is the trackline being moved to a different location between trials which, due to the inherent variability in the HAZ sizing, could capture regions that are slightly wider than those previously approximated.

Trial 4 – Similar to Trial 2, the alignment of the HAZ and the positioning of the maximum temperature in the HAZ regions between the experiment and the COMSOL simulation are in

good agreement but again, the temperature magnitudes are slightly off. This could be due to slight microstructure variations in the HAZ regions or a slight variation in the current that the plate saw, different from the predicted 19 A.

Trial 5 – This is one of the more accurate trials in terms of the positioning of the HAZ and the magnitude of the maximum temperatures although the maximum temperatures in the second HAZ region (on the right-hand side) show more variation than on the left. This could be due to the inherent variability of the amount of sensitization within each HAZ which yields different heating behaviors on each side of the weld. Additionally, the weld is not flush with the rest of the plate which forced the coil to not lie perfectly flat on the plate's surface. This could have resulted in dissimilar heating between the two HAZ regions. See the Discussion section for more on this behavior.

Regarding the cooling, more analysis would be needed to ascertain why this is happening. The final temperatures in the numerical results did show a strong agreement with those in the experiments but many variables impact the heat transfer and could bring the results closer upon further investigation.

Overall, with an error of less than 1% and the number of variables that can impact the results (see below), the accuracy of the model for duplicating the experimental results can be considered high.

5.1 Model Parameter Selection

As can be seen in the Results section, a suitable numerical model was established that could mimic the heating patterns seen in the experiments. However, several parameters in the numerical model were particularly challenging to find based on their variability and thus a methodical approach was taken to narrow them down:

1. Current
2. Relative Magnetic Permeability
3. Electrical Conductivity (HAZ)
4. Emissivity
5. HAZ Location

Liftoff distance and frequency were also explored, but they were felt to be known accurately enough that they could be held as constants. In the case of the liftoff distance, the measurement taken in the lab provided enough certainly to use a value of 1/16" in the model. The frequency was similar, in that the coil's power supply readout displayed the instantaneous frequency during heating. This frequency was consistently observed to be near 245 kHz and thus this value was held constant in the numerical trials.

To arrive at the final values for parameters 1-4 above, a series of parameter sweeps were performed to solve the inverse problem. That is, knowing the experimental results, the appropriate values were found to put into the model, which could then be justified/analyzed using the physics present:

1. 121 heating trials were run in COMSOL using the permutations of 11 different currents (30 A through 40 A in steps of 1 A) and 11 different relative magnetic permeabilities (100 through 700 in steps of 60).
2. These trials were all run on a plate with no sensitization present, that is, all regions possessed the same properties of the plain 440C steel.
3. Comparing these results with the experimental temperature increases during the heating of the unsensitized 440C samples, a suitable combination of current and relative magnetic permeability was established that could mimic this temperature increase.
4. With the apparent difference in heating behavior between the baseline and welded trials, a new current was found to be used in the welded trials in conjunction with the original permeability value as this should not change.
5. The conductivity within the HAZ was then adjusted to replicate the peaks seen in the experiments utilizing the current and relative magnetic permeability values found previously.
6. The emissivity was then explored.
7. Comparing the trackline results between the experiments and the numerical simulations, the HAZ sizing was adjusted from the initial assumptions.

5.1.1 Current

The current within the coil was known to fluctuate per the manufacturer based on the coupling detected between the coil and the plate. Although a range of current values was provided of 100-200 A, despite repeated attempts, the modeled temperatures were consistently much higher than those seen in the experiments even when using the low end of this range (100 A).

A factor that could have impacted this result was that after welding the plates, the two halves took on a “pitched” effect where the middle of the plate was slightly higher than the edges. This meant that when the coil was laid across this region, it did not lie perfectly flat. This variability in liftoff distance along the coil and could have disrupted the coupling between the coil and plate, driving the current lower than expected. Similarly, due to imperfections in the surfaces of the baseline, unwelded samples, this disruption could also have occurred, but likely to a lesser extent.

The final value for the baseline trials after running the 121 permutations came out to be 36 A which is what was quoted in the Design and Methodology section.

For the welded trials, a different approach had to be taken as it was evident that the amount of heating was different than in the baseline. Trackline profiles were snapped in the lab such as seen in Figure 43, in this case, capturing the heating across the parent plate, HAZ regions, and weld after approximately 2 s.

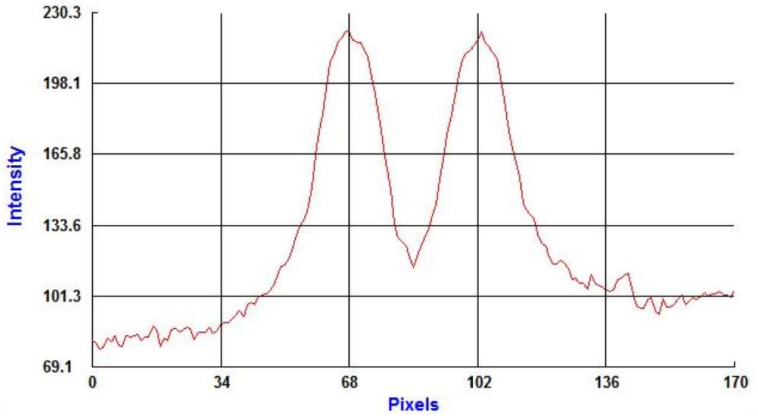

Figure 43 – Example 2019 Data Trackline

At the outer edges of this graph, flatter regions can be seen that have nonzero intensity counts. This represents regions of unsensitized material that had been heated, like what occurred in the baseline trials. Using the intensity count value at each of these extremes, the Stefan-Boltzmann law was used to find the temperature rise at these locations and a corresponding current value was found in COMSOL of 19 A. This is what was then applied for subsequent simulations of welded plates.

5.1.2 Relative Magnetic Permeability

A factor in the calculation of skin depth, the relative magnetic permeability of 440C was known to vary between ~100 and 700 [55, 61] which should have a significant impact on the heating results. It was hypothesized that regardless of the relative magnetic permeability value that came out of the 121 trials, it would not vary between the baseline and welded trials (as the same base material was used) and it would also not vary within the HAZ regions. Oswald-Tranta et al. described the fact that areas with higher magnetic permeability would heat slower and thus show up as dips in the temperature profile [22]. In each trial, as the HAZ showed a continuous increase in temperature even with varied heating times, it was not believed that this quantity changed (or changed appreciably) between the parent plate and the HAZ.

An additional consideration was the skin depth. As the impedance boundary condition was previously implemented, the skin depth had to be small enough to maintain this assumption. In the extreme case where μ was 100 (where the skin depth would be the largest), the skin depth came out to be:

$$\delta = \sqrt{\frac{\rho}{\pi f \mu_0 \mu_r}} = \sqrt{\frac{680\ x\ 10^{-9}\ \Omega\text{m}}{\pi(245\ x\ 10^{3}\ Hz)(4\pi\ x\ 10^{-7}\ H/m)(100)}} = 8.38\ x\ 10^{-5}\ m = 0.00330\ in$$

Therefore, the relative magnetic permeability value that was found for the parent plate after the set of 121 trials (700) was maintained for all test cases and for all regions while maintaining the necessary conditions for impedance boundary condition to be valid (the characteristic length being more than 10 times the skin depth).

5.1.3 Electrical Conductivity (HAZ)

As stated earlier, the rule of mixtures provided one contribution to the change in conductivity in the sensitized regions, but it was not the complete picture. Due to the presence of sensitized material at the grain boundaries, the eddy currents would be forced to take longer paths through the material rather than being able to pass freely as they would in unsensitized material.

The Drude model was used as a possible means to justify the additional difference in the conductivity. This model provides a physical basis for electrical conductivity as seen (for a DC field) in Equation 22 [62].

$$\sigma_0 = \frac{ne^2\tau}{m}$$

Equation 22 – Drude Model for Conductivity, DC Field

Here, n is the number of free electrons per unit volume in m^{-3}, e is the electron charge in C, τ is the mean time between collisions in seconds, and m is the electron mass in kg.

In the presence of an AC field, the equation becomes [63]:

$$\sigma(\omega) = \frac{\sigma_0}{1 - i\omega\tau} = \frac{\sigma_0}{1 + \omega^2\tau^2} - i\omega\tau\frac{\sigma_0}{1 + \omega^2\tau^2}$$

Equation 23 – Drude Model for Conductivity, AC Field

Here, ω is the angular frequency in rad/s.

Using this fact, the continuum form of Ohm's law can be written as seen in Equation 24 [64].

$$\boldsymbol{J} = \sigma\boldsymbol{E}$$

$$\boldsymbol{J}(t) = \Re\left(\sigma(\omega)\boldsymbol{E}(\omega)e^{-i\omega t}\right)$$

Equation 24 – Continuum Form of Ohm's Law, AC Field

While currents can pass through the sensitized grain boundaries, the preference would be to find the paths through the material that most closely resembled the unsensitized material (one with a higher conductivity). Thus, it is hypothesized that there will be an increase in the time between collisions as more randomness is created through the introduction of the chromium carbide in the microstructure, resulting in a decrease in the conductivity and an increase in the resistivity.

Technical difficulties at NUWCDIVNPT prevented new 440C SEM images from being captured in time to be analyzed. However, it was assumed that the sensitization present was comparable to that of the 301 steel shown earlier. Figure 44 shows the COMSOL simulation (based off welded Trial 1) where the conductivity in the HAZ was only adjusted through the rule of mixtures using an f value of 1.0 with the green line showing the temperature after 2 seconds. It is evident that the small peaks seen around arc lengths 0.9 and 1.3 are far lower than those seen experimentally.

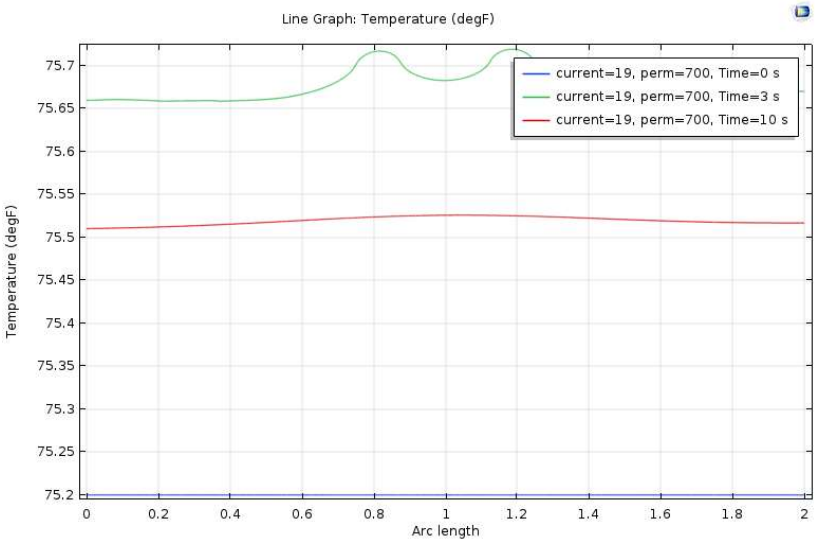

Figure 44 – HAZ with Rule of Mixtures Only

To account for the additional contribution to the measured heat signature due to the eddy current diversion, the conductivity (or the mean time between collisions) was incrementally decreased until the peak and final temperatures in the model agreed with the experimental values. This factor came out to be 1000 (a 1000X decrease in the conductivity), meaning that, due to the inverse proportionality between the mean time between collisions and the conductivity, the collision time could be assumed to have dropped by a factor of 1000 as well.

As a point of comparison, Figure 45 shows the HAZ with both the rule of mixtures and the conductivity reduction with clear spikes in line with the experimental results (these results also used the basis of welded Trial 1 but with both contributions present).

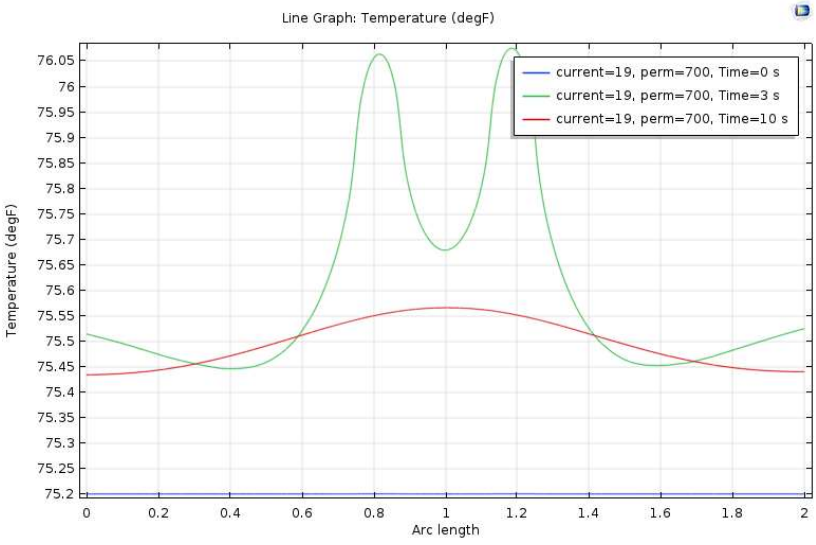

Figure 45 – HAZ with Rule of Mixtures and Drude Model

5.1.4 Emissivity

Emissivity is a difficult quantity to measure experimentally although it is bounded between 0 and 1. “Shinier” materials such as the un-treated 440C plate of interest here trend closer to 0 whereas darker, matte materials trend towards 1. It was assumed that the high reflectivity of the 440C would not allow the value to go above 0.5 (for reference, a value of 0.5 corresponds to a material such as oxidized brass which is far duller [65]).

As a check, two trials were run using the baseline COMSOL model Trial 1 parameters, one with an emissivity of 0.1 and one with an emissivity of 0.5. At the end of the 10 second capture period, the results were found as shown in Figure 46 and Figure 47.

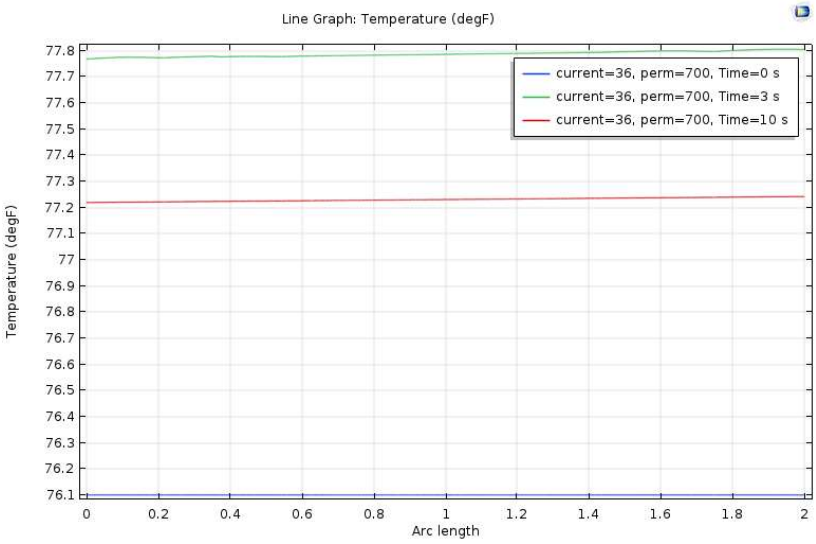

Figure 46 – Temperature Profiles with an Emissivity of 0.1

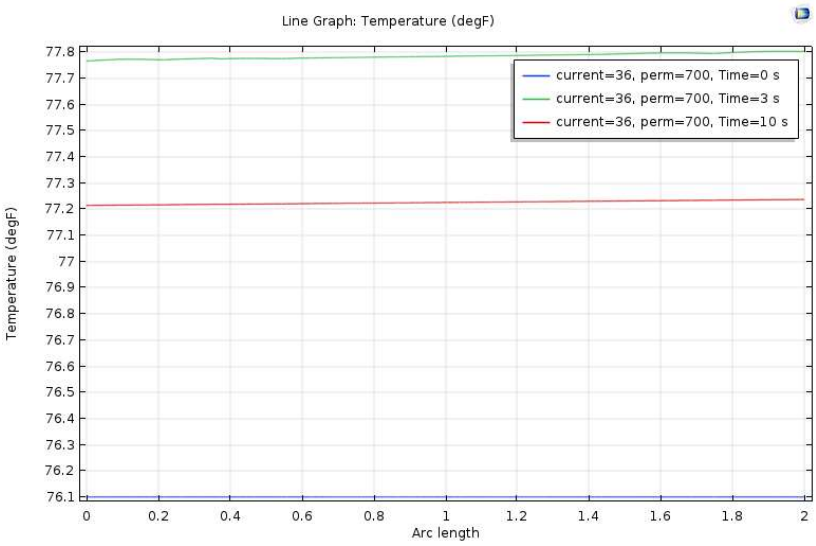

Figure 47 – Temperature Profiles with an Emissivity of 0.5

The difference in final temperatures between ε = 0.1 and ε = 0.5 was negligible, meaning that radiative cooling was minimal. Thus, a value of 0.1 was used for the remainder of the testing.

5.1.5 HAZ Location

Initially, each HAZ region was approximated to be 0.0625” wide and offset from the welded region by 0.125” on each side. However, after performing the trackline comparisons as seen in 4.3.3, the alignment of the temperature spikes was not favorable under these conditions. Based on these initial results, the HAZ locations were adjusted such that they were each 0.125” wide and adjacent to the welded region. Refer to Figure 48 for the original placement of the HAZ and Figure 49 for the final placement.

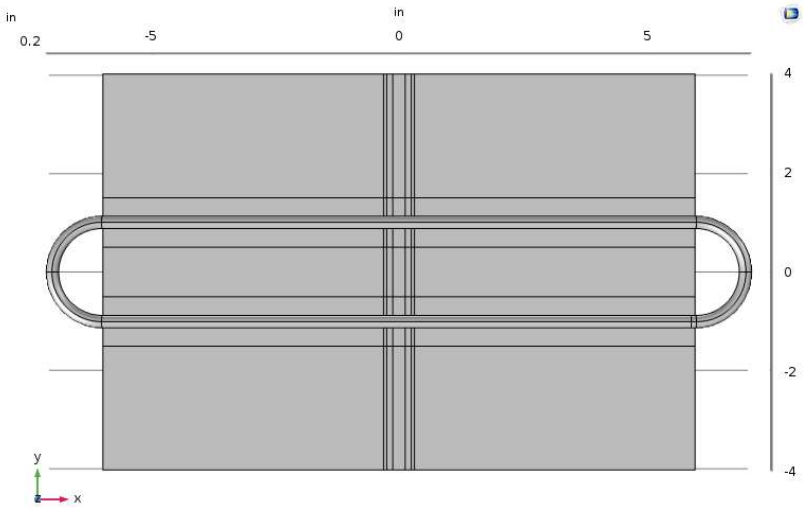

Figure 48 – Original Placement of HAZ

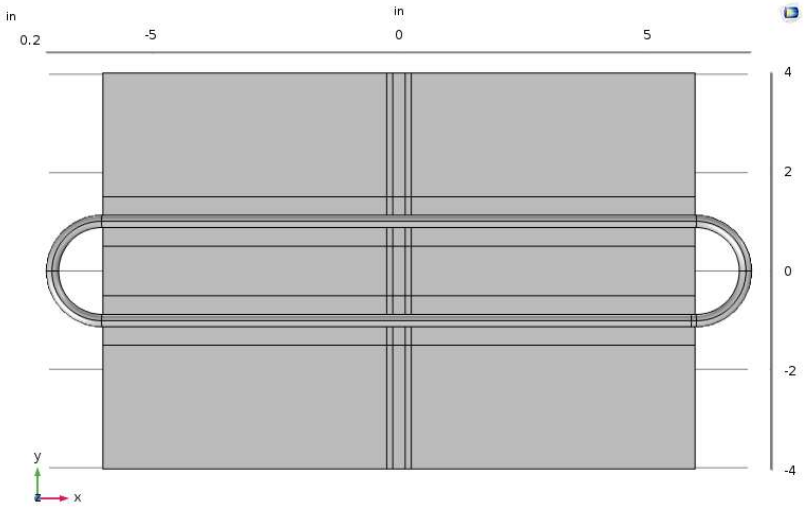

Figure 49 – Modified Placement of HAZ

5.2 Meshing

The mesh used in the COMSOL model was tailored to maximize computational efficiency while still capturing the important electromagnetic and heating behaviors. In addition to the impedance boundary condition simplification previously described:

1. A boundary mesh was used on the surface of the coil as, when using the impedance boundary condition, the interior could be safely neglected, thus saving elements.
2. A boundary mesh was also used on the top surface of the plate, but it was swept through the plate's depth using three (3) elements along its 0.125" height.
3. New domains were added underneath the coil to more accurately capture the heating along its length, each with a 1" width.
    a. Along the 1" width in the HAZ/weld region, a distribution of 50 total elements was used to capture the heating spikes.
    b. Along the longitudinal direction of these new domains (outside of the weld and HAZ regions) 100 total elements were used.
4. Coarser elements were used through the rest of the domains, including the surrounding air and within the plate away from the coil.

Figure 48 shows the meshing of the plate and coil with the air domain removed for clarity. Approximately 275,000 elements were used in total.

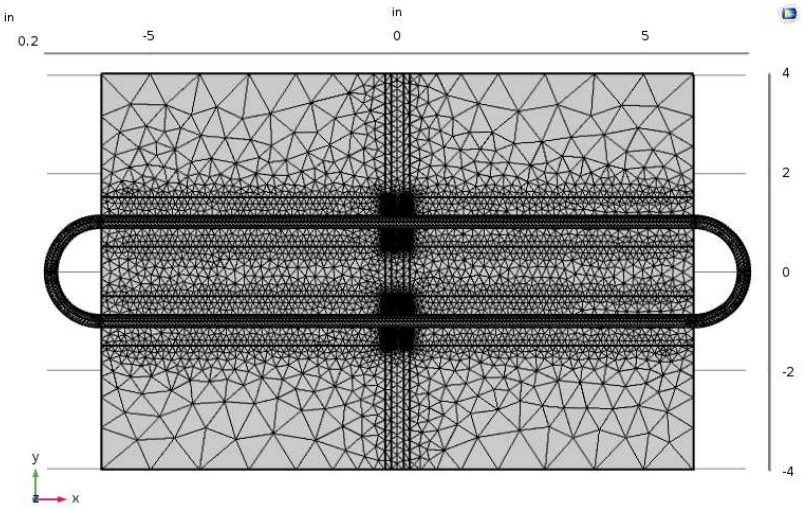

Figure 50 – COMSOL Model Mesh

5.3 Behavior of Welded Region

As alluded to earlier, the welded region was ignored in the model due to its lack of impact on the analysis of sensitization but there are behaviors worth discussing. Despite using the same sample, depending on the heating and settling times and the coil used, the weld presented itself as either a dip or a spike in the intensity counts. That is, it either heated faster or slower than the surrounding material.

For context, refer to Figure 51 which shows the temperature profiles of welded Trial 1 from 2019. Each line represents the heating (over time) of one point selected within Virtuoso (see Figure 52 for the location of these points). Most of the points are selected within the HAZ regions but there are four distinct points (curves) that heat slower than the rest which are the ones located within the weld.

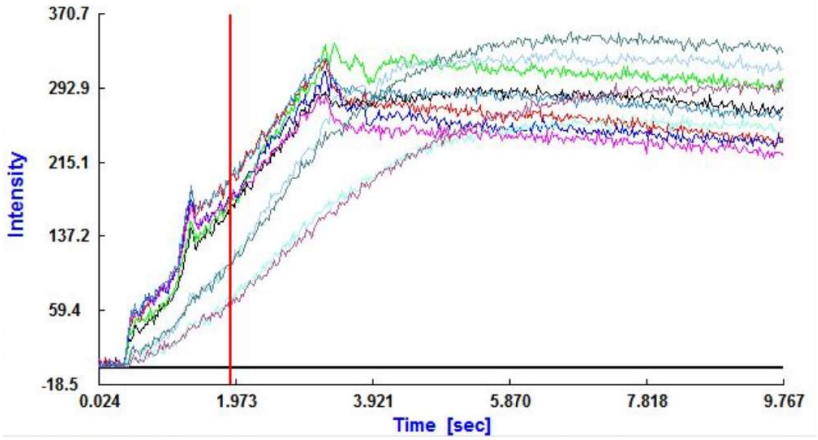

Figure 51 – Welded Trial 1 Virtuoso Temperature Profiles

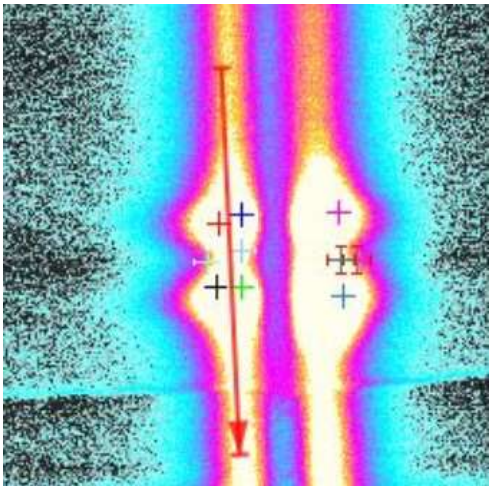

Figure 52 – Welded Trial 1 Virtuoso Data Points

The material used in the welded region is 309 steel which possesses a relative magnetic permeability of 1.008 [5, 8]. Even though it has a comparable electrical resistivity to the 440C parent plate material (780e-9 Ω-m vs. 680e-9 Ω-m for 440C [5]), the magnetic permeability difference between this and the 440C changes the skin depth enough that, at early time steps, the heat penetrates far deeper in the weld than the surrounding metal, showing up as a dip when compared to the surrounding HAZ.

Over a longer time period, however, the heat will continue to build after which this region will appear as a spike in the intensity plot. In Figure 51, even though the coil is removed after

approximately 3 seconds, the points in the weld see an almost monotonic increase in intensity counts (temperature) up through the end of the capture period. This behavior was described by Oswald-Tranta et al. [22] where surface cracks in magnetic materials show more rapid heating and will show up as regions with higher temperatures whereas cracks in non-magnetic materials will show up with as regions with lower temperatures.

Differences in values of physical parameters relevant to IIRT between the weld and parent plate materials are necessary to understand. They should be considered when analyzing such data to ensure that false conclusions on the presence of sensitization are not made.

5.4 Emissivity

Up to this point, little has been discussed regarding emissivity, but it is worth a treatment here. Emissivity describes the inherent property of a material to emit thermal radiation. For a perfect "blackbody," the emissivity is 1, meaning that it is a "perfect" emitter of radiation. An emissivity of 0 means the opposite, that the object does not emit any radiation. As can be imagined, any "real" material will fall somewhere between 0 and 1. However, even within a single sample, emissivity can vary depending on the viewing angle, defects, surface roughness, etc.

This thesis has focused on relative comparisons of intensity counts between individual points rather than looking at global heating behavior. The benefit of this is that, even if there were global differences in emissivity, these could be cancelled out by measuring relative differences in intensity counts rather than trying to use an absolute measure. See the following set of equations for an illustration of the elimination of emissivity by using a relative approach:

$$Baseline: E_1 = \varepsilon\sigma T_1^4$$

$$Heated: E_2 = \varepsilon\sigma T_2^4$$

$$Difference = \frac{|Heated\ Intensity\ Counts - Baseline\ Intensity\ Counts|}{Baseline\ Intensity\ Counts}$$

$$Difference = \frac{|\varepsilon\sigma T_2^4 - \varepsilon\sigma T_1^4|}{\varepsilon\sigma T_1^4}$$

$$Difference = \frac{\varepsilon\sigma|T_2^4 - T_1^4|}{\varepsilon\sigma T_1^4}$$

$$Difference = \frac{|T_2^4 - T_1^4|}{T_1^4}$$

As can be seen, by comparing a single point before and after heating, the emissivity can be cancelled, assuming the emissivity of this point does not change during testing.

5.5 Limitations/Challenges

While much effort went in to eliminating as much variability as possible within the experiments, it was inevitable that some would still exist.

5.5.1 Current in Coil

Although described by the manufacturer, the true current passing through the coil was an unknown and had to be estimated by solving the inverse problem of relating experimental results to the simulations. In addition, with the current varying depending on the material used rather always using a fixed value, even a value found for one set of samples could differ from that in another. Thus, while the results showed good agreement with the experiments, this process is not sustainable and for a predictive model, a known current value would need to be known *a priori*.

5.5.2 IR Thermometer

IR thermometers pose several unique limitations that can introduce error. For one, they are typically calibrated to work in an emissivity range that is close to 1. Working with metal, even metal that has been dulled, can result in emissivity values that are far from 1 and skew the results. Second, depending upon how far the thermometer is from the sample changes the sampling area. The thermometer used had a 12:1 ratio meaning that the diameter of the test area would be 1/12 of the distance of the thermometer from the sample, i.e. holding it 36 cm away from the target would yield a sample area with a 3 cm diameter. With this wide capture area, it is possible that the measured temperatures were impacted by the surrounding regions. Third, there are limitations in the thermometer's resolution. While taking measurements, the temperature would consistently jump in 0.2 °F increments, meaning that there was likely some loss in accuracy of observed temperatures from the thermometer.

5.5.3 Placement of Coil

For repeatability, one location within the sample was chosen to place the coil such that the heating in each trial would be as consistent as possible. As it was not held in place with a jig or a clamp, there was inherent variability in its location in each trial, both in its position above the sample but also in its liftoff distance. With the relatively small changes in absolute temperature between the baseline and the heated conditions, this could have had a sizeable impact.

6 Conclusions and Future Work

The foundation laid by Tucker showed the viability of IIRT as a suitable technique to qualitatively observe sensitization present within the heat affected zones (HAZ) of welded stainless steel plates. By applying first-principle physics, an expansion has been made where the intensity variations seen in IIRT experiments due to sensitization can be quantitatively correlated with a temperature increase. Moving one step further, these temperature changes have been duplicated within a numerical model, providing the foundation for future exploration into a comprehensive and predictive tool for field use. The primary findings are as follows:

1. Further validation of the IIRT method to detect sensitization has been performed with asymmetric heating occurring in these regions.
2. The Stefan-Boltzmann law is an acceptable tool to use when relating intensity counts to a temperature increase in IIRT scans.

3. By comparing discrete points in pre- and post-heating IR images, the variability of emissivity can be minimized.
4. Using baseline trials of material known to be unsensitized, a numerical model has been shown to replicate the experimental results.
5. Leveraging the physics of sensitization, a preliminary look has been taken at modeling regions where sensitized material is present to duplicate the temperature rises seen.
6. For the highest degree of model accuracy, the material parameters as well as the applied coil power need to be known *a priori*, the latter of which was not available here.
7. Larger temperature increases (i.e., longer heating times) could be beneficial to get larger contrasts in heating to help alleviate some of the experimental variables.
8. More analysis is needed with new SEM images to draw a correlation between a temperature rise and a DOS which would be important for a predictive tool.

As a result of the work done here, a weld could be checked as follows:

1. Find an area far from the weld of interest that has not been exposed to the temperatures required for sensitization.
2. Record the ambient temperature of the material in the unsensitized region.
3. Use a portable inductor to heat the material in the unsensitized region with a known current and record the IIRT scan to establish a baseline profile.
4. Take an IIRT scan around the weld of interest, being sure to capture the heat affected zone(s).
5. Using the known material parameters of the areas in question, load the numerical model to establish both the baseline and welded profiles.
6. Compare any experimental heating anomalies between the two regions with the model to draw conclusions about sensitization.

Although still in the early stages, the implications of this work are far-reaching. With the range of industries using stainless steels susceptible to sensitization and the limited resources available for NDT/NDE, this forms the basis for future work to be able to detect sensitization in an arbitrary sample with arbitrary parameters.

6.1 Future Work – Modeling

As the concept of IIRT is well understood, the next logical step would be to add more realism to the model to more accurately capture the heat fluctuations. While the physics presented here are accurate, there are limitations as it was based off the inverse problem of trying to match the simulations with experimental results. Ideally, the input parameters would be well-understood ahead of time and could yield results closely matching the experiments with limited human intervention. Several paths can be followed for future work to expand upon what has already been explored.

6.1.1 HAZ Conductivity

One of the primary areas for future exploration is the definition of the HAZ conductivity. Here, the conductivity was looked at in a qualitative sense while respecting the quantitative physics involved. A more thorough treatment of the true grain structure and the physics involved with the

diversion of the eddy currents (such as with the Drude and related models) would increase the accuracy for numerical prediction of the observed temperature spikes.

6.1.2 Weld Incorporation

Although the welded region was not incorporated here, it would be valuable to capture the full heating behavior/profile. There is also the possibility of the welded region contributing to the heating around it (such as in the HAZ), which could render it to be a valuable addition to the model.

6.1.3 Mesh Refinement

An assumption was made early on that the impedance boundary condition could be applied to both the coil and the plate. While justified in the scenarios studied here, this may not always be the case and a more explicit mesh may be needed to capture the skin depth of the material(s). A variable number of meshed layers through the thickness of the sample could also be used, not only to better capture the skin depth but also the resultant heat transfer behavior. Additionally, more refinement could be performed around the HAZ and welded regions to ensure an accurate representation of the heating variations.

6.2 Future Work – Experiments

With a more refined model, new experiments could be run to provide further benchmarks to the model and move it in to a regime where it could predict sensitization with minimal input from the user.

6.2.1 SEM Images

Due to technical limitations at NUWCDIVNPT, new SEM images could not be obtained in time for this work. In the future, accurate SEM images could be applied to provide a firmer basis for the use of the rule of mixtures and conductivity adjustments in the HAZ while providing further justification of the validity of the IIRT method. One of the areas of interest in sensitization is the DOS which describes the amount of sensitization present in a given sample. New SEM images would also enable a more precise treatment to be performed of the relationship between a material's DOS and the resulting temperature changes.

6.2.2 Power Supply

It has been seen that the coil current is one of the primary unknowns in this round of testing, introducing a level of uncertainty. An adjustable power supply that could feed the coil with a known power/current would be beneficial to provide more consistent experimental results.

6.2.3 Means of Sensitization

As discussed in the Introduction, welding is not the sole means of introducing sensitization in to a material. Another material that was investigated by Tucker et al. was that of 301 stainless steel [5]. These samples were unique as they had been sensitized from the factory (as shown by micrograph analysis) rather than being sensitized in a laboratory environment. Analysis of similar samples (those that have homogeneous sensitization, such as after being baked in an oven) could provide more insight in to how the presence of carbides affects the bulk material properties.

6.2.4 Temperatures of Heating

As alluded to above, if a sample could be heated to a higher temperature such that the initial and final temperatures showed a larger difference, it is possible that a higher degree of accuracy and confidence in the results could be obtained as it could help alleviate the error introduced by the IR thermometer. More analysis would have to be done to ensure that this additional heating would not adversely affect the material.

6.2.5 Painting Samples

In infrared thermography, one of the easiest ways to eliminate variability, particularly from emissivity, is to paint the material to emulate something closer to a perfect blackbody. Naturally, this would not be feasible for in-service material, but it may show merits in the calibration stages of a more accurate model.

6.2.6 Surface Treatments

For the sake of eliminating variables, samples were looked at that did not have any surface treatments applied such as grit-blasting or painting. Such surface treatments alter the surface properties due to changes in roughness, etc. which add a level of complexity that is difficult to model. However, in the real-world, these are likely to be seen in many applications and establishing the heating behavior in these scenarios would be useful in building a model with a wider scope.

6.2.7 New Materials

Of ongoing interest is the sensitization of aluminums as they are prone to sensitization at far lower temperatures than those needed for steel [66] and used in a range of industries such as the marine space [17]. NUWCDIVNPT has performed preliminary work in this area but the sensitization of aluminum has further complications to that in steel. By performing experiments on aluminum and giving more consideration to the physical phenomena involved, the model could be positioned to be expanded in the future.

Appendix A – ImageJ Image Processing Procedure

1. Open the image of interest.

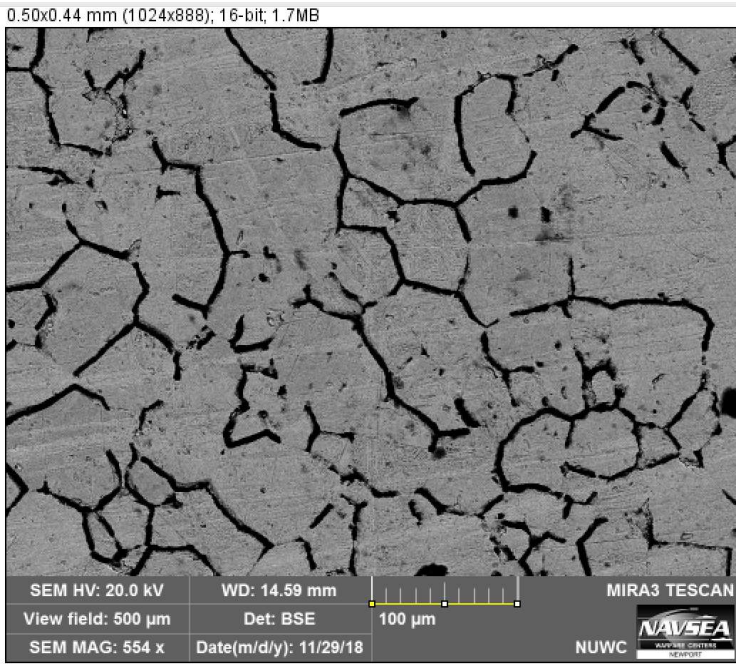

2. Set the scale by marking the ruler then clicking Analyze-Set Scale.

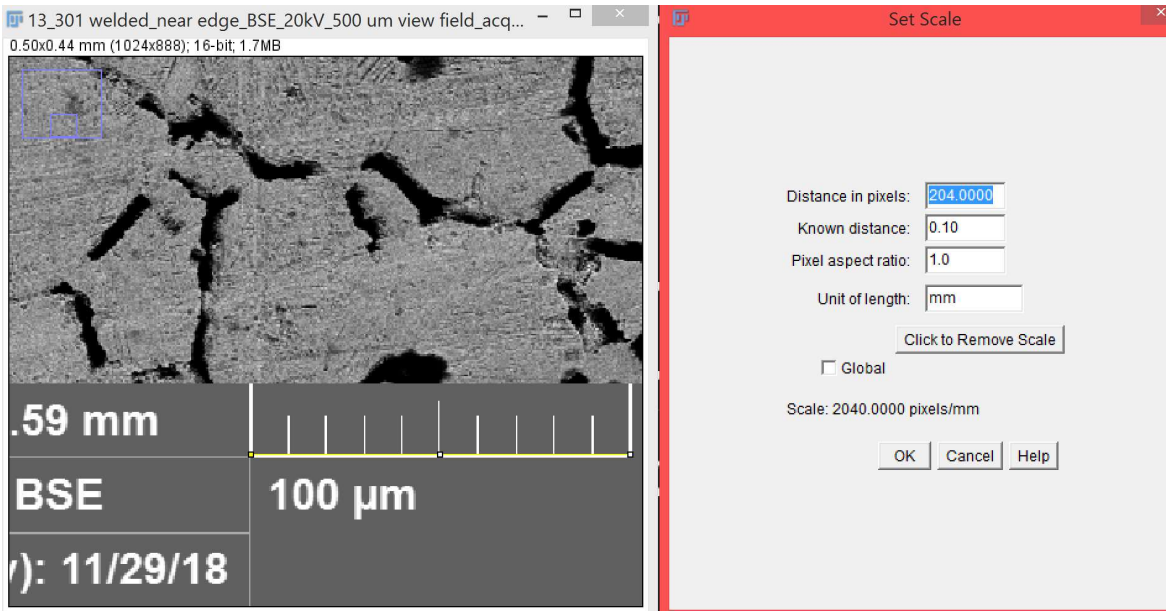

3. Remove the image label by selecting the actual image without the label then clicking Image-Crop
4. Save the file.
5. Check and save the histogram of the grayscale image by going to Analyze-Histogram.

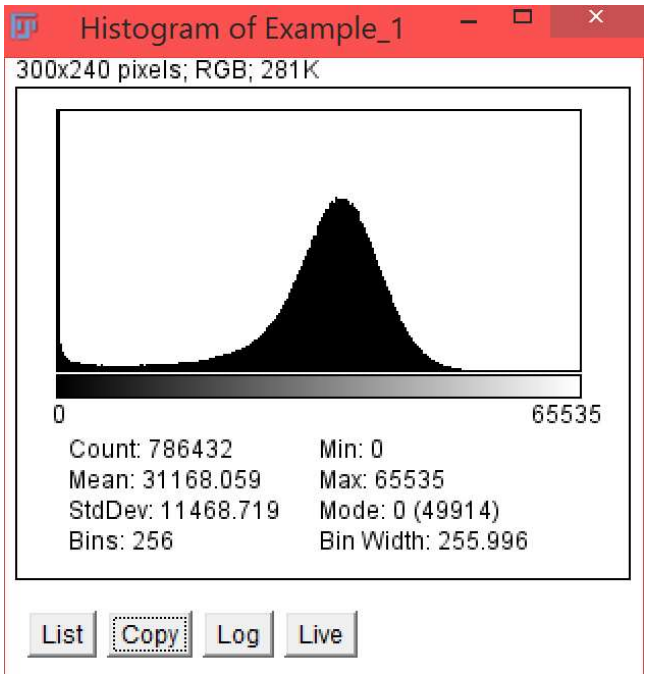

The above histogram indicates a high image quality as the grain boundary (grayscale close to 0) is almost separated from the matrix (the hump in the graph).

6. [Optional] Adjust brightness and contrast if needed using Image-Adjust-brightness/contrast. Then, return to Step 5. Before continuing, the following two goals should be achieved:
    a. The grain boundary (or "feature" of interest) is clear and sharp by "eyeball norm".
    b. The histogram shows that the grain boundary (or "feature") has been separated from the matrix.

    In addition to the brightness and contrast changes, one may also use the Process-Smooth/Sharpen/Noise/etc., but with caution; these operations lead to information loss.

7. Save the file. At this point, the image should be suitable for further processing.

8. Set threshold (of grayscale) for grain boundary (or "feature" in general) by going to Image-Adjust-Threshold. This is where the feature is defined.

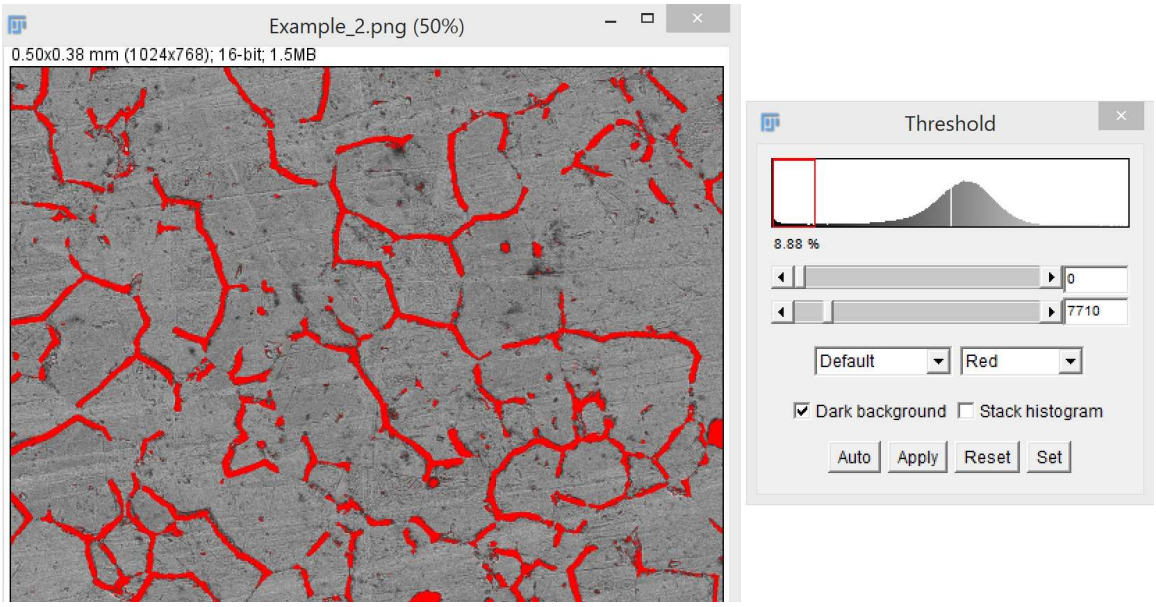

9. Save the file (a black and white image).

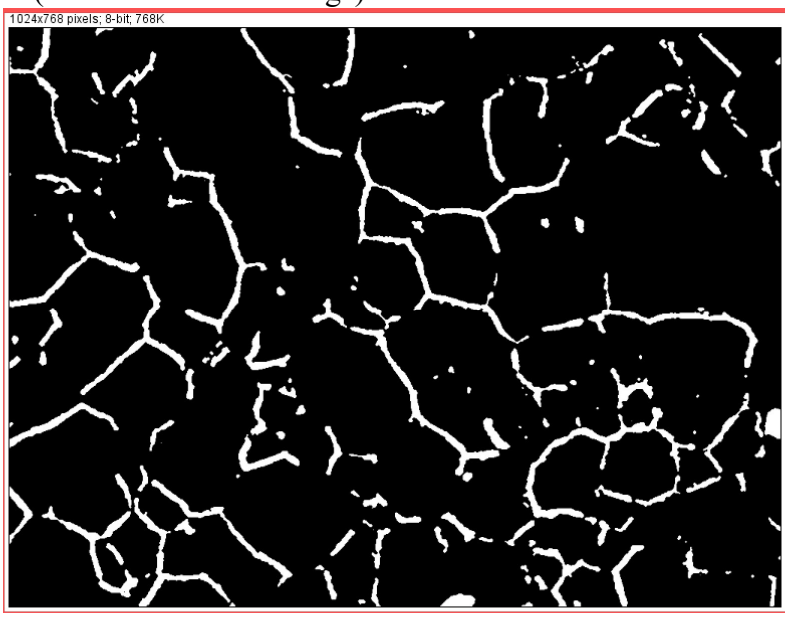

10. Calculate the area of grain boundary through Analyze-Measure. (For the above image, Area = 0.189 mm^2, %Area = 8.436).
11. Skeletonize the grain boundaries in order to analyze the "branches" and calculate their length with Plugins-Skeleton-Skeletonize. The image can be "despeckled" a few times before skeletonization to suppress noise.

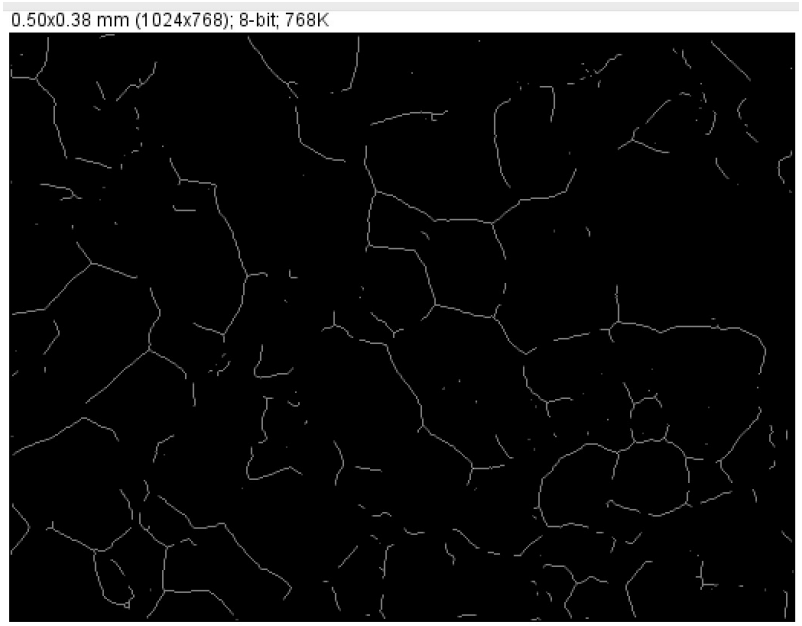

12. Save the file.

13. Analyze the skeleton with Analyze-Skeleton-Analyze Skeleton. Check “Show detailed info”.

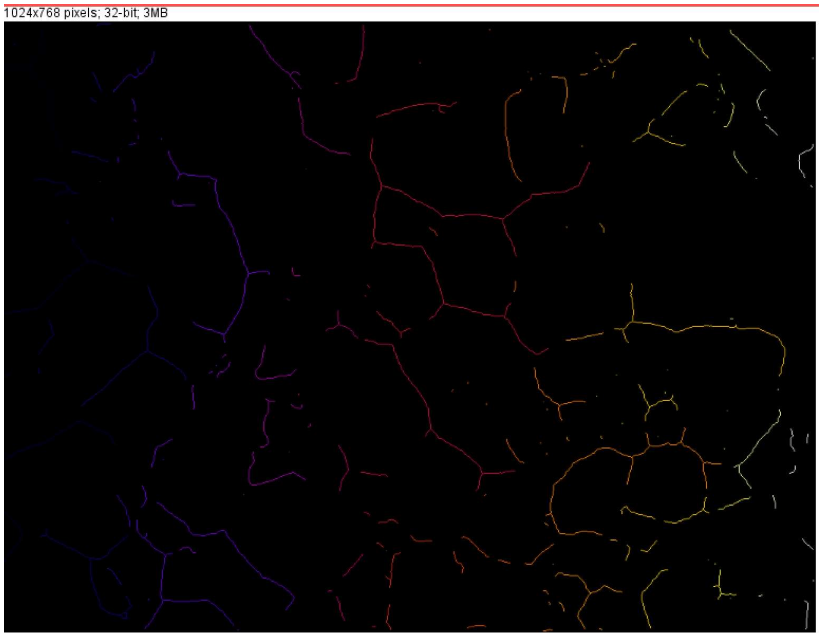

File Edit Font

Skeleton ID	Branch length	V1 x	V1 y	V1 z	V2 x	V2 y	V2 z	Euclidean distance
15	0.048	0.053	0.331	0	0.073	0.366	0	0.040
15	0.034	0.026	0.317	0	0.053	0.331	0	0.031
15	0.009	0.073	0.366	0	0.075	0.364	0	0.004
15	0.004	0.073	0.366	0	0.075	0.364	0	0.004
26	0.004	0.081	0.034	0	0.084	0.031	0	0.003
33	0.029	0.099	0.357	0	0.100	0.329	0	0.027
33	0.018	0.087	0.318	0	0.100	0.329	0	0.017
41	0.091	0.109	0.094	0	0.151	0.155	0	0.075
41	0.045	0.136	0.193	0	0.151	0.155	0	0.041
75	0.046	0.264	0.251	0	0.296	0.278	0	0.042
77	0.085	0.234	0.100	0	0.308	0.122	0	0.077
77	0.071	0.230	0.135	0	0.272	0.173	0	0.057
77	0.041	0.272	0.173	0	0.309	0.181	0	0.038
77	0.037	0.230	0.135	0	0.234	0.100	0	0.035
112	0.081	0.338	0.303	0	0.388	0.269	0	0.061
112	0.021	0.419	0.259	0	0.433	0.272	0	0.019
112	0.021	0.400	0.261	0	0.419	0.259	0	0.019
112	0.015	0.388	0.269	0	0.400	0.261	0	0.014
136	0.069	0.389	0.184	0	0.452	0.188	0	0.063
136	0.009	0.383	0.190	0	0.389	0.184	0	0.008
142	0.015	0.400	0.237	0	0.413	0.233	0	0.014
156	0.005	0.442	0.349	0	0.444	0.352	0	0.004

Save the table of “Detailed info”. The total length of grain boundaries can be calculated by summing the second column. In this case, it is 0.798 mm.

Appendix B – Experimental Data, 2018

Trial 1

Nominal Measured Temperature (Baseline)	76.1 °F
Weld Intensity Counts (Baseline)	5958
Weld Intensity Counts (Heated)	6263
Fractional Difference in Intensity Counts + 1	1.05
(Fractional Difference in Intensity Counts +1)$^{0.25}$	1.01
Predicted Final Temperature	77.1 °F
Nominal Measured Temperature (Heated)	76.9 °F
Wand Frequency	250 kHz

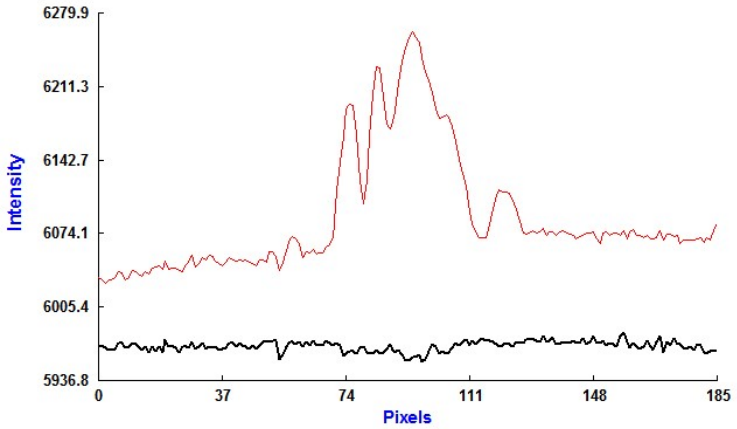

Trial 1 IIRT Scan

Trial 2

Nominal Measured Temperature (Baseline)	77.0 °F
Weld Intensity Counts (Baseline)	6130
Weld Intensity Counts (Heated)	6700
Fractional Difference in Intensity Counts + 1	1.09
(Fractional Difference in Intensity Counts +1)$^{0.25}$	1.02
Predicted Final Temperature	78.7 °F
Nominal Measured Temperature (Heated)	78.6 °F
Wand Frequency	245 kHz

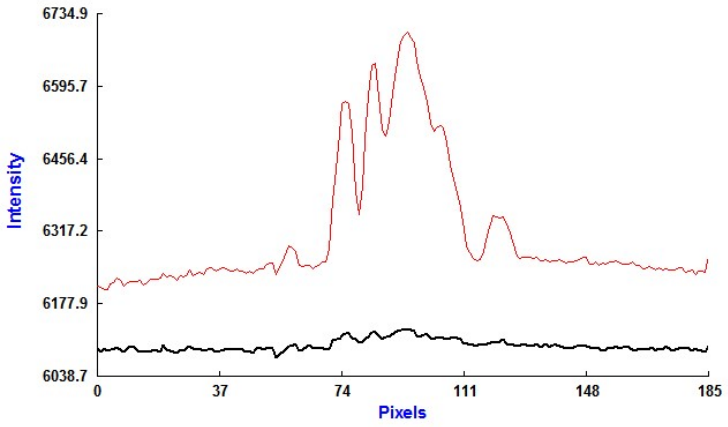

Trial 2 IIRT Scan

Trial 3

Nominal Measured Temperature (Baseline)	77.1 °F
Weld Intensity Counts (Baseline)	6205
Weld Intensity Counts (Heated)	6510
Fractional Difference in Intensity Counts + 1	1.05
(Fractional Difference in Intensity Counts +1)$^{0.25}$	1.01
Predicted Final Temperature	78.0 °F
Nominal Measured Temperature (Heated)	78.2 °F
Wand Frequency	250 kHz

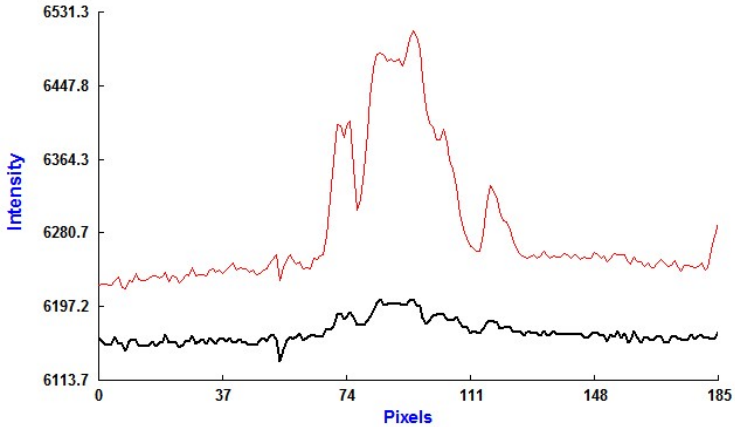

Trial 3 IIRT Scan

Trial 4

Nominal Measured Temperature (Baseline)	77.6 °F
Weld Intensity Counts (Baseline)	6222
Weld Intensity Counts (Heated)	6568
Fractional Difference in Intensity Counts + 1	1.06
(Fractional Difference in Intensity Counts +1)$^{0.25}$	1.01
Predicted Final Temperature	78.7 °F
Nominal Measured Temperature (Heated)	78.6 °F
Wand Frequency	245 – 250 kHz

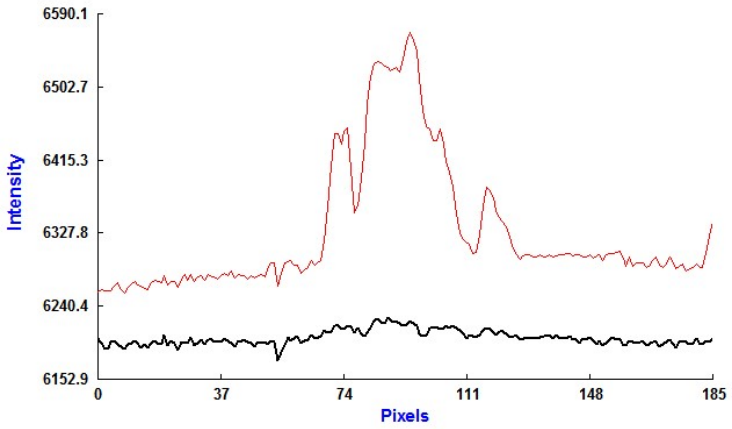

Trial 4 IIRT Scan

Trial 5

Nominal Measured Temperature (Baseline)	78.4 °F
Weld Intensity Counts (Baseline)	6399
Weld Intensity Counts (Heated)	6715
Fractional Difference in Intensity Counts + 1	1.05
(Fractional Difference in Intensity Counts +1)$^{0.25}$	1.01
Predicted Final Temperature	79.3 °F
Nominal Measured Temperature (Heated)	79.1 °F
Wand Frequency	250 – 255 kHz

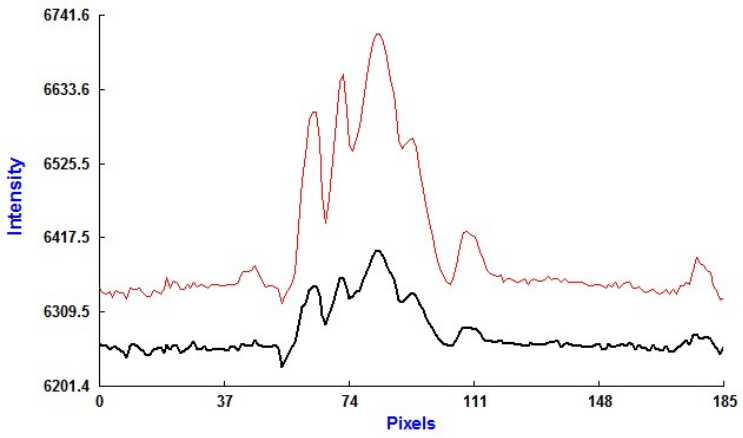

Trial 5 IIRT Scan

Trial 6

Nominal Measured Temperature (Baseline)	77.9 °F
Weld Intensity Counts (Baseline)	6230
Weld Intensity Counts (Heated)	6642
Fractional Difference in Intensity Counts + 1	1.07
(Fractional Difference in Intensity Counts +1)$^{0.25}$	1.02
Predicted Final Temperature	79.2 °F
Nominal Measured Temperature (Heated)	78.9 °F
Wand Frequency	240 – 245 kHz

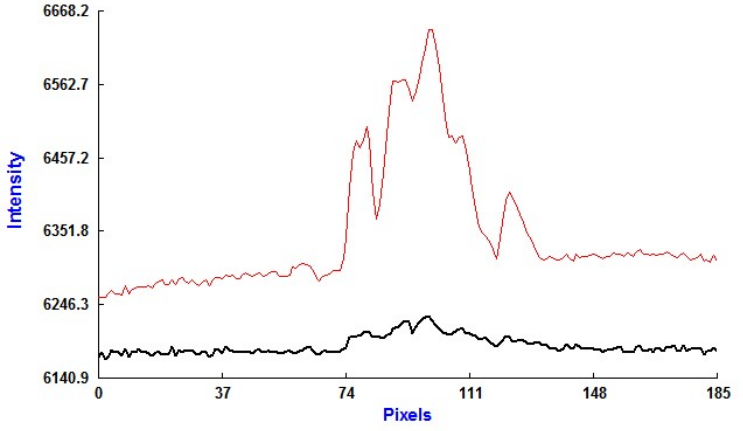

Trial 6 IIRT Scan

Trial 7

Nominal Measured Temperature (Baseline)	78.6 °F
Weld Intensity Counts (Baseline)	6348
Weld Intensity Counts (Heated)	6673
Fractional Difference in Intensity Counts + 1	1.05
(Fractional Difference in Intensity Counts +1)$^{0.25}$	1.01
Predicted Final Temperature	79.6 °F
Nominal Measured Temperature (Heated)	79.1 °F
Wand Frequency	240 – 245 kHz

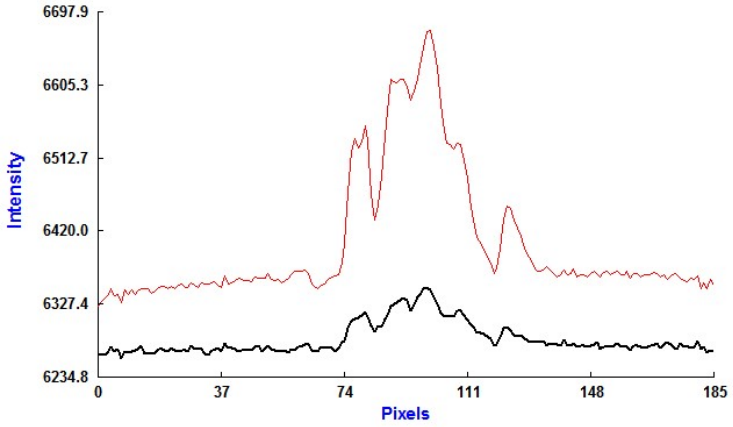

Trial 7 IIRT Scan

Trial 8

Nominal Measured Temperature (Baseline)	79.1 °F
Weld Intensity Counts (Baseline)	6432
Weld Intensity Counts (Heated)	6886
Fractional Difference in Intensity Counts + 1	1.07
(Fractional Difference in Intensity Counts +1)$^{0.25}$	1.02
Predicted Final Temperature	80.5 °F
Nominal Measured Temperature (Heated)	80.2 °F
Wand Frequency	245 – 250 kHz

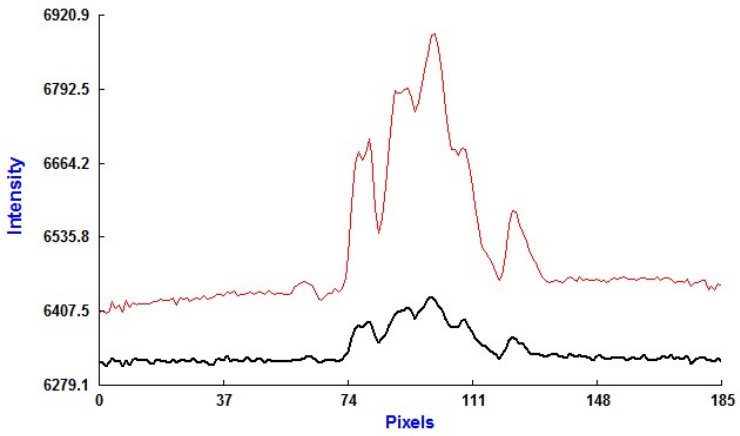

Trial 8 IIRT Scan

Trial 9

Nominal Measured Temperature (Baseline)	79.8 °F
Weld Intensity Counts (Baseline)	6495
Weld Intensity Counts (Heated)	6746
Fractional Difference in Intensity Counts + 1	1.04
(Fractional Difference in Intensity Counts +1)$^{0.25}$	1.01
Predicted Final Temperature	80.6 °F
Nominal Measured Temperature (Heated)	80.6 °F
Wand Frequency	250 kHz

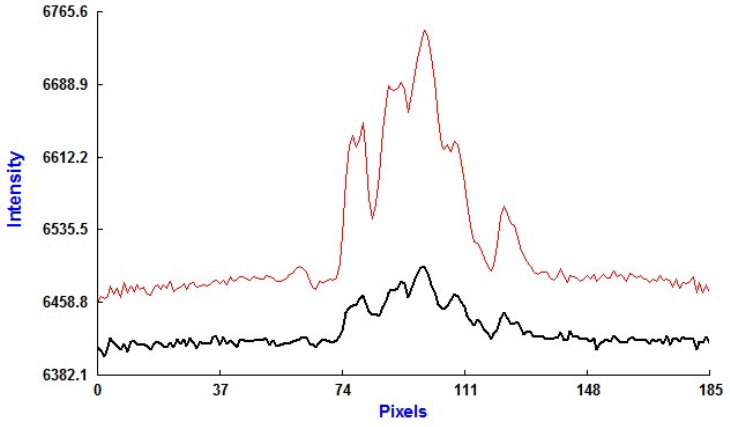

Trial 9 IIRT Scan

Trial 10

Nominal Measured Temperature (Baseline)	80.2 °F
Weld Intensity Counts (Baseline)	6471
Weld Intensity Counts (Heated)	6923
Fractional Difference in Intensity Counts + 1	1.07
(Fractional Difference in Intensity Counts +1)$^{0.25}$	1.02
Predicted Final Temperature	81.6 °F
Nominal Measured Temperature (Heated)	80.9 °F
Wand Frequency	240 – 250 kHz

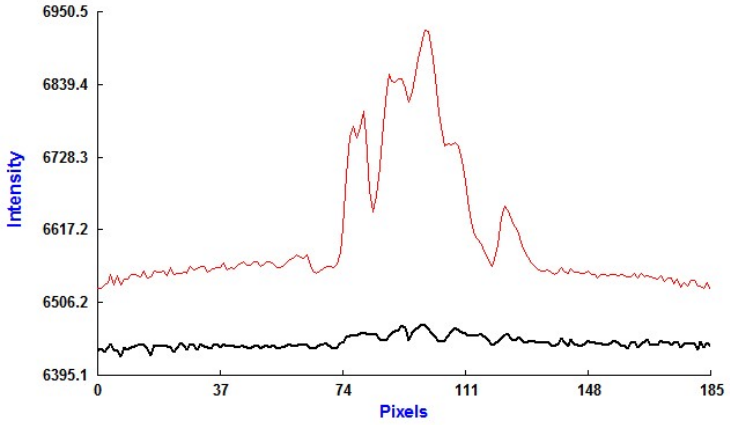

Trial 10 IIRT Scan

Appendix C – Experimental Data, 2019

Baseline Trial 1

Nominal Measured Temperature (Baseline)	76.1 °F
Baseline Intensity Counts	5950
Nominal Measured Temperature (Maximum)	77.9 °F
Maximum Intensity Counts	N/A
Nominal Measured Temperature (End of Trial)	77.7 °F
Final Intensity Counts	N/A

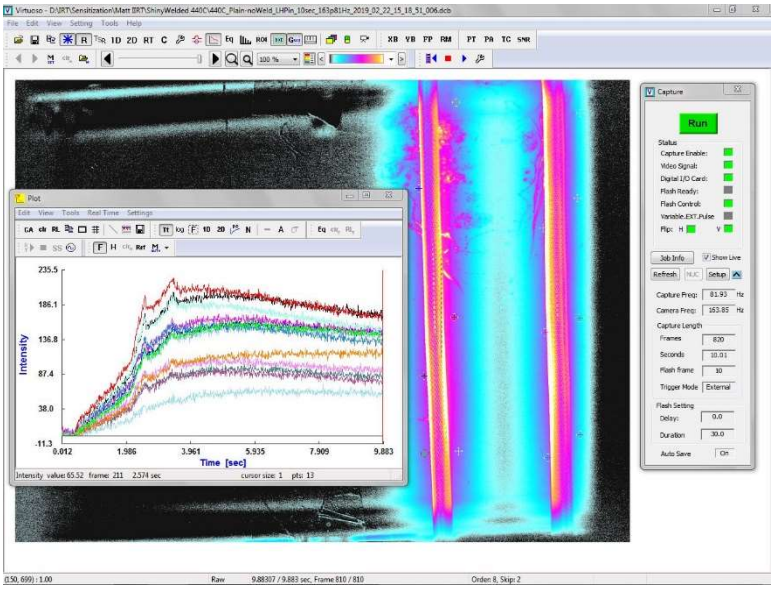

Baseline Trial 1 IIRT Scan

*This data was not available

Baseline Trial 2

Nominal Measured Temperature (Baseline)	76.2 °F
Baseline Intensity Counts	5950
Nominal Measured Temperature (Maximum)	77.9 °F
Maximum Intensity Counts	5950 + 152*
Nominal Measured Temperature (End of Trial)	77.7 °F
Final Intensity Counts	5950 + 126*

*Averaged over 13 measurement points

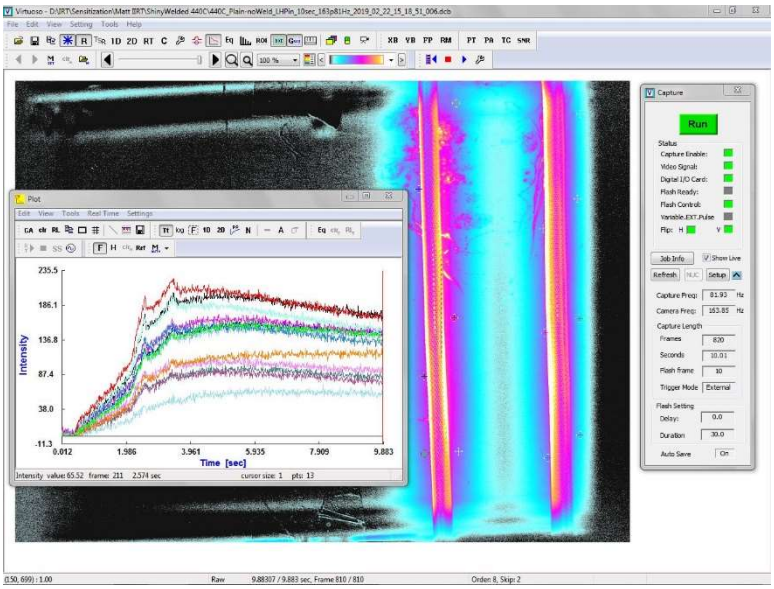

Baseline Trial 2 IIRT Scan

Welded Trial 1

Nominal Measured Temperature (Baseline)	75.2 °F
Baseline Intensity Counts	5760
Nominal Measured Temperature (End of Trial)	76.2 °F
Final Intensity Counts	5760 + 254*
Maximum Intensity Counts	5760 + 313*
Fractional Difference in Intensity Counts + 1	1.01*
(Fractional Difference in Intensity Counts +1)$^{0.25}$	1.002*
Predicted Maximum Temperature	76.4 °F*

*Averaged over 6 measurement points (excluded 4 points within the weld)

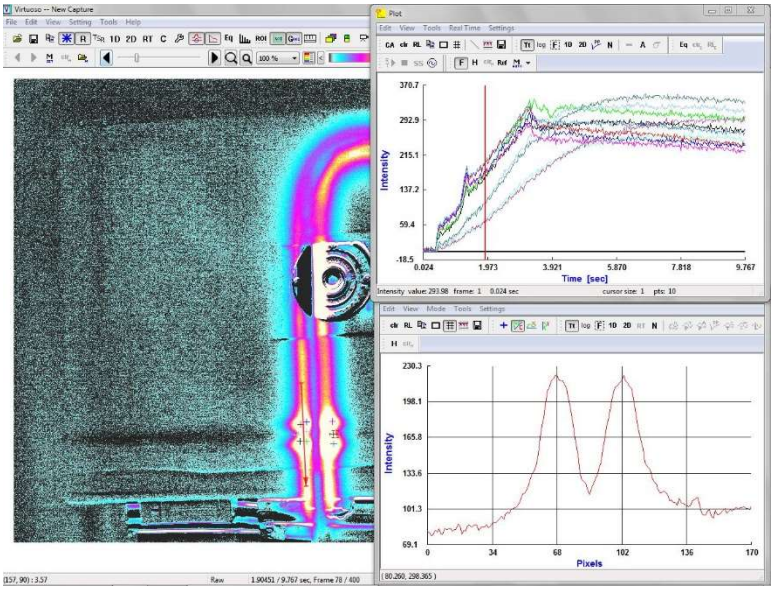

Welded Trial 1 IIRT Scan

Welded Trial 2

Nominal Measured Temperature (Baseline)	75.9 °F
Baseline Intensity Counts	5860
Nominal Measured Temperature (End of Trial)	76.8 °F
Final Intensity Counts	5860 + 290*
Maximum Intensity Counts	5860 + 411*
Fractional Difference in Intensity Counts + 1	1.02*
(Fractional Difference in Intensity Counts +1)$^{0.25}$	1.005*
Predicted Maximum Temperature	77.2 °F*

*Averaged over 6 measurement points (excluded 2 points within the weld)

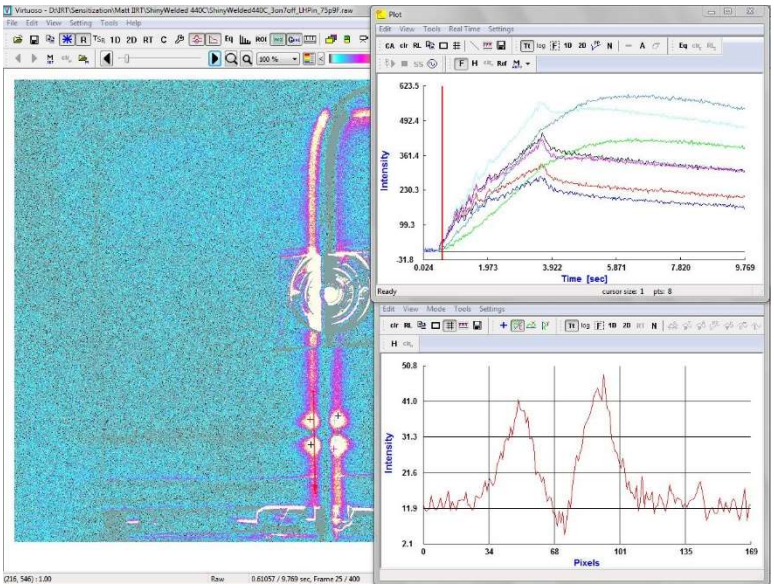

Welded Trial 2 IIRT Scan

Welded Trial 3

Nominal Measured Temperature (Baseline)	75.3 °F
Baseline Intensity Counts	5670
Nominal Measured Temperature (End of Trial)	75.8 °F
Final Intensity Counts	5670 + 176*
Maximum Intensity Counts	5670 + 324*
Fractional Difference in Intensity Counts + 1	1.03*
(Fractional Difference in Intensity Counts +1)$^{0.25}$	1.006*
Predicted Maximum Temperature	76.3 °F*

*Averaged over 4 measurement points (excluded 2 points within the weld)

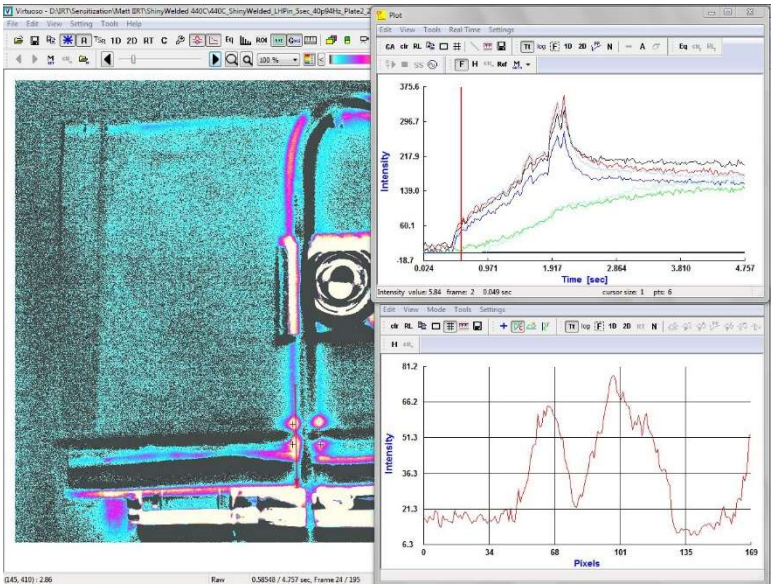

Welded Trial 3 IIRT Scan

Welded Trial 4

Nominal Measured Temperature (Baseline)	75.7 °F
Baseline Intensity Counts	5830
Nominal Measured Temperature (End of Trial)	76.2 °F
Final Intensity Counts	5830 + 182*
Maximum Intensity Counts	5830 + 262*
Fractional Difference in Intensity Counts + 1	1.01*
(Fractional Difference in Intensity Counts +1)$^{0.25}$	1.003*
Predicted Maximum Temperature	76.5 °F*

*Averaged over 4 measurement points (excluded 2 points within the weld)

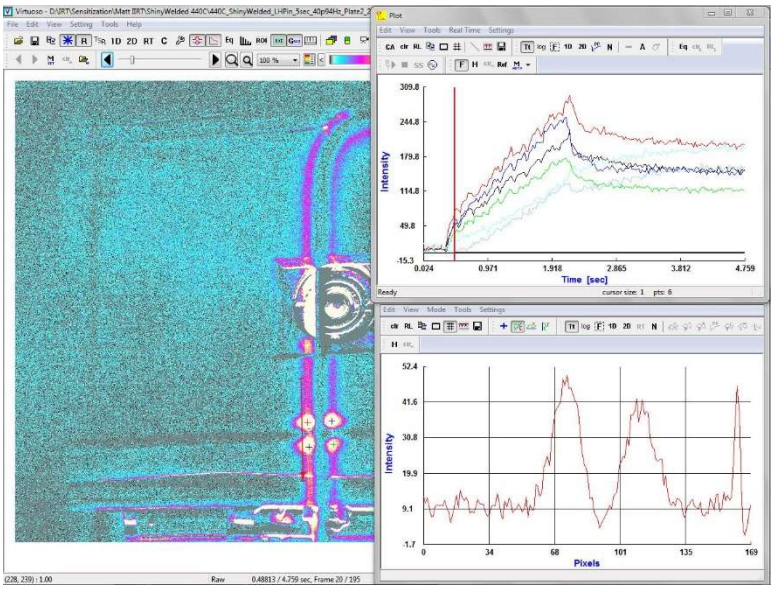

Welded Trial 4 IIRT Scan

Welded Trial 5

Nominal Measured Temperature (Baseline)	76.2 °F
Baseline Intensity Counts	5950
Nominal Measured Temperature (End of Trial)	76.7 °F
Final Intensity Counts	5950 + 155*
Maximum Intensity Counts	5950 + 233*
Fractional Difference in Intensity Counts + 1	1.01*
(Fractional Difference in Intensity Counts +1)$^{0.25}$	1.003*
Predicted Maximum Temperature	76.9 °F*

*Averaged over 8 measurement points (excluded 2 points within the weld)

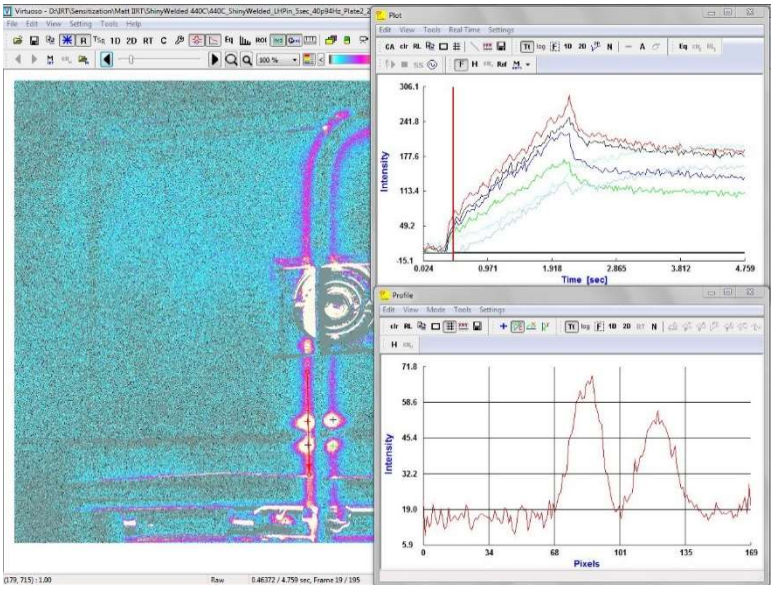

Welded Trial 5 IIRT Scan

References

[1] C.S. Tedmon Jr., D.A. Vermilyea, and J.H. Rosolowski, "Intergranular corrosion of austenitic stainless steel," *Journal of the Electrochemical Society*, vol. 118, no. 2, pp. 192-202, Feb. 1971.

[2] G.S. Was, R.M. Kruger, "A thermodynamic and kinetic basis for understanding chromium depletion in Ni-Cr-Fe alloys," *Acta metallurgica*, vol. 33, no. 5, pp. 841-854, May 1985.

[3] D.A. Jones, *Principles and Prevention of Corrosion*. Upper Saddle River, NJ, USA: Prentice-Hall, Inc., 1996.

[4] *CORROSION: Intergranular Corrosion* (n.d.) [Online]. Available: http://www.ssina.com/corrosion/igc.html.

[5] W.C. Tucker, P. Lockhart, E. Guzas, "Evaluating sensitized chromium steel alloys with induction infrared thermography," *Journal of Nondestructive Evaluation*, vol. 38, no. 2, article 42, Jun. 2019.

[6] ASTM A262-15 Standard Practices for Detecting Susceptibility to Intergranular Attack in Austenitic Stainless Steels, ASTM International, West Conshohocken, PA, 2015, https://doi.org/10.1520/A0262-15

[7] S.N. L'vov, V.F. Nemchenko, P.S. Kislyi, T.S. Verkhoglyadova, T. Ya. Kosolapova, "The electrical properties of chromium borides, carbides, and nitrides," *Soviet Powder Metallurgy and Metal Ceramics*, vol. 1, no. 4, pp. 243-247, Jul. 1962.

[8] *MatWeb Material Property Database* (n.d.) [Online]. Available: http://www.matweb.com/.

[9] M. Roberts, K. Wang, E. Guzas, P. Lockhart, W. Tucker, "Induction infrared for thermography for non-destructive evaluation of alloy sensitization," presented at the 45th Annual Review of Progress in Quantitative Nondestructive Evaluation, Burlington, VT, USA, 2018.

[10] I.Z. Abidin, M.Z Umar, M.Y. Yusof, M.M. Ibrahim, A.R. Hamzah, M.N. Salleh, "Advantages and applications of eddy current thermography testing for comprehensive and reliable defect assessment," presented at the 18th World Conference on Nondestructive Testing, Durban, South Africa, 2012.

[11] N.S. Rusli, I.Z. Abidin, S.A. Aziz, "A review on eddy current thermography technique for non-destructive testing application," *Jurnal Teknologi*, vol. 78, no.11, pp. 127-132, Nov. 2016.

[12] G. Walle, U. Netzelmann, C. Stumm, B. Valeske, "Low frequency induction thermography for the characterization of hidden cracks in ferromagnetic steel components," presented at the 11th International Conference on Quantitative InfraRed Thermography, Naples, Italy, 2012.

[13] J. Vrana, M. Goldammer, J. Baumann, M. Rothenfusser, W. Arnold, "Mechanisms and models of crack detection with induction thermography," in *34th Annual Review of Progress in Quantitative Nondestructive Evaluation*, Golden, CO, USA, 2007, pp. 475-482.

[14] U. Netzelmann, G. Walle, "Induction thermography as a tool for reliable detection of surface defects in forged components," presented at the 17th World Conference on Nondestructive Testing, Shanghai, China, 2008.

[15] J. Peng, G. Tian, L. Wang, X. Gao, Y. Zhang, Z. Wang, "Rolling contact fatigue detection using eddy current pulsed thermography," in *2014 IEEE Far East Forum on Nondestructive Evaluation/Testing*, Chengdu, China, 2014, pp. 176-180.

[16] B. Oswald-Tranta, G. Wally, "Thermo-inductive investigations of steel wires for surface cracks," in *SPIE 5782, Thermosense XXVII*, Orlando, FL, USA, 2005, pp. 245-254.

[17] W. Świderski, "Possibility of defect detection by eddy current thermography in marine structures," *Scientific Journals of the Maritime University of Szczecin*, vol. 44, no. 116, pp. 43-46, Jul. 2015.

[18] D. Vasić, V. Bilas, D. Ambruš, "Pulsed eddy-current nondestructive testing of ferromagnetic tubes," *IEEE Transactions on Instrumentation and Measurement*, vol. 53, no. 4, pp. 1289-1294, Aug. 2004.

[19] M. He, L. Zhang, W. Zheng, Y. Feng, "Crack detection based on a moving mode of eddy current thermography method," *Measurement*, vol. 109, pp. 119-129, Oct. 2017.

[20] S. Yang, G.Y. Tian, I.Z. Abidin, J. Wilson, "Simulation of edge cracks using pulsed eddy current stimulated thermography," *Journal of Dynamic Systems, Measurement, and Control*, vol. 133, no. 1, pp. 011008-1-011008-6, Nov. 2010.

[21] I.Z. Abidin, G.Y. Tian, J. Wilson, S. Yang, D. Almond, "Quantitative evaluation of angular defects by pulsed eddy current thermography," *NDT&E International*, vol. 43, no. 7, pp. 537-546, Oct. 2010.

[22] B. Oswald-Tranta, G. Wally, "Thermo-inductive surface crack detection in metallic materials," presented at the 9th European Conference on NDT, Berlin, Germany, 2006.

[23] B. Cannas, S. Carcangiu, N. Trulli, "Modeling of active infrared thermography for defect detection in concrete structures," presented at the 8th Annual Conference on Multiphysics Simulation, Milan, Italy, 2012.

[24] G. Li, M. Genest, "Numerical simulation of induction thermography on a laminated composite panel," presented at the American Society for Composites 31st Technical Conference, Williamsburg, VA, USA, 2016.

[25] H. Shaikh, N. Sivaibharasi, B. Sasi, T. Anita, R. Amirthalingam, B.P.C. Rao, T. Jayakumar, H.S. Khatak, Baldev Raj, "Use of eddy current testing method in detection and evaluation of sensitisation and intergranular corrosion in austenitic stainless steels," *Corrosion Science*, vol. 48, no. 6, pp. 1462-1482, Jun. 2006.

[26] H. Kikuchi, H. Yanagiwara, H. Takahashi, T. Sumimoto, T. Murakawi, "Detection of sensitization for 600 alloy and austenitic stainless steel by magnetic field sensor," presented at the 19th World Conference on Non-Destructive Testing, Munich, Germany 2016.

[27] S.T. Abraham, S.K. Albert, C.R. Das, N. Parvathavarthini, B. Venkatraman, R.S. Mini, K. Balasubramaniam, "Assessment of sensitization in AISI 304 stainless steel by nonlinear ultrasonic method," *Acta Metallugica Sinica*, vol. 26, no. 5, pp. 545-552, Oct. 2013.

[28] A. Cobb, E. Macha, J. Bartlett, Y. Xia, "Detecting sensitization in aluminum alloys using acoustic resonance and EMAT ultrasound," in *43rd Annual Review of Progress in Quantitative Nondestructive Evaluation*, Atlanta, GA, USA, 2016, pp. 050001-1-050001-9.

[29] J. Stella, J. Cerezo, E. Rodriguez, "Characterization of the sensitization degree in the AISI 304 stainless steel using spectral analysis and conventional ultrasonic techniques," *NDT&E International*, vol. 42, no. 4, pp. 267-274, Jun. 2009.

[30] J.Y. Park and D. Grove, III, "Portable probe to measure sensitization of stainless steel," U.S. Patent 4,179,349, 18 Dec., 1979.

[31] *ElectraWatch Degree of Sensitization (DoS) Probe* (n.d.) [Online]. Available: http://electrawatch.com/ElectraWatch_DoS_Probe_Datasheet.pdf.

[32] ASTM G108-94(2015) Standard Test Method for Electrochemical Reactivation (EPR) for Detecting Sensitization of AISI Type 304 and 304L Stainless Steels, ASTM International, West Conshohocken, PA, 2015, https://doi.org/10.1520/G0108-94R15

[33] B. Patidar, M.M. Hussain, S. Das, D. Mukherjee, A.P. Tiwari, "Simulation and experimental validation of induction heating of MS tube for elevated temperature NDT application," in *COMSOL Conference 2015 Pune*, Pune, India, 2015.

[34] G.Y. Tian, J. Wilson, L. Cheng, D.P. Almond, E. Kostson, B. Weekes, "Pulsed eddy current thermography and applications," in *Lecture Notes in Electrical Engineering,* vol. 96*, New Developments in Sensing Technologies for Structural Health Monitoring*, Subhas Chandra Mukhopadhyay, Ed. Berlin/Heidelberg, Germany: Springer-Verlag Berlin Heidelberg, 2011, pp. 205-231.

[35] K. Djellabi, M.E.H. Latreche, "Induction heating process design using Comsol Multiphysics software version 4.2a," *World Academy of Science, Engineering, and Technology,* vol. 8, no. 1, pp. 72-75, Jan. 2014.

[36] *Joules law* (n.d.) [Online]. Available: https://www.britannica.com/science/Joules-law.

[37] E. Bogatin, *Signal Integrity – Simplified*. Upper Saddle River, NJ: Prentice Hall Professional Technical Reference, 2004.

[38] *Basics of Induction Heating* (n.d.) [Online]. Available: https://radyne.com/what-is-induction/induction-heating-basics/.

[39] F. Bay, V. Labbe, Y. Favennec, J. L. Chenot, "A numerical model for induction heating processes coupling electromagnetism and thermomechanics," *International Journal for Numerical Methods in Engineering*, vol. 58, no. 6, pp. 839-867, Jul. 2003.

[40] S.C. Chen, H.S. Peng, J.A. Chang, W.R. Jong, "Simulations and verifications of induction heating on a mold plate," *International Communications in Heat and Mass Transfer*, vol. 31, no. 7, pp. 971-980, Oct. 2004.

[41] M. Fisk, "Simulation of induction heating in manufacturing," Licentiate Thesis, Luleå University of Technology, Luleå, Sweden, 2008.

[42] B. Oswald-Tranta, "Induction thermography for surface crack detection and depth determination," *Applied Sciences*, vol. 8, no. 2, article 257, Feb. 2018.

[43] C.V. Dodd, W.E. Deeds, "Analytical solutions to eddy-current probe coil problems," Oak Ridge National Laboratory, Oak Ridge, Tennessee, USA, ORNL-TM-1987, Nov. 1967.

[44] A. Ikram, N. Arif, H. Chung, "Design of an induction system for induction assisted alternating current gas metal arc welding," *Journal of Materials Processing Technology*, vol 231, pp. 162-170, May 2016.

[45] J.D. Jackson, "From Lorentz to Coulomb and other explicit gauge transformations," Lawrence Berkeley National Laboratory, Berkeley, CA, USA, LBNL-50079, 17 Apr. 2002.

[46] Z. Liu, X Liu, L. Jiang, G. Lu, H. Liu, "Study on the heat transfer characteristics performed in the infrared thermography detection of welded structure," *The Open Mechanical Engineering Journal*, vol. 9, pp. 251-259, Apr. 2015.

[47] D. Fofanov, S. Riedner, "Magnetic properties of stainless steels: applications, opportunities and new developments."

[48] J-B. Izard, "Development of remote handling technologies tolerant to operation ready fusion reactor conditions, Thesis, Tampere University of Technology, Hervanta, Finland, 2013.

[49] *MagWeb: World's Largest Database of Magnetic Materials* (n.d.) [Online]. Available: https://magweb.us/free-bh-curves/.

[50] *NESS ENGINEERING TECHNICAL DATA METAL / ALLOY RESISTIVITY* (2014, Oct. 21) [Online]. Available: http://www.nessengr.com/techdata/metalresis.html.

[51] M. Alger, *Polymer Science Dictionary*. Dordrecht, Netherlands: Springer Science+Business Media Dordrecht, 2017.

[52] *Derivation of the rule of mixtures and inverse rule of mixtures* (n.d.) [Online]. Available: https://www.doitpoms.ac.uk/tlplib/bones/derivation_mixture_rules.php.

[53] *Stefan-Boltzmann law* (n.d.) [Online]. Available: https://www.britannica.com/science/Stefan-Boltzmann-law.

[54] *The Engineering ToolBox, Radiation Heat Transfer* (n.d.) [Online]. Available: https://www.engineeringtoolbox.com/radiation-heat-transfer-d_431.html.

[55] *AISI 440C STAINLESS STEEL BALLS* (n.d.) [Online]. Available: http://www.rgpballs.com/en/products/BALLS/QUICK-SELECTION/STEEL/STAINLESS-STEEL/HARDENED-STAINLESS-STEEL/AISI-440C-STAINLESS-STEEL-BALLS.

[56] COMSOL Inc., *COMSOL Multiphysics 5.3a*. [Digital]. Stockholm, Sweden: COMSOL Inc., 2017.

[57] T.B.A. Senior, "Approximate boundary conditions," University of Michigan Radiation Laboratory, Ann Arbor, MI, USA, RL-681, Aug. 1980.

[58] COMSOL Inc. Technical Staff, *AC/DC Module 5.3a User's Guide*, COMSOL Inc., 2017.

[59] W.H. McAdams, *Heat Transmission*. New York, NY: McGraw Hill, 1954.

[60] İ. Dinçer, M.A. Rosen, *Thermal Energy Storage: Systems and Applications*. Chichester, West Sussex, United Kingdom: John Wiley & Sons, 2011.

[61] A.E. Drake. *National Physical Laboratory, Kaye & Laby Tables of Physical & Chemical Constants, 2.6.6 Magnetic Properties of Materials* (n.d.) [Online]. Available: http://www.kayelaby.npl.co.uk/general_physics/2_6/2_6_6.html.

[62] *Metals: the Drude model of electrical conduction* (n.d.) [Online]. Available: https://www.doitpoms.ac.uk/tlplib/thermal_electrical/drude.php.

[63] A.F.J Levi, *Essential Classical Mechanics for Device Physics*. San Rafael, CA, USA: Morgan & Claypool, 2016.

[64] N.W. Ashcroft, N.D. Mermin, *Solid State Physics*. Fort Worth, TX: Harcourt, Inc., 1976.

[65] *Optotherm Support, Emissivity in the Infrared, Emissivity Values* (n.d.) [Online]. Available: https://www.optotherm.com/emiss-table.htm.

[66] R. Zhang, S.P. Knight, R.L Holtz, R. Goswami, C.H.J. Davies, N. Birbilis, "A survey of sensitization in 5xxx series aluminum alloys," *Corrosion*, vol. 72, no. 2, pp. 144-159, Feb. 2016.